

The Multiscale Nature of Tropical Convection in Observations and Models

Pedro Angulo-Umaña

A dissertation
submitted in partial fulfillment of the
requirements for the degree of

Doctor of Philosophy

University of Washington

2025

Reading Committee:

Peter Blossey, Chair

Daehyun Kim

Dargan Frierson

Program Authorized to Offer Degree:
Atmospheric and Climate Science

©Copyright 2025

Pedro Angulo-Umaña

University of Washington

Abstract

The Multiscale Nature of Tropical Convection in Observations and Models

Pedro Angulo-Umaña

Chair of the Supervisory Committee:

Peter Blossey

Department Atmospheric and Climate Sciences

This dissertation seeks to improve understanding of tropical convection's multiscale nature. By utilizing high-resolution observations, global reanalysis, and convection-permitting numerical models, this dissertation examines the multiscale structure of tropical convection. The physical processes that couple different scales of motion to one another are also examined. In this dissertation we will: use satellite observations to show that the multiscale structure of tropical precipitation features impacts the likelihood of the feature generating a local-scale, intense rain rate event; use high-resolution idealized models to explore the possible mechanism behind this coupling, namely the interaction between convective updrafts via turbulent mixing; and use a global, storm-resolving model to separate large-scale and small-scale convective motions, and characterize their co-evolutions and mutual influences on one another.

TABLE OF CONTENTS

	Page
List of Figures	iii
Chapter 1: Introduction and Thesis Outline	1
1.1 Scale Interactions and Extreme Instantaneous Rainfall	3
1.2 Scale Interactions and Large-Scale Vertical Circulations	5
Chapter 2: The Role of Morphology in Extreme-Producing Tropical Precipitation Systems	8
2.1 Introduction	8
2.2 Data and Methods	11
2.3 Results	16
2.4 Conclusions	24
Chapter 3: Sensitivity of System Morphology to Subgrid-Mixing Strength in Idealized Simulations of Radiative-Convective Equilibrium	27
3.1 Introduction	27
3.2 Model Simulations and Methodology	29
3.3 Results	32
3.4 Conclusion	45
Chapter 4: Multiscale Convective Circulations and Scale Interactions in a Global Storm-Resolving Model	47
4.1 Introduction	47
4.2 Model Setup and Datasets	49
4.3 Methods	51
4.4 Large-Scale Circulations and Mean Cloud Properties	56
4.5 Small-Scale Circulations and Upscale Impacts	62
4.6 Bidirectionality of Scale Interactions	68
4.7 Summary and Conclusions	73

Chapter 5: Summary of Dissertation and Conclusions	76
5.1 Synopsis of Dissertation	76
5.2 Concluding remarks	77
Bibliography	80

LIST OF FIGURES

Figure Number	Page
1.1 Projected changes to annual maximum daily rainfall under warming scenarios of a) 1.5°C ; b) 2.0°C ; and 4.0°C . Hatching indicates regions where fewer than 80% of models considered agreed on the sign of the change. Numbers on panels indicate number of models considered. Figure taken from the Sixth Assessment Report of the Intergovernmental Panel on Climate Change (IPCC-AR6; <i>IPCC</i> (2023)).	3
1.2 Reconstructed vertical mass flux evolutions associated with a) the Madden-Julian Oscillation; b) Equatorial Rossby Waves; c) Kelvin waves with periods ~ 10 days; d) Kelvin waves with periodicity of 3-4 days; e) Westward intertio-gravity waves; f) eastward intertio-gravity waves; and g) mixed Rossby-gravity waves. Mass flux values are normalized. Figure taken from <i>Inoue et al.</i> (2020)	6
2.1 Two precipitation features (PFs) over the Gulf of Martaban (Southeast Asia) identified via the method described in the text. Precipitation rates above (below) 10 mm/hr are colored red (blue). White dots indicate the principal (largest) core. Computed localizations (λ ; Eq. 3.3) are indicated in the title. PFs have similar sizes of a) 10,675 km and b) 10,125 km.	12
2.2 Cumulative distribution functions (CDFs) of PF maximum precipitation (MaxPr) values. CDF for oceanic (continental) PFs is shown in blue (red). The combined CDF is shown in black. The vertical line at 60 mm/hr indicates the minimum MaxPr value required for a PF to be classified as an extreme-generating PF (ExPF).	13
2.3 a) Probability distribution function (PDF) of both oceanic and continental PFs. b) The difference between PDFs of oceanic and continental PFs. Differences are reported as absolute differences in the PDF values and thus have units of percentage points.	15
2.4 Maps on 2° grids. Shading indicates a) the number of ExPFs recorded in our dataset; b) the conditional probability of ExPF occurrence, defined as the ratio of ExPFs that occur within a given location to the total number of PFs that occurred at that location; c) mean size of TyPFs at each location; d) mean size of ExPFs at each location; e) mean λ of TyPFs at each location; f) mean λ of ExPFs at each location. The maritime continent region (defined in Section 2.3.3) is highlighted in white	17

2.5	Average MaxPr for PFs composited by PF area and λ . White contour is drawn at 60 mm/hr contour.	19
2.6	Distribution of PF λ and the fraction of PF area taken by the principal core. A one-to-one line is plotted to aid discussion.	20
2.7	Fraction of PFs for which the rainiest pixel is contained within the principal core of the PF.	22
2.8	The average reflectivity (in dBZ) of a PF's rainiest pixels stratified by PF size and λ . Averages are taken over the indicated layers.	23
2.9	A schematic of the proposed coupling pathway between entrainment and morphology. In the case of (a) non-localized convection, the moistening of non-cloudy air by detrainment is less efficient because of the distance between convective elements. This causes the drying due to entrainment to have increased effectiveness in depleting buoyancy and hindering convection. In the case of (b) localized convection, the proximity of the convection allows detrainment to efficiently moisten the near-cloud environment of other convective elements, mitigating the buoyancy reduction associated with entrainment, and promoting stronger precipitation	25
3.1	Snapshots of the precipitation field taken on Day 50 of the simulation. Boundaries of convective systems are shown in black. Boundaries of precipitation cores shown in red.	29
3.2	Mean vertical profiles of TKE eddy diffusivity (Eq. 3.2) for each of the three model simulations. Averages are taken over whole model domain over length of simulation.	33
3.3	Vertical profiles of mean total turbulent kinetic energy (TKE) for each of the three simulation. Total TKE is the sum of both grid-scale (resolved) turbulence and subgrid-scale turbulence. Averages are taken over whole model domain over length of simulation.	34
3.4	Vertical profiles of mean vertical velocity within clouds for each model experiment. Clouds boundaries are identified by a threshold of 10^{-5} kg/kg for cloud water mixing ratio. Averages are taken over whole model domain over length of simulation.	35
3.5	As in Figure 3.4, but for in-cloud vertical mass flux.	36
3.6	Timeseries of mean surface heat flux (sensible heat flux plus latent heat fluxes) for each of the three experiments considered.	37
3.7	Mean vertical profiles of relative humidity (%) for each of the three model simulations. Averages are taken over whole model domain over length of simulation.	39

3.8	Mean vertical profiles of specific humidity (g/kg) for each of the three model simulations. Averages are taken over whole model domain over length of simulation.	40
3.9	a) A timeseries of number of precipitation systems for each simulation. b) Normalized density of convective system area over the entire model run.	41
3.10	Time series of the fractional coverage of rainy pixels ($> 0.1 \text{ mm/d}$ rain rate) for each model experiment.	42
3.11	Bin-mean values of MaxPr, stratified by feature size (x-axis) and localization λ (Eq. 3.3; y-axis).	42
3.12	Feature MaxPr composited by the size of the feature's principal core. Only bins with at least 10 features are considered.	43
3.13	Bin-mean vertical velocity (in isobaric coordinates) within principal cores of indicated size. Vertical velocities reported at a) 850 hPa; b) 500 hPa; and c) 200 hPa.	44
4.1	The red box above indicates the boundaries of our study domain.	50
4.2	First (a) and second (b) empirical orthogonal functions (EOFs) of large-scale vertical mass flux for gSAM (solid blue) and ERA5 (dashed black). The explained variance ratio for each mode is indicated in brackets.	52
4.3	a) Diagram showing the partitioning of the a_{strat} - a_{conv} plane into eight phases. The circle in the center shows the boundary of Phase 0, which comprises bins with $R_{cs} < 0.5$; b) the composite large-scale mass flux profile (\bar{M} ; Eq. 4.2) binned by θ_{cs} . The boundaries of each phase are indicated.	54
4.4	(Shading) Joint histogram of gSAM (top row) and ERA5 (bottom row) in the a_{conv} - a_{strat} plane. Bin-mean tendencies a_{strat} and a_{conv} are shown as arrows. Backward differences (a,d) show the evolution over the preceding 3 hours, with arrow heads located at bin center; forward differences (b,e) show the evolution over the subsequent 3 hours, with arrow tails located at bin center; and centered differences (c,f) represent the mean evolution over a 6 hour centered period, with arrow midpoints located at bin center.	56
4.5	Transition frequencies over a 6-hour centered period for (a) gSAM and (b) ERA5. The shown frequencies indicate the conditional probability that a large-scale domain that is in the indicated initial phase at t -3hr will transition to a given final phase at $t + 3\text{hr}$	58
4.6	(a-b) Bin-average of large-scale precipitation derived from (a) gSAM and (b) CMORPH observational dataset; (c-d) bin-average of large-scale precipitable water (PW) from (c) gSAM and (d) ERA5 Reanalysis.	59

4.7	As in Fig. 4.6, but with cloud radiative effects (CRE) binned by a_{conv} and a_{strat} . Top row: Bin-composite values of (a) longwave CRE; (b) shortwave CRE; and (c) net CRE in gSAM. Bottom row: CERES values of (d) longwave CRE; (e) shortwave CRE; and (f) net CRE. Averages over all bins displayed	60
4.8	Composite means of sub grid-scale vertical velocity (shading) and moisture-space circulation ψ (contours). Profile of mean vertical velocity is also shown. Data are averaged over 5 columns to reduce the noisiness of the sub grid-scale vertical velocity.	63
4.9	As in Figure 4.3, but with shading of moist static energy.	65
4.10	Profiles of Phase-averaged saturation MSE (red), mean MSE (black), and the mean MSE of columns in the 95th percentile of column saturation fraction ($\eta > 0.95$; Sec. 34.3.3)	66
4.11	As in Figure 4.9, but with shading of combined cloud water and ice mixing ratio.	67
4.12	(a-c) Composite large-scale vertical mass flux profiles of domains that either advance; (d-f) Composite difference in cloud water and ice mixing ratio between domains undergoing advancing transitions and persistence.	69

ACKNOWLEDGMENTS

I first wish to acknowledge the support of my two advisors, Daehyun Kim and Peter Blossey. Both have served as patient mentors, skilled teachers, and inspiring collaborators during my graduate studies. I am grateful to them for their generosity with their time, and for the countless useful insights they have shared with me over the years.

I wish also to thank the groupmates of the Kim/Blossey group, past and present, who I have had the joy of speaking with and learning from. I particularly want to thank Mu-Ting Chien (my academic twin) for the many thought-provoking conversations about both research and life we have had. I also want to thank Spencer Ressel and Nelly Emlaw for their support and help in preparing my thesis defense. I also wish to thank the members of the Convective Systems/Tropical Dynamics Laboratory at Seoul National University for being gracious hosts during a visit I made to SNU in November of 2024. It was on this trip to SNU that much of what now forms Chapter 2 of the present dissertation was completed.

Finally, I wish to thank my wife, Melanie, for her inexplicable (to me) and unwavering support throughout the entirety of my graduate studies. It is hard for me to imagine having completed my doctorate without her by my side. In our junior year of our undergraduate studies, she said to me that she expected an acknowledgment in my PhD thesis as “my wife”. Well, here you go.

Chapter 1

INTRODUCTION AND THESIS OUTLINE

Moist atmospheric convection is one of the most spectacular phenomena on Earth. Through the condensation of atmospheric water vapor into a mist of small water droplets and ice crystals, the typically transparent atmosphere is injected with a dizzyingly diverse population of clouds and convective weather systems, as well as a vertical pulse of diabatic heating that can drive changes to the circulation over large ranges. Over the past twenty years, there has been mounting evidence that tropical convective systems and their associated clouds, through interactions with radiation, moist thermodynamics, and dynamical circulations, are a part of *and have an influence on* the circulations that characterize the large-scale flows observed in the tropics. In other words, a growing body of work rejects viewing tropical convective systems (with horizontal scales on the order of $\mathcal{O}(10 \text{ km} - 100 \text{ km})$) as being either completely *independent* of large-scale circulations (meaning $\mathcal{O}(1000 \text{ km})$), as well as the view that convection is completely *controlled* by large-scale motions. Rather, contemporary studies suggest there is a multifaceted coupling between the two scales of motion, whereby large-scale circulations emerge (in some sense) from smaller-scale convective activity, while the small-scale convection is itself sensitive to large-scale conditions that can be changed by large-scale circulations (*Emanuel et al.*, 1994; *Mapes*, 1997, 1998; *Raymond*, 2000; *Arakawa*, 2004; *Bretherton et al.*, 2004)

This view is not new; quite to the contrary, advocacy for some version of a “scale interaction” picture for tropical convection can be seen in many studies conducted shortly after the development of robust observational networks in the region during the Pacific theater of the Second World War. Such a view, whereby intermediate scales of motion between the smallest cumulus updrafts and large-scale stationary forcings (so-called mesoscales) play a role in the overall circulation of the tropical atmosphere, represents a departure from the more classical (and very successful) paradigm of quasi-geostrophy (QG) developed and em-

ployed in understanding the dynamics of the midlatitude atmosphere. Clarence Palmer, in an 1956 survey of the insights garnered about tropical weather since the war, summarized the development of tropical meteorology thusly (*Palmer*, 1952):

The history of research in tropical meteorology during the past twenty years could be summed up as an account of struggle ; the struggle to free the science from the domination of concepts derived from the study of weather in high latitudes.

In particular, the framework of QG used in midlatitude dynamics is based around a clear scale separation, made quantitative in the form of asymptotic expansions of the dynamical equations in terms of the Rossby number $Ro = U/fL$, where U is the typical zonal wind, f the Coriolis parameters, and L a characteristic length scale. Under QG, motions on scales comparable to or larger than $L = U/f$ (the so-called Rossby deformation radius) can be taken to be driven by the conservation of potential vorticity, with buoyancy effects being of second order (defined in terms of an asymptotic series expansion) importance *Pedlosky* (1987); *Holton and Hakim* (2013). The distinct character of the tropical atmosphere can be glimpsed even from this abbreviated summary of the QG framework by noting that as $f \rightarrow 0$, $Ro \rightarrow \infty$, indicating that vorticity-driven circulations and buoyancy-driven circulation are not scale-separated in the equatorial region. While there are certainly analogies between the tropical and extratropical atmosphere (for example, a so-called *equatorial Rossby radius* can be obtained in a formally similar context as in QG dynamics, as in *Matsuno* (1966)), both theoretical and observational evidence acquired over the last 75 years supports the notion that the dynamics of the tropical atmosphere are more non-linear, and less scale-separated, than the extratropical motions, making the applicability of QG dynamics questionable for the tropical atmosphere.

In the remainder of this Introduction, I will describe two examples of problems in tropical metrology where the interaction across scales is of particular significance. The first is the problem of determining necessary and sufficient conditions for the generation of extreme rainfall rates; the second is the problem of relating the evolution of large-scale vertical motions of the tropical atmosphere to the structure and evolution of smaller-scale convective

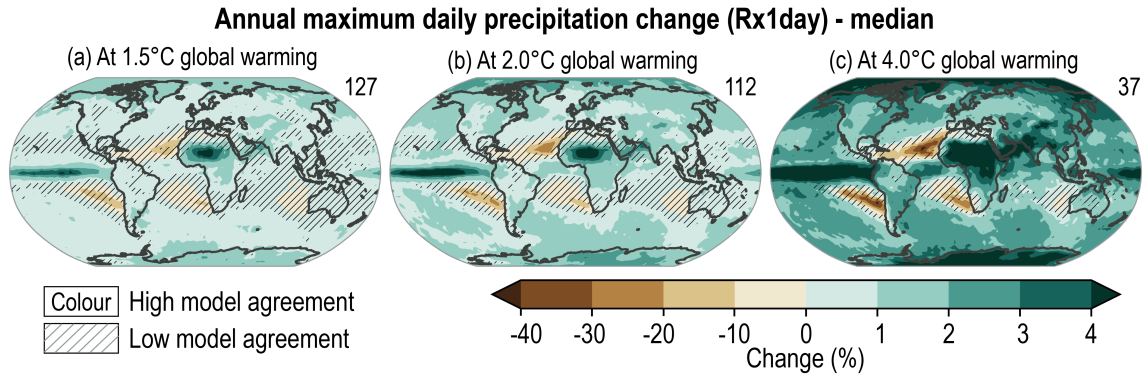


Figure 1.1: Projected changes to annual maximum daily rainfall under warming scenarios of a) 1.5°C; b) 2.0°C; and 4.0°C. Hatching indicates regions where fewer than 80% of models considered agreed on the sign of the change. Numbers on panels indicate number of models considered. Figure taken from the Sixth Assessment Report of the Intergovernmental Panel on Climate Change (IPCC-AR6; *IPCC* (2023)).

circulations and clouds. The former question is addressed in Chapters 2 and 3 of this dissertation, while the latter question is the subject of Chapter 4.

1.1 Scale Interactions and Extreme Instantaneous Rainfall

The notion of “extreme precipitation” refers to the top percentile events (in terms of precipitation production) that occur over some region. Such events are known to cause flooding, mudslides, and other societally relevant disasters. A survey of climate model projections performed as part of the Sixth Assessment Report of the Intergovernmental Panel on Climate Change (*IPCC*, 2023) indicates that the impact of global warming on changes in the intensity of extreme precipitation events in the tropics remains poorly constrained by models (Fig. 1.1). As such, improving the understanding of the processes involved in the generation of tropical precipitation extremes remains a worthwhile goal with scientifically and societally relevant implications.

Observational and modeling studies have shown that the answer to the question of “what processes are responsible for the generation of extreme precipitation events?” depends at least partly on the definition of “extreme precipitation”. This choice, in turn, is associated with a particular set of spatio-temporal scales of atmospheric motion that will be most

relevant to generating precipitation at the scales considered. As an example, consider extremes of daily precipitation accumulations (e.g., top 5% events). For this definition, global observational studies have shown that the primary drivers of such extreme precipitation are long-lived mesoscale convective systems *Roca and Fiolleau* (2020); *Tsai et al.* (2025). In models, an analogous result holds; the phenomenon of “self-aggregation” by convection in numerical models with homogeneous boundary conditions (see *Wing and Cronin* (2016) for a review) has been shown to be associated with extreme precipitation accumulations, in large part because of the steadiness of the location of the aggregated convective state *Bao et al.* (2017); *O'Donnell and Wing* (2024). In other words, it has been shown that the organization of convection, either in numerical models in the form of self-aggregation or in observations in the form of coherent mesoscale convective systems, is a strong determining factor in the generation of daily extreme precipitation.

For the case of extreme *instantaneous* precipitation, however, the case is less clear. For example, *Bao and Sherwood* (2019) used idealized modeling to argue that instantaneous precipitation rates are largely unaffected by the degree of convective organization. More recently, *O'Donnell and Wing* (2024) computed correlations between the degree of spatial organization (quantified by I_{org} as defined in *Tompkins and Semie* (2017); see the introduction of *Sakaeda and Torri* (2022) for a contemporary synopsis of such organization indices) and precipitation rate, computed at different coarsening length and time scales. They found a positive correlation, indicating an enhancement of precipitation rates associated with organization, for both daily and instantaneous timescales.

In observations, tropical precipitation extremes are often studied using orbiting satellites, such as the Global Precipitation Mission (GPM, *Iguchi et al.*), which inherently observe instantaneous precipitation rates. A recent study (*Xu et al.* (2022)) found that a large fraction (over the oceans a majority) of convective features that generate extreme precipitation rates contain relatively weak convection (as measured by the depth of the vertical radar profile). This and other studies (*Hamada et al.* (2015); *Zipser and Liu* (2021)) raise the question of whether and how other factors, besides the strength of the vertical motions, of a convective system may modulate the likelihood of an extreme rainfall event occurring.

It is this question which is addressed in Chapters 2 and 3 of this thesis. In Chapter 2 we

use observations from the GPM satellite to identify tropical precipitation features. The multiscale structure of these features is then quantified using two simple morphological indices: the area of the feature, which we identify as a measure of the feature-scale organization; and an index termed the *localization* of the feature, which quantifies the extent to which the precipitation in the feature is spatially centered or distributed. We show that the morphology of the feature does impact the probability of the feature generating an extreme rainfall event. We further present evidence of moisture entrainment acting as a pathway coupling feature morphology to precipitation production. In Chapter 3 we further investigate this hypothesized coupling pathway by performing a set of modeling experiments with differing subgrid mixing strengths. We examine the impact that this change on the morphology of the systems and the relationship between morphology and precipitation extremes. We show that the domain-average structure of convection was indeed modulated by changes in the strength of subgrid mixing. We also find that the model experiments with stronger mixing tended to generate a larger number of smaller features. While we also find that these models do exhibit coupling between a feature’s morphology and maximum precipitation rate, we find that this coupling is largely unaffected by changes in the subgrid mixing strength.

1.2 Scale Interactions and Large-Scale Vertical Circulations

The space-time variability of convective proxies (such as brightness temperature or precipitation) has been studied using global observations of the tropics *Takayabu* (1994); *Wheeler and Kiladis* (1999)). Such Spectral analysis of equatorial convection typically quantified via brightness temperature or precipitation) has revealed peaks in regions of the spectral space that align with dispersion curves predicted by the linear wave theory of shallow water on a beta plane *Takayabu* (1994); *Wheeler and Kiladis* (1999). Such peaks include Madden-Julian Oscillation *Zhang* (2005); *Jiang et al.* (2020), Kelvin Waves *Chien and Kim* (2023), and Equatorial Rossby Waves *Fuchs-Stone et al.* (2019). These coherent peaks in the spectral power of convection motivate the term “convectively coupled equatorial waves” (CCEWs; see *Kiladis et al.* (2009) for a review). The passage of CCEWs has been linked to extreme precipitation events *Hermawan et al.* (2022); *Senior et al.* (2022); *Cheng et al.* (2023), and are principal drivers of subseasonal variability in the tropics.

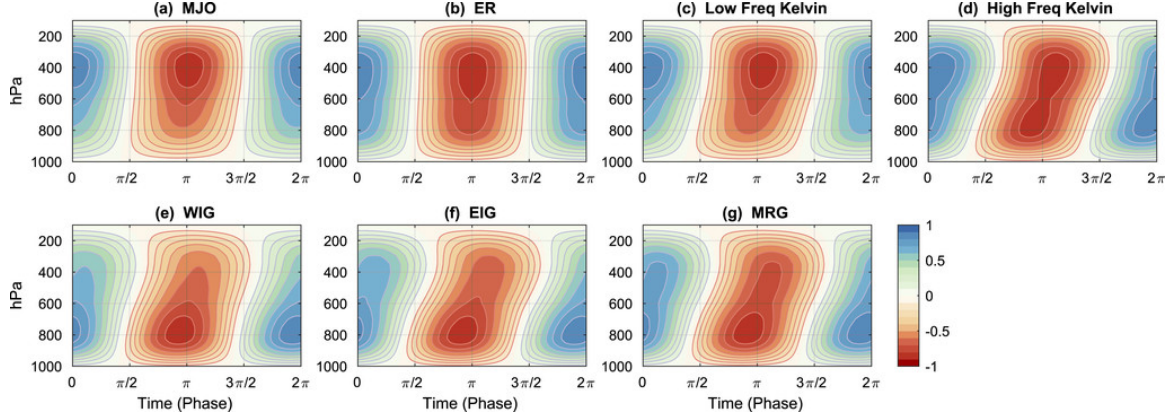


Figure 1.2: Reconstructed vertical mass flux evolutions associated with a) the Madden-Julian Oscillation; b) Equatorial Rossby Waves; c) Kelvin waves with periods ~ 10 days; d) Kelvin waves with periodicity of 3-4 days; e) Westward intertio-gravity waves; f) eastward intertio-gravity waves; and g) mixed Rossby-gravity waves. Mass flux values are normalized. Figure taken from *Inoue et al.* (2020)

CCEWs are also associated with circulation patterns that can be extracted from global reanalysis data (*Adames and Wallace*, 2015; *Inoue et al.*, 2020). In particular, *Inoue et al.* (2020) calculated the composite vertical motions associated with different classes of CCEWs, noting that different waves had different shaped vertical motion profiles. The shape of the vertical mass flux, in particular its degree of top- or bottom-heaviness, has been shown to impact the energetic import or export of circulations by modulation of the so-called “gross moist stability” *Neelin and Held* (1987); *Back and Bretherton* (2009); *Raymond et al.* (2009); *Inoue et al.* (2020, 2021); *Masunaga* (2023); *Masunaga and Takahashi* (2024). Therefore, understanding how the vertical velocity profiles of these large-scale circulations evolve is critically important to understanding the overall energetics of these scales of motion.

Multiple studies have shown that the majority of variance in these vertical motions can be explained by two sinusoidal structures: the gravest mode, with a half-wavelength spanning the depth of the troposphere; and a secondary mode with wavelength equal to the troposphere’s depth *Back and Bretherton* (2009); *Back et al.* (2017); *Inoue et al.* (2020). These modes have been associated with deep convection and stratiform anvils, respectively. Furthermore, while the role of cumulus convection in mediating the majority of tropical ver-

tical mass flux has been noted since the pioneering study of Riehl and Malkus in 1958 *Riehl* (1958), efforts to connect directly the structure of small-scale clouds to the structure and evolution of large-scale vertical circulations has historically been hindered by the coarseness of global models. However, modern computing techniques have allowed for the development of global storm-resolving models, capable of resolving both large- and small-scale vertical motions simultaneously *Satoh et al.* (2019); *Stevens et al.* (2019). These models provide a novel avenue for exploring how convective and clouds couple disparate scales of motions. Chapter 4 of this thesis utilizes such a model to document evidence of interactions across scales in the development and lifecycle of large-scale vertical motions, and the roles played by both large- and small-scale structures in modulating the evolution of large-scale vertical motions. Particular focus is paid to the question of which scale, if any, dominates the determination of the large-scale evolution.

Chapter 2

THE ROLE OF MORPHOLOGY IN EXTREME-PRODUCING TROPICAL PRECIPITATION SYSTEMS

2.1 Introduction

In the tropics, precipitation is generated by a diverse and ever-replenishing population of rain-generating cloud clusters. These clusters range in scales and intensities. Shallow convective showers are one regime; deep convective downpours another; and broad-scale stratiform rain yet another. These rain events are often associated with, but are not the same as, organized convective systems. For example, a single tropical squall line (a particular mode of organized convection) may contain clusters in all three of the aforementioned precipitation regimes within it *Houze* (1997). Furthermore, recent observations have shown that sub-regions of broad-scale convective systems (viz. mesoscale convective systems; see *Houze* (2018) for a contemporary review) undergo evolution and transition between different precipitation regimes, which has implications for the evolution of the three-dimensional (horizontal and vertical) dynamical structure and evolution of the system (*Mapes et al.*, 2006; *Masunaga and Takahashi*, 2024). This coupling between precipitation and the structure of convective circulations has been long identified as an important but poorly understood component of dynamical theories of tropical precipitation, particularly on the scales of organized convective systems (*Mapes*, 1997; *Arakawa*, 2004).

This paucity of understanding regarding the relationship between precipitation and the structure of convection is particularly troubling in the context of extreme precipitation. In particular, observational studies utilizing space-borne, global observations of tropical precipitation have documented the fact that extreme tropical (instantaneous) rainfall rates are not always associated with very strong or deep convection (*Hamada et al.*, 2015; *Xu et al.*, 2022). Instead, regions of extreme rainfall (quantified as rain rates exceeding 60 mm/hr in *Xu et al.* (2022)) are often an order of magnitude smaller in spatial extent (\sim 10

km) than the larger rainy regions in which they are embedded (~ 100 km). Observations show that these extreme-generating parent rainy regions are often not characterized by very deep or strong convection.

This (relatively recent) observation about tropical precipitation extremes is unfortunately not well explained by contemporary descriptions of the coupling between precipitation extremes and circulation. In particular, a large body of work has made remarkable advances have been made in developing a diagnostic framework for understanding changes to tropical convective extremes with global warming (*O’Gorman and Schneider*, 2009; *Muller et al.*, 2011). However, this framework was intended for (and has primarily been utilized on) stationary and very localized deep convection, as occurs in idealized numerical simulations of convection (viz. self-aggregated convection; the reader is directed to *Wing et al.* (2017) for a review of the phenomenon of convective self-aggregation). The spatial organization of convection is thus not explicitly considered in this framework. As such, the spatial inhomogeneity of precipitation, even within an organized convective system, is also not represented. Furthermore, convection is modeled as a moist adiabatic parcel process; as such, the vertical structure of convection is completely determined by the temperature and humidity profiles of the environment. The interactions of different convective elements is thus “integrated out” in this framework. It follows then that such a vertical profile-based model is best suited for stationary or quasi-stationary convective configurations; at the same time, it is an ill-suited framework for understanding the role of spatial organization of observed tropical precipitation, or the role of such organization the generation of tropical precipitation extremes.

Despite this, prior studies have indeed found compelling evidence that the organization of convection plays a role in determining the location and intensity of precipitation extremes. Historically, both extremes of daily accumulated precipitation (as measured by e.g. rain gauge networks) and instantaneous precipitation rate (as measured by e.g. satellite observations) have been termed “extreme precipitation events”. In terms of daily accumulated precipitation, the connection between convective organization and precipitation extremes has been well established in both model and observational studies. In particular, idealized modeling studies have shown that self-aggregated convection increases the intensity

of daily precipitation accumulation in a range of modeling setups (*Bao et al.*, 2017; *Bao and Sherwood*, 2019; *O'Donnell and Wing*, 2024). This intensification of daily precipitation accumulations is due to self-aggregated convection's tendency to be more stationary than disaggregated convection, resulting in regions with sustained rainfall and thus greater precipitation accumulations. Similarly, in observations, extremes of daily rain accumulations are strongly associated with organized mesoscale convective systems (*Roca and Fiolleau*, 2020). Furthermore, global studies have shown that when convection over the tropical belt as a whole is more organized (as computed via the organization index I_{org} ; the reader is directed to the introduction of *Sakaeda and Torri* (2022) for a review of examples of such organization indices), daily precipitation accumulations increase as well (*Bao et al.*, 2024).

In the case of extreme *instantaneous* precipitation, however, the link between the spatial organization of convection and extreme rainfall is not as well established. An idealized model study that demonstrated a positive relationship between convective aggregation and extreme daily precipitation also showed an invariance of extreme precipitation rates to convective aggregation (*Bao and Sherwood*, 2019). The authors of that study suggested that microphysical interactions, particularly hydrometeor loading, may have played a key role in maintaining the instantaneous precipitation rate unchanged as the convection aggregated. In a more recent model ensemble study, *O'Donnell and Wing* (2024) demonstrated that not only is the correlation between organization (I_{org}) and accumulated precipitation is most strongly positive for daily time scales, the correlation weakens but remains positive for shorter time scales, extending to instantaneous precipitation rates. Besides modeling, observational studies have also reached mixed results in understanding the role of convective organization and instantaneous precipitation extremes. For example, *Semie and Bony* (2020) used instantaneous satellite observations to show that within square tropical domains, the domain-mean precipitation rate decreases with organization (I_{org}), but the mean precipitation rate within the rainy regions is increased. This suggests that convective organization may serve to enhance instantaneous precipitation rates within the bounds of a precipitation system. Similarly, *Angulo-Umana and Kim* (2023) showed that tropical mesoscale (2°) square domains that are more organized (greater I_{org}) also experience more intense rainfalls; they further showed that this result holds between domains with similar

spatial coverage of convection and column moisture, indicating that organization *per se* serves to enhance instantaneous precipitation rates. However, these two studies did not resolve the role of organization within convective systems; that is, they defined organization and precipitation statistics in terms of averages over square domains; the organization of precipitation into coherent features, and the role of the sub-feature organization, was not directly considered in either *Semie and Bony* (2020) or *Angulo-Umana and Kim* (2023), who quantified organization based on the distribution of pixel values within the study domain.

Recently, (*Carenso et al.*, 2024) used both model and observational products to argue that the “morphology” of rain events (quantified in their paper by the rainy area fraction and the upper quartile of rain rates within the event) determines whether the given rain event is extreme in terms of accumulation, instantaneous rain rate, or both. This study suggests the importance of spatial structure of rainfall events in the generation of extreme events.

The purpose of this study is to establish a link between the morphology of tropical precipitation features and the generation of instantaneous extreme rainfall. In Section 2 we will detail the precipitation data used in this study; we will further define the spatial statistics we use to characterize the morphology of precipitation features in observations. In Section 3 we will examine how these morphological properties of precipitation features modify the intensity of rainfall and the risk of extremes occurring. We also offer some insight into the role of morphology in the vertical structure of precipitation features. Conclusions and final remarks are provided in Section 4.

2.2 Data and Methods

2.2.1 Identifying precipitating systems in GPM

Our observations of tropical precipitation features (PFs hereafter) will come from version 7 of the Global Precipitation Mission’s space-borne Ku-Band Precipitation Radar (GPM-PR; available from <https://gpm.atmos.washington.edu/>). This dataset is comprised of a series of snapshots along the GPM-PR observational swath, which has a width of 245 km. Each snapshot is provided on a regular grid with $0.05^\circ \times 0.05^\circ$ ($\sim 5\text{km} \times 5\text{km}$) horizontal spacing.

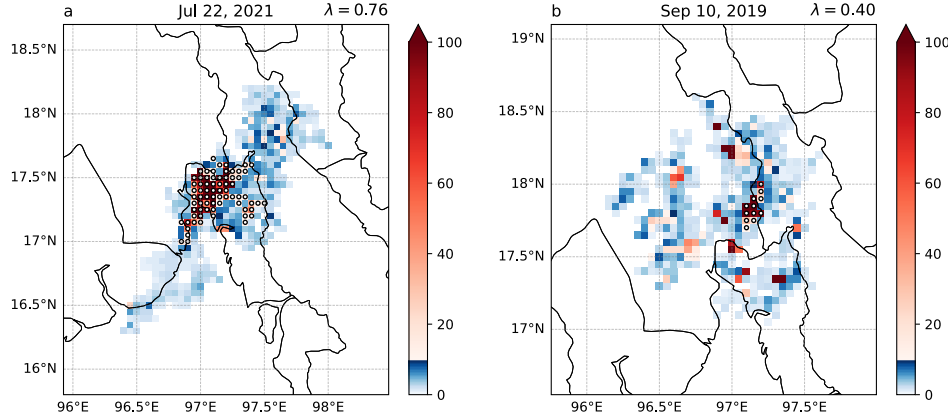


Figure 2.1: Two precipitation features (PFs) over the Gulf of Martaban (Southeast Asia) identified via the method described in the text. Precipitation rates above (below) 10 mm/hr are colored red (blue). White dots indicate the principal (largest) core. Computed localizations (λ ; Eq. 3.3) are indicated in the title. PFs have similar sizes of a) 10,675 km and b) 10,125 km.

Each pixel contains a vertical profile of radar reflectivity, as well as a retrieval of near-surface rain rate (*Iguchi et al.*, 2000). Thus, GPM-PR allows for both a characterization of the horizontal and vertical structure of tropical PFs. Furthermore, using GPM allows us to directly target precipitating systems, unlike other studies which have utilized less-direct measures of convective intensity to identify systems, such as brightness temperature (as used in *Roca et al.* (2014); *Feng et al.* (2021)).

To identify PFs, we begin by identifying contiguous areas of at least 100 km² (4 GPM pixels) with rain rates exceeding 1 mm/hr. We further require that each PF considered contain at least one pixel with a rain rate exceeding 10 mm/hr. This is meant to restrict our study to only those PFs that contain active convection. Contiguous regions of precipitation values exceeding 10 mm/hr (of any size) will be termed “cores” in this study. Thresholds of 5mm/hr or 20 mm/hr yields qualitatively similar results (not shown). To avoid truncation effects, only PFs that are completely enclosed within the GPM-PR swath are considered in the present study. Although this reduces the pool of PFs we can consider in the present study, the GPM-PR swath has been found to be sufficiently wide to adequately sample the

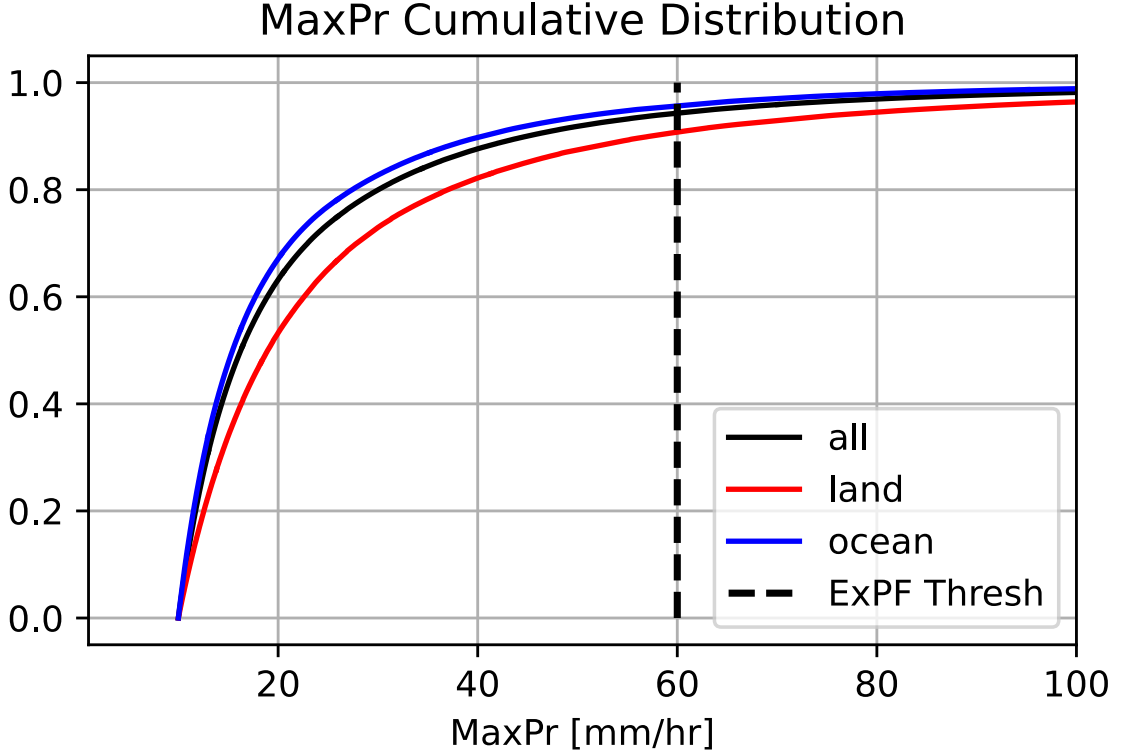


Figure 2.2: Cumulative distribution functions (CDFs) of PF maximum precipitation (MaxPr) values. CDF for oceanic (continental) PFs is shown in blue (red). The combined CDF is shown in black. The vertical line at 60 mm/hr indicates the minimum MaxPr value required for a PF to be classified as an extreme-generating PF (ExPF).

size distribution of tropical PFs *Nesbitt et al.* (2006). The date range of data analyzed extends from January 1, 2015 to December 31, 2024. In that range, we identified 1,130,057 PFs in total. Examples of two such PFs are shown in Fig. 2.1.

2.2.2 Identifying extreme-generating precipitation features

Since we are interested in understanding the role of morphology in generating extreme precipitation events, we will define “extreme-generating precipitating features” (ExPFs) as PFs with a maximum precipitation rate (MaxPr) value exceeding 60 mm/hr. This threshold corresponds approximately to the 95th percentile of global MaxPr values considered

(Fig. 2.2). This threshold is applied to all PFs regardless of whether the PF is oceanic or continental. This threshold is also identical to the one used by *Xu et al.* (2022) to define extreme precipitation. In all we identify 70,588 ExPFs. We note that a greater fraction of continental PFs are extreme under this threshold than oceanic (Fig. 2.2).

In contrast to ExPFs, we also define typical PFs (TyPFs) as PFs with MaxPr values in the interquartile range; that is, the middle 50% of PFs by MaxPr. Thus TyPFs are PFs that are generating non-trivial intensities of precipitation, but not to the level of ExPFs. TyPFs therefore serve as a comparison to ExPFs.

2.2.3 Characterizing Feature Morphology

There exists a wide range of morphological measures that have been proposed for the study of tropical convective systems (see the introduction of *Sakaeda and Torri* (2022) for a review of several such metrics). For our study, we are primarily interested in describing both the spatial extent and the spatial arrangement of the precipitation field within a given PF. Therefore, we will use two simple morphological measures to describe each PF.

The first morphological quantity we will compute for each PF is simply the area of the PF (measured in km^2), which we take as a quantification of the degree of feature-scale organization. This association has a physical basis, as the stratiform anvils of deep convective systems constitute a large fraction, and often majority, of the total area coverage of tropical convective systems (*Houze*, 1997, 2004). Since this anvil structure is a critical component of the so-called “organized,” system-scale overturning circulations associated with deep convective systems (*Lafore and Moncrieff*, 1989; *Houze*, 2018), the association between PF size and organization is well-motivated, at least on the length scales ($O(10^2\text{-}10^4 \text{ km}^2)$) considered in the present study.

The second way we characterize system morphology is by quantifying how centralized the feature’s precipitation production is. If most of the feature’s precipitation is being generated in a spatially limited portion of the feature, as opposed to being evenly distributed, then we say that this reflects a greater degree of spatial *localization* in the feature’s convection. Thus localization is a qualitatively similar notion to what has been termed “convective

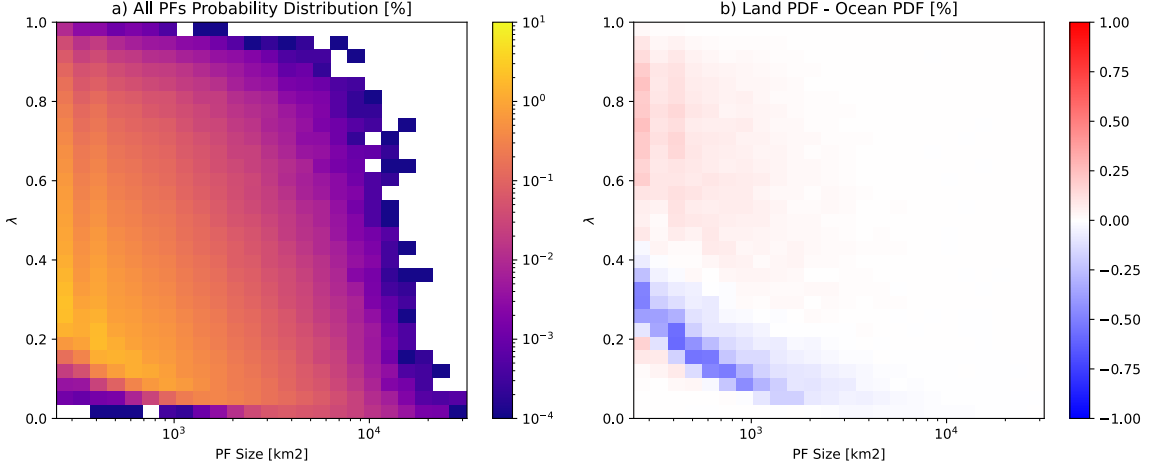


Figure 2.3: a) Probability distribution function (PDF) of both oceanic and continental PFs. b) The difference between PDFs of oceanic and continental PFs. Differences are reported as absolute differences in the PDF values and thus have units of percentage points.

organization” or “aggregation” in the literature.

To quantify the degree of localization, first the precipitation field within a PF is segmented into cores (pixels with >10 mm/hr rain rate). We note that by our definition of the PF, we are guaranteed at least one core exists for every PF, so that the localization is well-defined for all PFs considered in our study. The largest core within the PF is termed the “principal core”. We then define the *localization* λ as the fraction of the total PF precipitation that is generated by the principal core:

$$\lambda = \frac{\text{Precipitation due to principal core}}{\text{Total precipitation}}. \quad (2.1)$$

Thus, a PF with a single dominant core (e.g., Fig. 2.1a) will have a higher λ than a PF with several, similarly rainy cores (e.g., Fig. 2.1b)

Figure 2.3a shows the joint distribution of PF area and λ for the whole population of PFs. We can see that there is a weak but discernible negative correlation between PF size and λ , indicating that larger features tend to be less localized than smaller ones, which accords with the observation that a large amount of PF areal extent is due to the weakly raining but spatially expansive stratiform anvil (Ahmed and Schumacher, 2015). However, there is substantial spread around this correlation, so that for any given size there are many different

values of λ realized. Furthermore, the computed Pearson r value ($r = -0.33$) indicates the two variables can explain only about ~ 10 percent of each other's total variance. This motivates us to consider our two morphological parameters of size and λ as being largely independent, at least in the sense that we can take any combination of PF size and λ as an equally probable (if not equally likely) realization of a tropical PF's morphology.

A similar distribution as in Fig. 2.3a is seen for oceanic and continental PFs analyzed separately (not shown). The difference between the PDF of continental and oceanic PFs is shown in Fig. 2.3b. A band of negative values corresponding to small ($< 10^3$ km) and weakly localized ($\lambda < 0.5$) PFs indicates that such PFs are more common over the oceans than over land. Similarly, a broader region of positive values for small but more strongly localized ($\lambda > 0.5$) PFs indicates that such PFs are more common over land than ocean. We note that PFs of such sizes are the vast majority of PFs (Fig. 2.3a). Figure 2.3b thus indicates that oceanic PFs tend to be less localized than similarly sized continental PFs. However, the difference between the two distributions is modest ($\approx 1\%$), so for both oceanic and continental PFs we also assume that PF area and λ are essentially independent.

2.3 Results

2.3.1 Global morphology of extreme precipitation systems

Having defined the criterion for identifying PFs, TyPFs, and ExPFs, as well as the morphological statistics we will use to characterize them, we now examine the global populations of ExPFs. Figure 2.4a shows the global distribution of ExPFs. We observe that there is a large concentration of ExPFs within the equatorial Intertropical Convergence Zone, as well as over the western Pacific ocean and Indo-Pacific Warm Pool region. Computing the fraction of all PFs that occur over a given point that are ExPFs, we can quantify the conditional probability of ExPF occurrence over a given region (Fig. 2.4b). We note that there is stark land/ocean contrast, with ExPFs constituting a larger fraction of continental PFs than oceanic PFs.

Turning to the morphologies of these systems, we observe that there is not a clear land-ocean contrast in the morphologies of either ExPFs or TyPFs. Neither PF size (Fig.

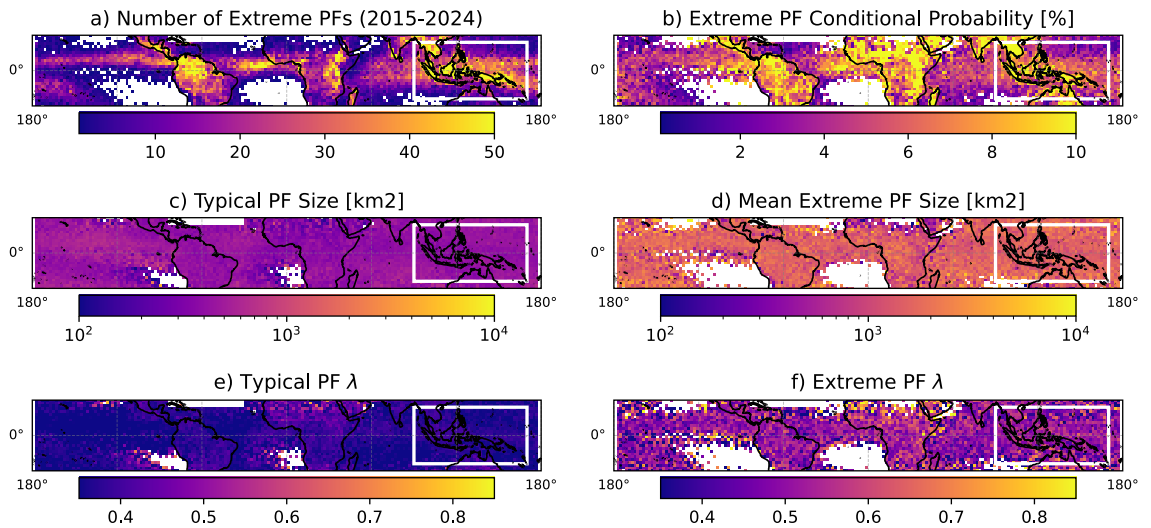


Figure 2.4: Maps on 2° grids. Shading indicates a) the number of ExPFs recorded in our dataset; b) the conditional probability of ExPF occurrence, defined as the ratio of ExPFs that occur within a given location to the total number of PFs that occurred at that location; c) mean size of TyPFs at each location; d) mean size of ExPFs at each location; e) mean λ of TyPFs at each location; f) mean λ of ExPFs at each location. The maritime continent region (defined in Section 2.3.3) is highlighted in white

2.4c,d) nor λ (Fig. 2.4e,f) exhibits a clear land-ocean contrast. However, we see a stark difference between ExPFs and TyPFs in the mean size and λ of each respective PF type. In particular, ExPFs are on average much larger (Fig. 2.4c,d) and more localized λ (Fig. 2.4e,f) than TyPFs. This indicates that, globally, extreme precipitation events (precipitation rates exceeding 60 mm/hr⁻¹) are most associated with precipitation features that are both larger and more localized than average.

Since both the size of the PF and the value of λ can be associated with some notion of convective organization, albeit at different length scales, we can interpret Figure 2.4 as showing that extreme instantaneous precipitation events are associated with an increased degree of convective organization. This finding is concordant with previous studies that concluded that precipitation extremes are generally enhanced by an increase in the organization of convection (*Pendergrass et al., 2016; Roca and Fiolleau, 2020; Semie and Bony, 2020*). However, the dual importance of both PF size and λ suggests that the organization of convection at both the scale of precipitation features, as well as its smaller-scale spatial arrangement, plays a role in determining which precipitation features generate extreme events.

2.3.2 How does morphology impact extreme precipitation?

To probe the ways in which feature morphology impacts the production of extreme precipitation events, we compute the average MaxPr for PFs binned by their area and λ (Fig. 2.5). The distributions are similar for both continental and oceanic PFs separately (not shown). As expected from Figure 2.4c-f, MaxPr generally increases with both size and λ for both land and ocean PFs. For PFs of a given size, those that are more localized (larger λ) have on average much greater MaxPr than those that are less localized; similarly, for a given localization λ , larger PFs have on average a higher MaxPr than smaller PFs. We further observe that the sensitivity of MaxPr to λ increases with PF size; that is, the MaxPr of larger PFs increases more quickly with λ than the MaxPr of smaller PFs.

To gain further insight into the role of localization in the generation of ExPFs, we compute the joint distribution of localization λ , and the fraction of PF area taken up by the

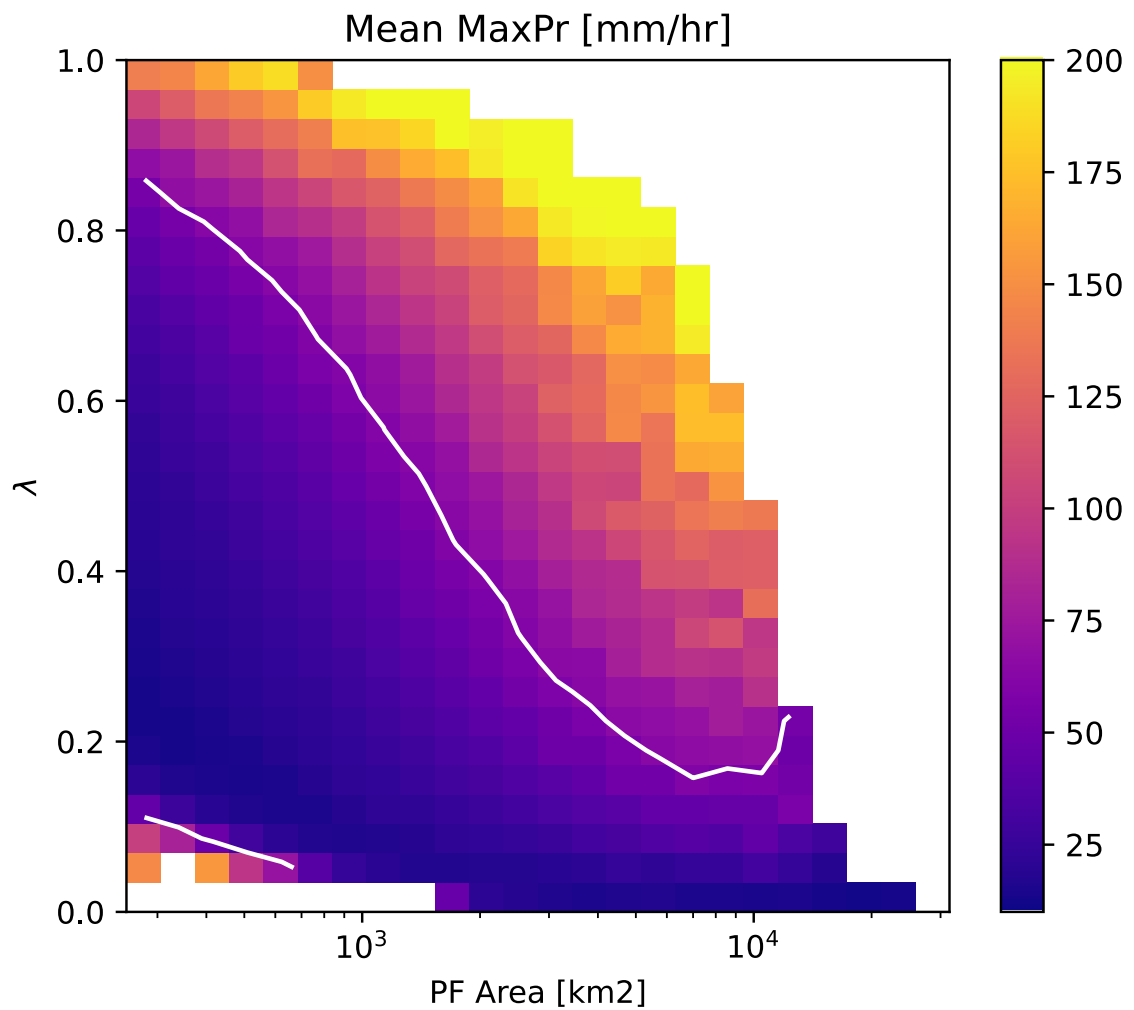


Figure 2.5: Average MaxPr for PFs composited by PF area and λ . White contour is drawn at 60 mm/hr contour.

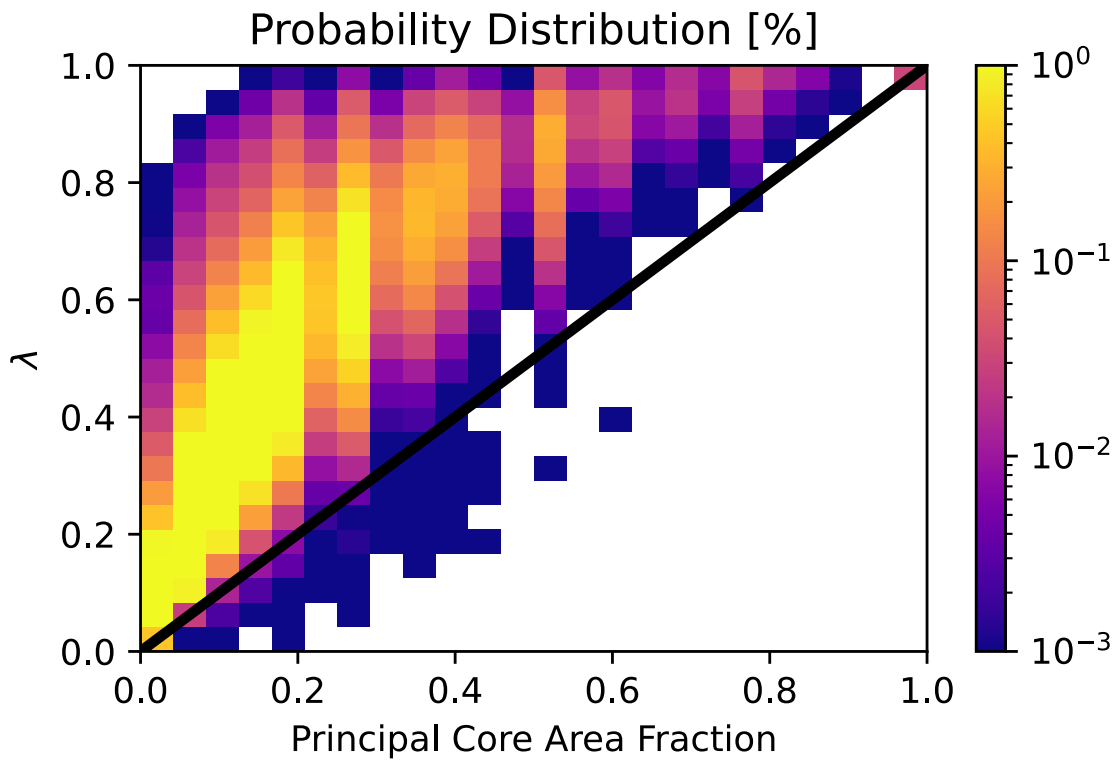


Figure 2.6: Distribution of PF λ and the fraction of PF area taken by the principal core. A one-to-one line is plotted to aid discussion.

principal core (Fig. 2.6). If the spatial arrangement of precipitation were immaterial, then we would expect that the fractional precipitation contribution from a core (i.e. λ) would scale as the fractional area of that core. However, we see that increasing the areal fraction of a given PF's principal core has an outsized effect on the fraction of precipitation generated by that core. This thus suggests that increasing the areal fraction of the principal core of a PF will increase the precipitation production of the core by a greater proportion than its growth in areal extent. We speculate that this additional enhancement is due to interactions between convective elements within the principal core. As the area fraction increases, these mutual interactions are enhanced, resulting in stronger rainfall beyond what is attributable to growing core area.

Finally, we note that the large majority of PFs have their rainiest pixels within their principal cores. Figure 2.7 shows the fraction of PFs for which the rainiest pixel (the pixel whose precipitation rate is MaxPr) is contained within the principal core of the PF. For the vast majority of PFs, the rainiest pixel is within the principal core. A notable class of exceptions are large systems with relatively weaker localization values, for which only about $\sim 50\%$ of PFs exhibit this property. Notably, for large and localized PFs, which is the configuration most strongly associated with ExPFs (Fig. 2.5), the fraction of PFs with rainiest pixel within the principal cluster is close to 100%, indicating that such extreme events tend to occur within the principal (largest) core within a PF.

2.3.3 Proposed morphology-entrainment-precipitation coupling pathway

We conclude this section by examining the vertical structure of PFs, and exploring the role of morphology in modulating the vertical structure of convection. In particular, we examine the mean reflectivity of the rainiest pixels for PFs of differing sizes and values of λ . Since reflectivity serves as a measure of the amount of cloud water present in the column, greater reflectivities at higher levels are indicative of stronger and deeper convection. For data volume reasons, we only consider PFs over the maritime continent region (highlighted in white in Fig. 2.4). The computed means are shown in Figure 2.8. We find that larger and more localized PFs have, on average, a greater mean reflectivity at a range of heights than

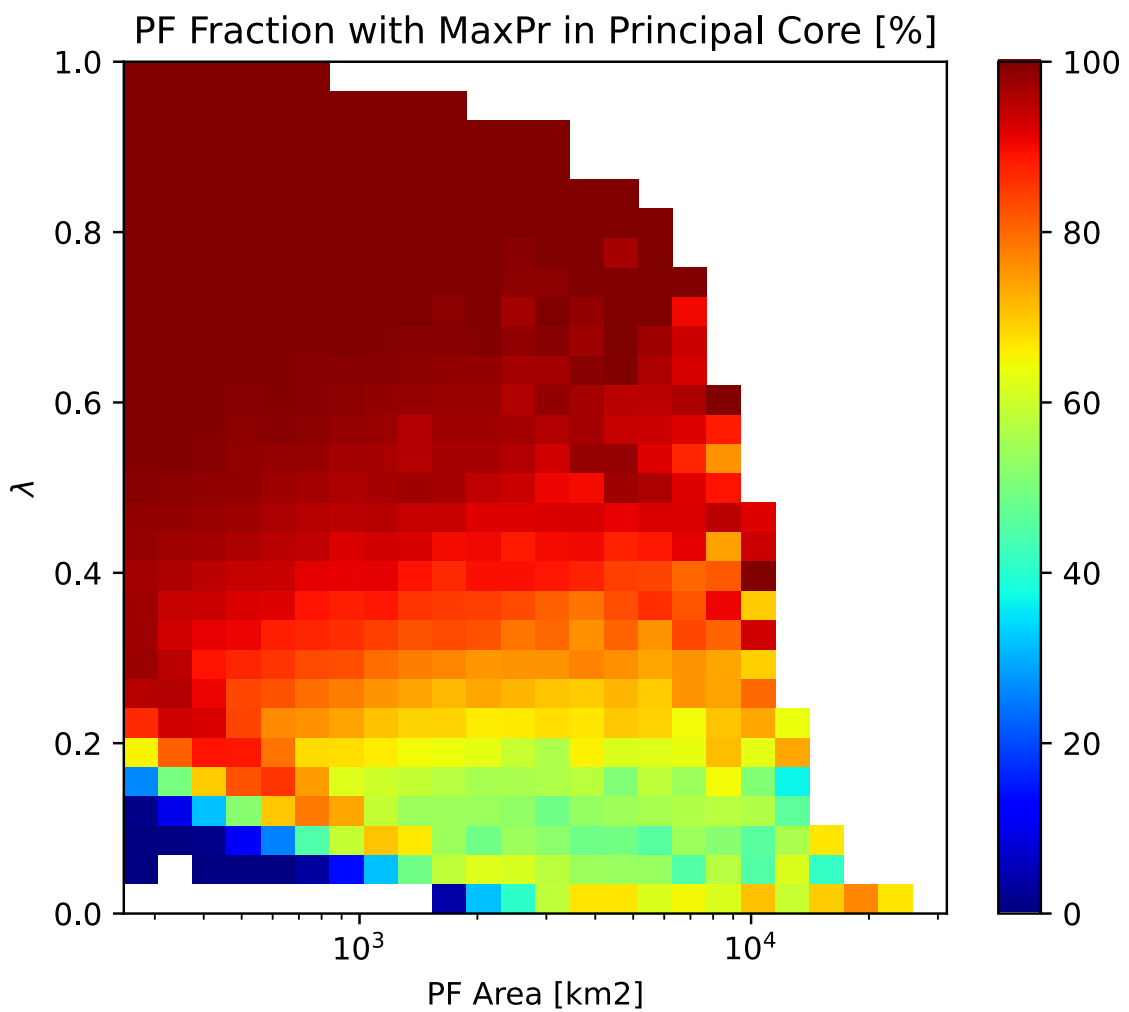


Figure 2.7: Fraction of PFs for which the rainiest pixel is contained within the principal core of the PF.

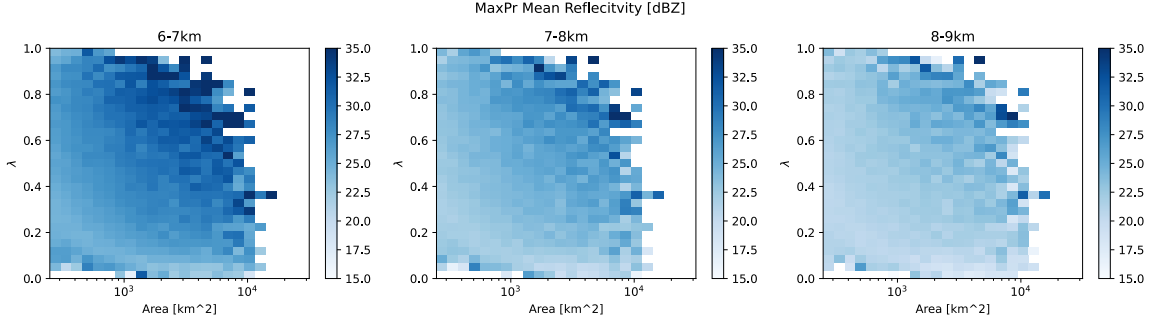


Figure 2.8: The average reflectivity (in dBZ) of a PF's rainiest pixels stratified by PF size and λ . Averages are taken over the indicated layers.

smaller and less localized PFs.

Based on Fig. 2.8, and the fact that most extreme rain events occur within the principal core of a PF, we speculate that the mutual interactions suggested by Fig. 2.6 are associated with the modulation of the near-cloud environment by convective entrainment and detrainment (see *de Rooy et al.* (2013) for a detailed review of entrainment and detrainment). Convective entrainment refers to the mixing of non-cloud (sub-saturated) air into a region of cloudy (saturated) air. Similarly, detrainment refers to the ejection of cloudy air into the non-cloud environment. The effect of entrainment is to dry cloudy updrafts, while the effect of detrainment is to moisten the near-cloud environment.

The proposed relationship between entrainment, morphology, and the vertical strength of convection is diagrammed in Fig. 2.9. In the proposed pathway, convection detrains saturated air into a non-saturated environment, thus moistening the local environment. Because of this moistening, the evaporative cooling and buoyancy reduction due to entrainment of subsaturated air into nearby convective elements is minimized, resulting in what may be termed “protected convection” *Brown and Zhang* (1997); *Holloway and Neelin* (2009). We speculate that in weakly or non-localized PFs (Fig. 2.9a), this moistening is relatively ineffective, so that the entrainment of dry environmental air is a major constraint on convection. However, in the case of localized PFs (Fig. 2.9b), we speculate that the increased localization of convection strengthens the moistening of the environmental air via detrainment. This results in stronger and deeper convection in more localized PFs, and offers an

explanation of why MaxPr is related to PF morphology.

2.4 Conclusions

In this study we have sought to better understand the connection between tropical precipitation extremes and the morphology of the precipitation features in which they are embedded. Using spaceborne radar observations from GPM with horizontal resolution of 5km, we identify tropical precipitation features (PFs) as contiguous rainy regions with rain rates exceeding 1 mm/hr (Fig. 2.1). Precipitation features with at least one rainfall value exceeding 60 mm/hr are classified as extreme-producing precipitation features (ExPFs; Fig. 2.2). We find that ExPFs are most prevalent over the climatological rainy regions, and make up a larger fraction of total continental PFs than oceanic PFs (Fig. 2.4).

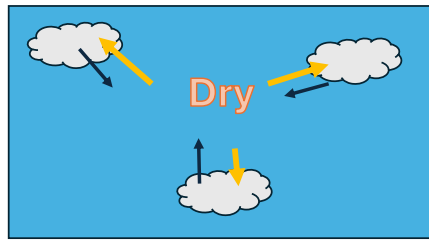
The morphology of each PF is characterized by its total area, which serves as a measure of feature-scale organization; and the localization of precipitation λ (Eq. 2.1), which provides a quantitative index of the clustering of the PF's rain production (Fig. 2.1). We found that compared to TyPFs, ExPFs are on average much larger (Fig. 2.4c,d) and more localized (Fig. 2.4e,f). This indicates that the maximum precipitation rate realized by a PF (MaxPr) is related to the spatial characteristic of the system.

We further explore the relationship between MaxPr and system morphology by examining how MaxPr depends on PF size and λ . We find that MaxPr is on average greatest for PFs that are larger and more localized (Fig. 2.5). This indicates that the morphology of a given PF modulates the maximum precipitation rate that the feature is capable of realizing. We further found that the dependence of MaxPr on PF size and λ are related, with MaxPr for larger PFs exhibiting a greater sensitivity to changes in λ than smaller PFs. We also observed that the precipitation localization scales faster than the areal fraction of the largest core within the PFs (Fig. 2.6). We interpret this as suggestive of the importance of mutual interactions between convection in the enhancement of precipitation with λ .

To examine the impacts of precipitation localization on the strength and structure of tropical deep convection, we examine how the mean reflectivity of the rainiest pixels over a range of vertical layers varies based on PF morphology. What we find is that for all PF sizes, increased λ is associated with an increased mean reflectivity within the rainiest core

Entrainment-Morphology Pathway

a) Weakly Localized



b) Strongly Localized

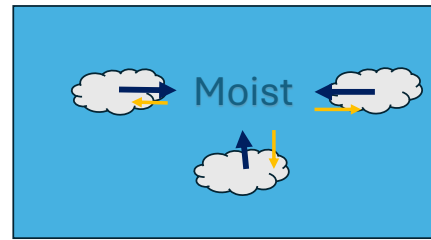


Figure 2.9: A schematic of the proposed coupling pathway between entrainment and morphology. In the case of (a) non-localized convection, the moistening of non-cloudy air by detrainment is less efficient because of the distance between convective elements. This causes the drying due to entrainment to have increased effectiveness in depleting buoyancy and hindering convection. In the case of (b) localized convection, the proximity of the convection allows detrainment to efficiently moisten the near-cloud environment of other convective elements, mitigating the buoyancy reduction associated with entrainment, and promoting stronger precipitation

for a range of heights (Fig. 2.3.3). We interpret this as suggestive that increased localization is associated with stronger convective transport of cloud water and hydrometeors. We propose that this is due to the effects of moisture detrainment, which allows cloudy air to moisten its nearby non-cloud environment and reduce the buoyancy loss due to entrainment of sub-saturated air into the cloud (Fig. 2.9). Though theoretical treatments of such interactions date back to the early days of the cumulus parametrization problem (*Fraser (1968); Arakawa and Schubert (1974)*), the question of how exactly to represent these interactions in models, and how those interactions depend on the model's scale, remains an active areas of research (*Tomassini et al., 2023*). This study therefore provides observational evidence on the importance of these interactions in producing high-impact precipitation extremes.

Chapter 3

SENSITIVITY OF SYSTEM MORPHOLOGY TO SUBGRID-MIXING STRENGTH IN IDEALIZED SIMULATIONS OF RADIATIVE-CONVECTIVE EQUILIBRIUM

3.1 *Introduction*

A full accounting of the impacts of mutual interactions between convective elements has been an outstanding question in tropical convection for several decades (*Fraser*, 1968; *Haman*, 1969; *Arakawa and Schubert*, 1974). Because of their distinct radiative and thermodynamic character compared to clear-air, clouds are a source of strong perturbations to the local background state. One primary way in which these perturbations are transferred to the large-scale environment is through turbulent mixing. In particular, at the interface between (saturated) cloudy air and (sub-saturated) environmental air, two processes are responsible for the mixing of cloudy and non-cloudy air: *entrainment*, whereby subsaturated air is mixed into the saturated updraft air; and *detrainment*, where cloudy air is released out into the environment (*de Rooy et al.*, 2013).

The ways in which entrainment couples clouds to their environments can depend on the convective regime being considered. For example, entrainment in stratocumulus decks is primarily considered a cloud-top process by which air above the cloud layer is entrained to lower levels (*Wood and Bretherton*, 2004, 2006). For deep convection, however, observational (*Brown and Zhang*, 1997; *Bretherton et al.*, 2004; *Rushley et al.*, 2018; *Wolding et al.*, 2020) and modeling (*Holloway and Neelin*, 2009) studies have highlighted the importance of entrainment in coupling large-scale environmental moisture profiles to the strength and structure of deep convection. In particular, the entrainment of dry mid-tropospheric air into deep convection was shown to reduce buoyancy via evaporative cooling. Furthermore, studies have also shown that the mixing of cloudy air into the environment (detrainment) moistens the near-cloud environment. This suggests that entrainment couples convection not only to its environment, but also to other proximate convective elements.

Entrainment has also been shown to exert some control over the organization of convection in idealized models. In particular, *Tompkins and Semie* (2017) performed a series of idealized numerical experiments to determine the role of entrainment in helping convection to aggregate to a stationary state. They found that stronger mixing rates (and thus stronger entrainment) are associated with a greater degree of convective organization. This finding suggests two non-exclusive possibilities: that increased sensitivity of convection to the local environment resulting from stronger entrainment results in more spatially localized convection; and, that increased moistening of the local environment from convective updrafts resulting from stronger detrainment helps promote future convection in the vicinity of existing convection.

However, the organization of convection does not always resemble the state of a single, large convective entity as is the case in self-aggregation in numerical models (see *Wing et al.* (2017) for a review). Rather, tropical convection is often organized into a population of discrete convective systems, as is seen in so-called “disaggregated” convection.

The purpose of this study is to determine what role subgrid mixing plays in modulating the vertical structure and horizontal morphology of convective systems in disaggregated convection. Using idealized simulations of radiative-convective equilibrium, this study will examine how different mixing strengths impact the morphology of precipitation features in disaggregated convection. We will perform three simulations of radiative-convective equilibrium, with the only change being in the subgrid mixing scheme’s eddy mixing coefficient, which controls the strength of subgrid mixing, and thus the mixing of moisture between cloudy updrafts and clear air. By varying the eddy mixing strength systematically, we can strengthen or weaken the entrainment experienced by convection. We will examine to what extent these changes impact the vertical structure of convection, the morphology of convective systems, and the maximum precipitation generated by each system.

The rest of this paper is organized as follows: Section 2 introduces the modeling framework we will use. It also details the experiments we performed. Section 3 examines the results of these modeling experiments. We examine the differences (as far as they exist) between precipitation features in each of the simulations analyzed. In Section 4 we offer concluding remarks.

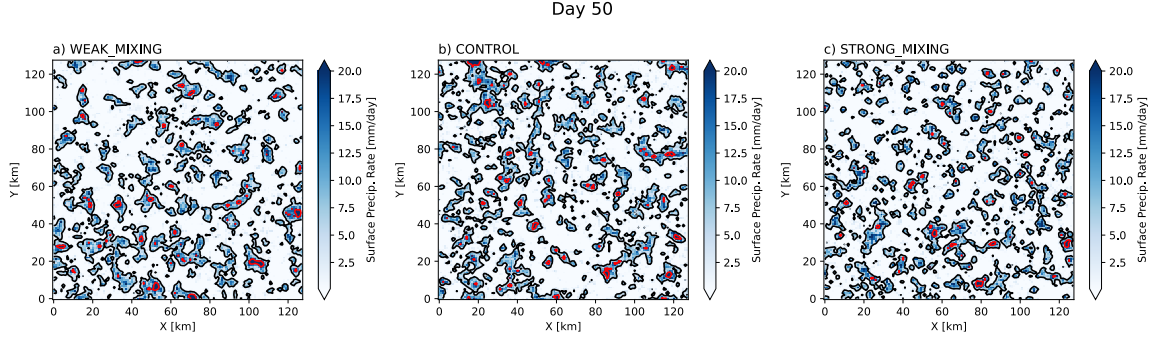


Figure 3.1: Snapshots of the precipitation field taken on Day 50 of the simulation. Boundaries of convective systems are shown in black. Boundaries of precipitation cores shown in red.

3.2 Model Simulations and Methodology

3.2.1 Model Setup

In order to investigate the role of free-tropospheric mixing modulating convection's coupling to spatial organization, we performed a series of idealized experiments with the System for Atmospheric Modeling (SAM; *Khairoutdinov and Randall (2003)*). The model experiments were run on a doubly periodic domain of area $128 \text{ km} \times 128 \text{ km}$. The model was integrated with a 1 km horizontal grid spacing, without a convective parameterization. The sea surface temperature was held fixed at 301 K. All models were run for 100 days. Two-dimensional fields are saved at daily frequency. With this configuration, no experiment exhibited an aggregated state (i.e., where convective elements clump into a single entity), as has been observed in models with larger domains (*Wing et al., 2017*).

We performed three modeling experiments in which the only parameter varied is the strength of the subgrid mixing scheme. The subgrid mixing scheme utilized by SAM is a turbulent kinetic energy (TKE) scheme, in which the model equation for a generic scalar field ϕ (such as humidity or temperature) is written as follows:

$$\frac{\partial \phi}{\partial t} + \frac{1}{\bar{\rho}} \nabla \cdot (\bar{\rho} \vec{V}_3 \phi) = \nabla \cdot (K \nabla \phi) \quad (3.1)$$

where \vec{V}_3 is the full three-dimensional velocity field, $\bar{\rho}$ is the base state (anelastic) density

profile, and K is the eddy diffusivity which varies in all three dimensions and in time. In TKE schemes, K in Eq. 3.1 is proportional to the local subgrid-turbulent kinetic energy:

$$K = C_s \times \sqrt{\text{TKE}} \times L \quad (3.2)$$

where L is a chosen eddy mixing length scale, TKE is the local turbulent kinetic energy, and C_s is the eddy diffusivity coefficient. Note that the turbulent Prandtl number is assumed to be unity in SAM, so the eddy diffusivity of scalars and eddy viscosity are identical.

The three model simulations differ from each other by the strength of subgrid mixing of both momentum and scalars. While one simulation uses the default setting for subgrid mixing, the others change the value of the eddy viscosity/diffusivity coefficient C_s in Equation (3.2), scaling it by a single factor for heights above 1.2 km.

These simulations are:

- A control run (CONTROL) in which C_s retains its default value of 0.1 for all heights;
- A weak mixing run (WEAK_MIXING) in which C_s is scaled down by a factor of 0.2 for heights above 1.2 km; and
- A strong mixing run (STRONG_MIXING) in which C_s is scaled up by a factor of 5 for heights above 1.2 km.

All simulations use the default value of C_s for heights below 400 m. A cosine ramp is used in the layer between 400 m and 1.2 km to link the default and modified values of C_s . It should be noted that the equal values of C_s in the sub-400 m layer does not imply equal values of K in this layer (Equation 3.2). Since K is proportional to TKE, different values of K should be expected between different experiments, as the value of TKE will differ between experiments.

We also distinguish *subgrid mixing*, which we do modify in our model experiments, and *entrainment*, which is a related but distinct component of model setups. Entrainment (*per se*) is a component of many mass-flux based formulations of convection representing the mixing of saturated (cloudy) and environmental profiles (Arakawa and Schubert, 1974;

(*Tiedtke*, 1989; *Yano*, 2014). Since our SAM simulations do not parameterize convection, the subgrid mixing (which serves to diffuse gradients in scalar or momentum fields) is always present, rather than only being enabled when representing moist convection as in the case of parameterized convection. As such, the subgrid mixing that occurs in our model might be said to *result* in entrainment, but is in fact a bit more general than that, as it occurs at all points in the model rather than only occurring in (parameterized) deep convective regimes, and diffuses not just humidity gradients, but gradients of other scalar and vector quantities as well.

3.2.2 Identifying Precipitation Features and Their Morphology

For each simulation, *precipitation features* are identified as contiguous groups of pixels with precipitation rates that exceeded the 75th percentile of non-zero precipitation rates for each experiment. We similarly define *precipitation cores* as contiguous regions with precipitation rates exceeding the 99th percentile of non-zero precipitation rates. These thresholds allow for the objective identification of coherent precipitation clusters and regions of intense precipitation, respectively. A snapshot of the precipitation field is shown in Fig. 3.1 for each experiment, with the outlines of precipitation features in white, and precipitation cores outlined in red. In this study, we only consider precipitation features with at least one core embedded within it. We will refer to the largest core within a system as the system’s “principal core” to facilitate discussion.

To describe the morphology of precipitation features present in our simulations, for each feature we computed morphological statistics. The first was simply the size of the feature, which serves as a direct quantification of the degree of feature-scale organization. We additionally computed the size of the principal core, which similarly served as a measure of how organized the principal core was. Finally, we computed for each precipitation feature was a parameter we will term the “localization” λ , which is defined as the fraction of feature precipitation produced by the principal core in the feature:

$$\lambda = \frac{P_{\text{principal core}}}{P_{\text{system}}} \quad (3.3)$$

By construction λ is dimensionless and bounded between 0 and 1.

3.3 Results

3.3.1 Vertical Mean-State Structure of Convection

The impacts of changing subgrid mixing between the model experiments are analyzed by computing vertical mean profiles. We first verify that the different experiments have differing mixing strengths; we do this by examining the mean vertical profile of eddy diffusivity (Eq. 3.2) averaged over the whole model domain (Fig. 3.2). We see that, as expected, STRONG_MIXING has much greater subgrid diffusivity values (and thus stronger mixing) than the CONTROL simulation; CONTROL in turn exhibits stronger mixing than WEAK_MIXING.

This change in eddy diffusivity has a marked effect on the mean turbulent kinetic energy (TKE) structure in each of the different simulations (Fig. 3.3). As would be expected from Eq. 3.1, stronger eddy diffusivity is associated with reduced TKE. Interestingly, the qualitative form of the TKE profile is similar between each of the simulations considered, with a top-heavy profile that peaks between 10 km and 12 km. This top-heavy structure exists both in the resolved and the subgrid components of TKE (not shown).

To investigate the vertical structure of simulated convection, we examine the mean profile of in-cloud* vertical velocity, where (Fig. 3.4). We find that STRONG_MIXING exhibits much stronger convection (faster vertical motions) in the lower troposphere (between 2 km and 6 km) than other simulations. This holds true also for higher levels between 6 km and 9km, where there is also a slight but clear separation between CONTROL and WEAK_MIXING. This indicates that enhanced mixing between the clouds and environment (accomplished by strengthening subgrid mixing) results in stronger convection.

A similar pattern as for in-cloud vertical velocity also holds for in-cloud vertical mass flux (Fig. 3.5). We observe that the STRONG_MIXING simulation exhibited overall stronger in-cloud vertical motions than either CONTROL or WEAK_MIXING. In particular, STRONG_MIXING had a pronounced excess in-cloud mass flux in the layer be-

*Here, “in-cloud” model voxels are defined as voxels either: with a combined cloud water and ice mixing ratio exceeding 10^{-5} kg/kg; or in a precipitating downdraft, with precipitation mixing ratio exceeding 10^{-4} kg/kg and negative vertical velocity

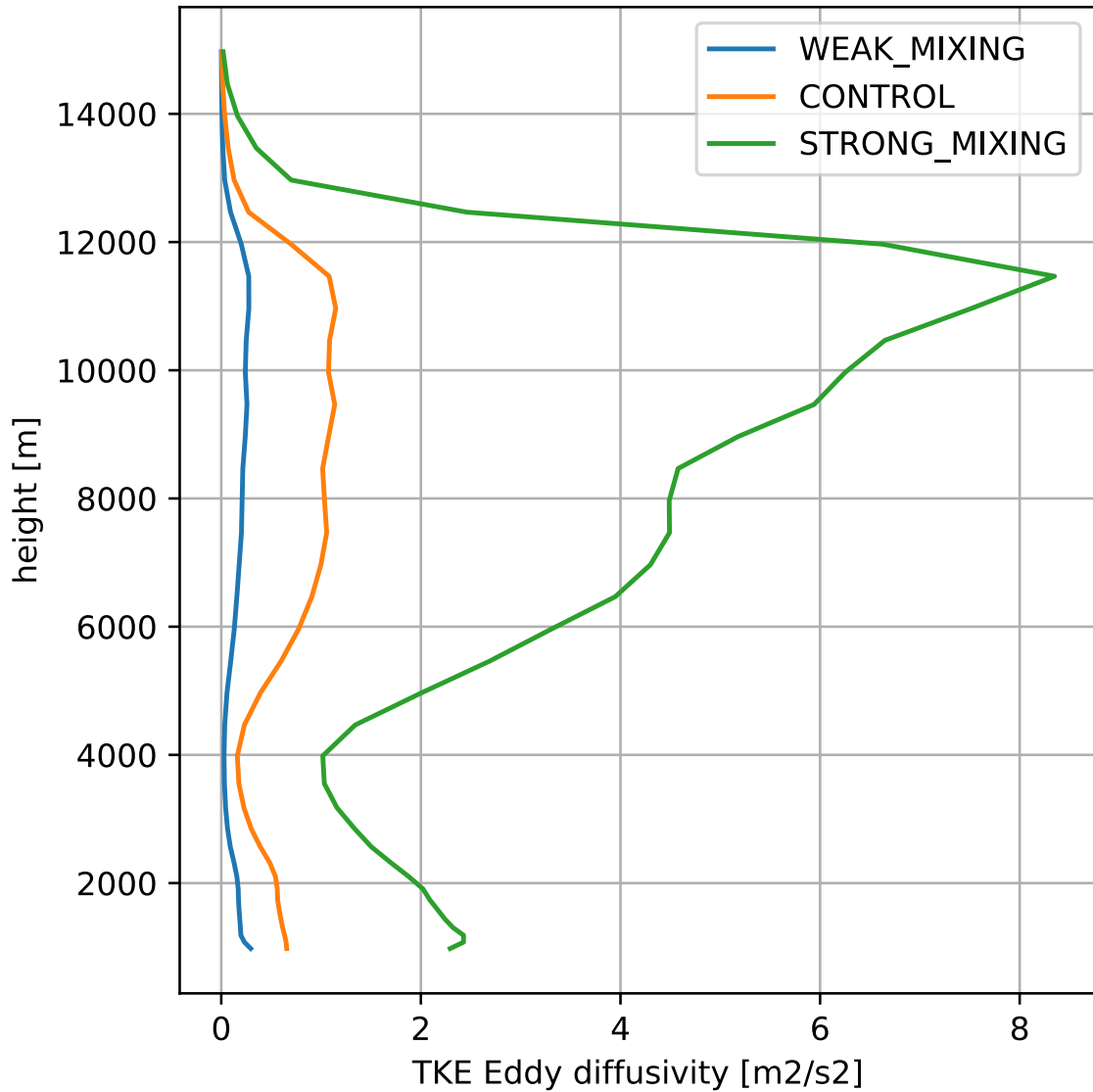


Figure 3.2: Mean vertical profiles of TKE eddy diffusivity (Eq. 3.2) for each of the three model simulations. Averages are taken over whole model domain over length of simulation.

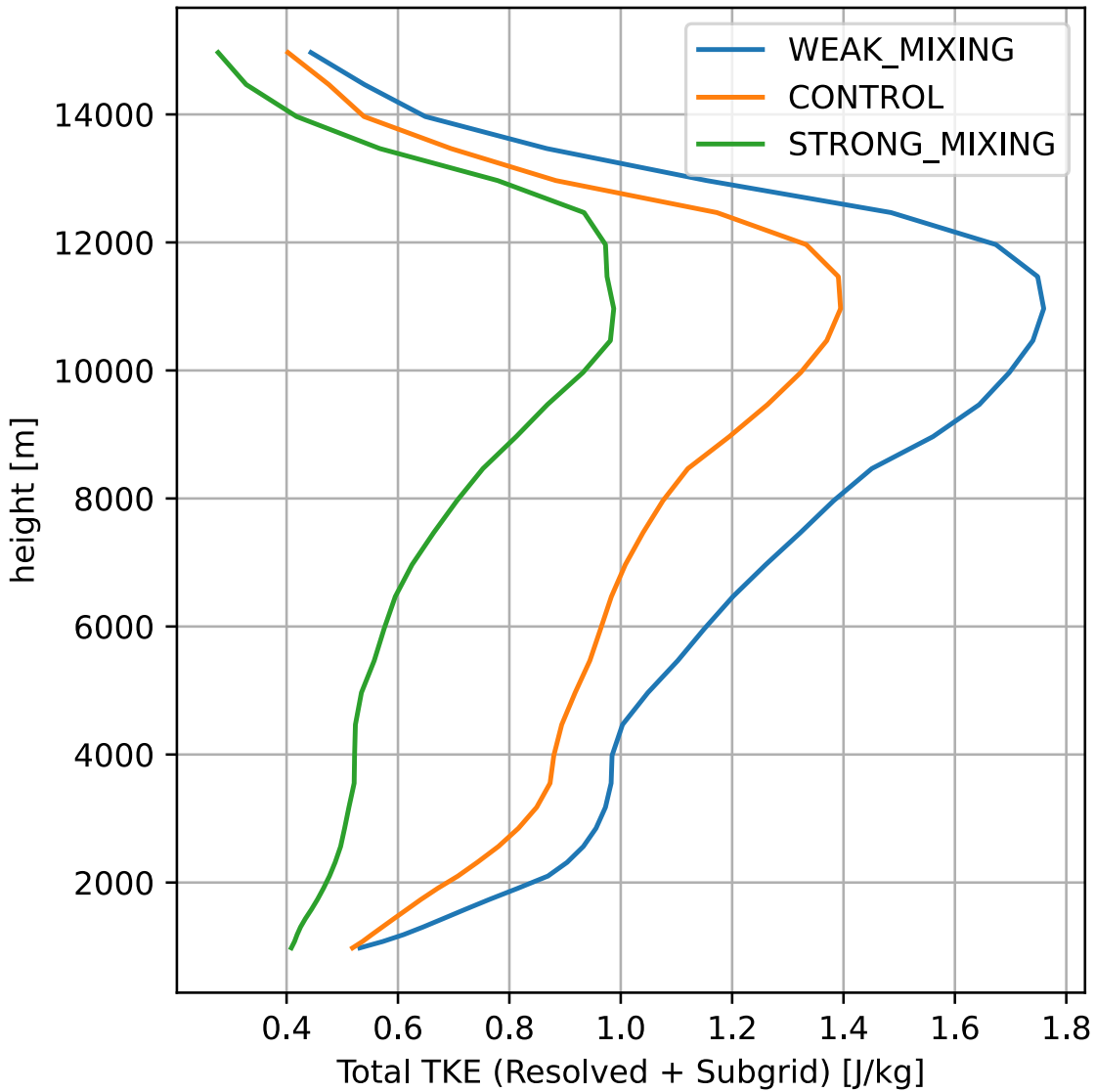


Figure 3.3: Vertical profiles of mean total turbulent kinetic energy (TKE) for each of the three simulation. Total TKE is the sum of both grid-scale (resolved) turbulence and subgrid-scale turbulence. Averages are taken over whole model domain over length of simulation.

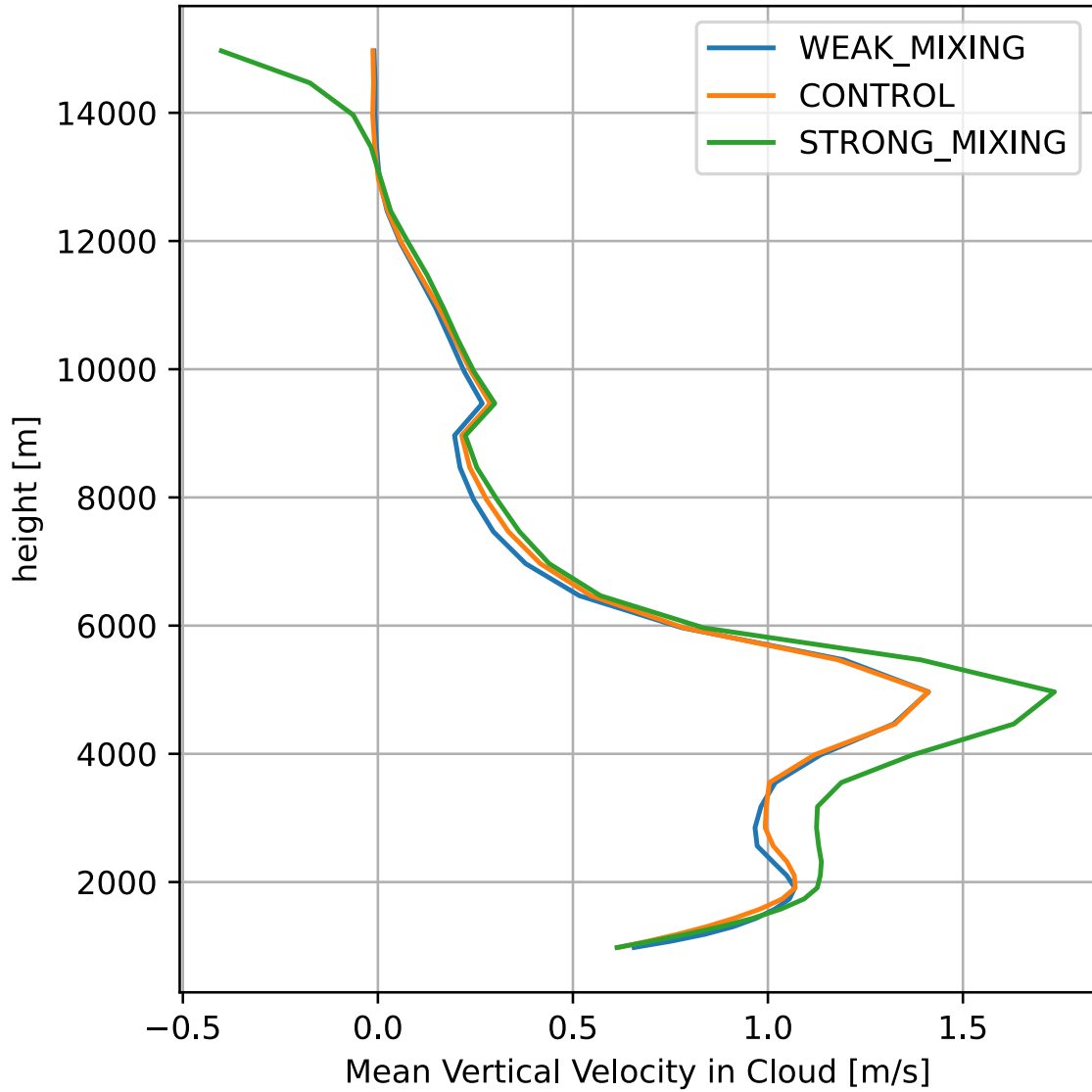


Figure 3.4: Vertical profiles of mean vertical velocity within clouds for each model experiment. Clouds boundaries are identified by a threshold of 10^{-5} kg/kg for cloud water mixing ratio. Averages are taken over whole model domain over length of simulation.

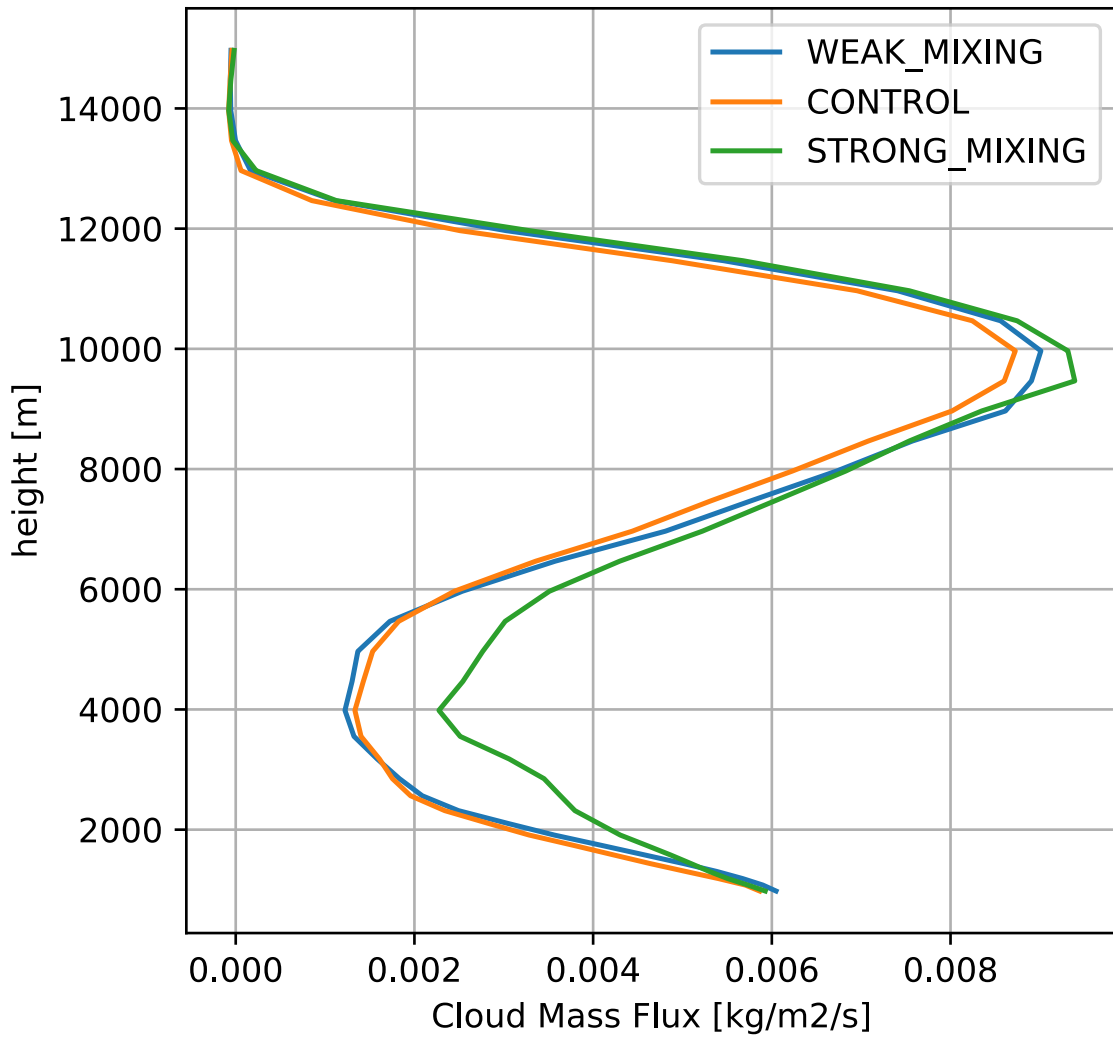


Figure 3.5: As in Figure 3.4, but for in-cloud vertical mass flux.

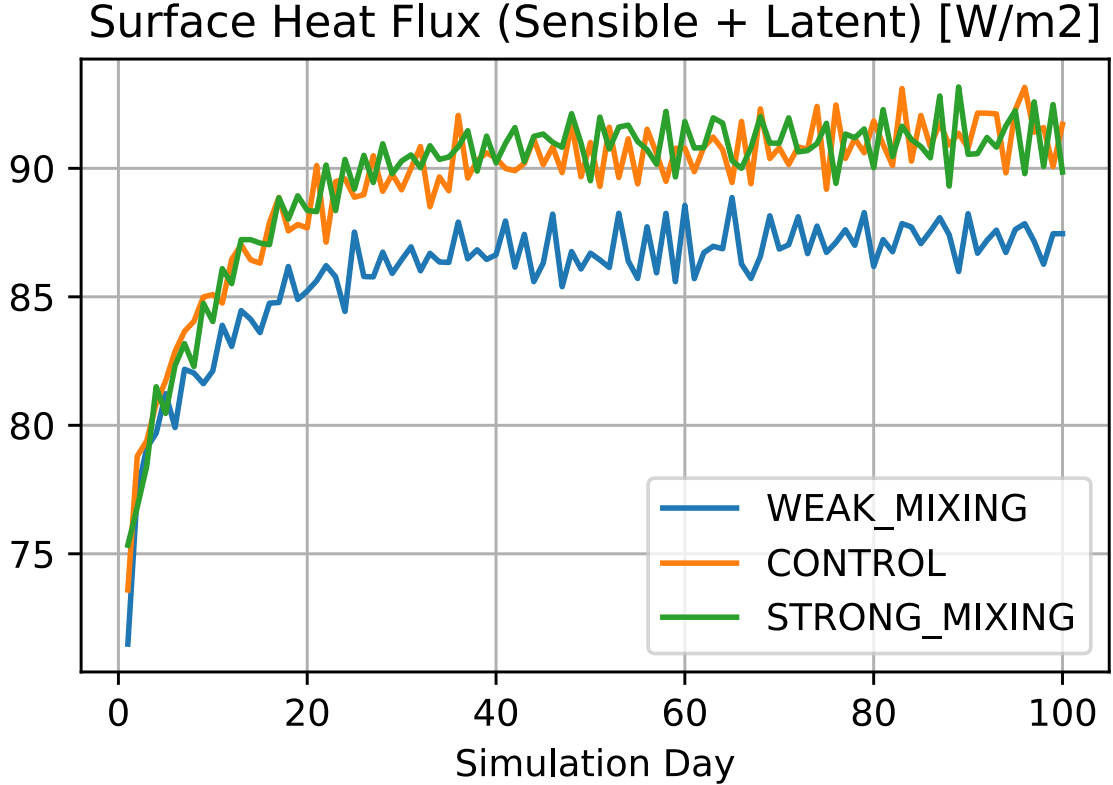


Figure 3.6: Timeseries of mean surface heat flux (sensible heat flux plus latent heat fluxes) for each of the three experiments considered.

tween 2 km to 6 km. This can be interpreted as a signature of more midlevel clouds in STRONG_MIXING. These clouds has been shown to play a role in modulating feedbacks between convective organization and circulations, suggesting that the overall circulation may differ between model simulations (*Sokol and Hartmann, 2022*).

Though we will not examine the circulation changes closely, we can obtain some insights into the energetic consequences of these differences in vertical velocity structures by comparing time series of mean surface fluxes (latent plus sensible) across the three simulations (Fig. 3.6). For all three experiments, we see that the surface fluxes begin at zero, and grow in amplitude until about day 40. We can take this as an indication of a developing convective ensemble that reaches some quasi-stationary state after 40 days. We note that

the amplitude of the surface fluxes differ substantially between the three simulations (Fig. 3.6). In particular, WEAK_MIXING has the weakest surface fluxes, while experiments with stronger mixing generate stronger surface fluxes. This suggests that simulations with stronger mixing (and thus stronger convection; Figs. 3.4 and 3.5) induce stronger surface fluxes. This is reminiscent of studies of self-aggregated convection in RCE, where interactions between surface fluxes and overturning circulations has been put forward as a primary driver or aggregation (*Bretherton et al.*, 2005; *Wing et al.*, 2017).

We further examine the impact of subgrid mixing on the mean-state vertical structure of convection by examining the vertical profiles of mean-state relative humidity (Fig. 3.7) and specific humidity (Fig. 3.8). We see that increasing the strength of subgrid mixing results in a drier atmosphere for almost all heights, both in terms of relative humidity and specific humidity. This can be understood as the consequence of the stronger convection present in STRONG_MIXING compared to CONTROL or WEAK_MIXING. In *Tompkins and Semie* (2017), more efficient mixing (larger mixing rates) from the TKE scheme is associated with an enhanced degree of convective aggregation and a drier troposphere. While we do not ever achieve an aggregated state in the model runs performed (probably due to the smallness of the domain considered), we can still see that more efficient mixing is associated with a drier atmosphere.

3.3.2 Changes to Precipitation Feature Population

Figure 3.9a shows the timeseries of the number of precipitation features identified for each experiment for each day. We can see that STRONG_MIXING has a notably larger number of systems present throughout the simulation than either CONTROL or WEAK_MIXING. Interestingly, there is no large difference between the number of features in CONTROL or WEAK_MIXING. Consistent with this, the features generated in STRONG_MIXING are also smaller on average than either CONTROL or WEAK_MIXING (Fig. 3.9b). This indicates that in STRONG_MIXING, precipitation features are generally both more numerous and smaller.

There are also notable differences between the three simulations in terms of the to-

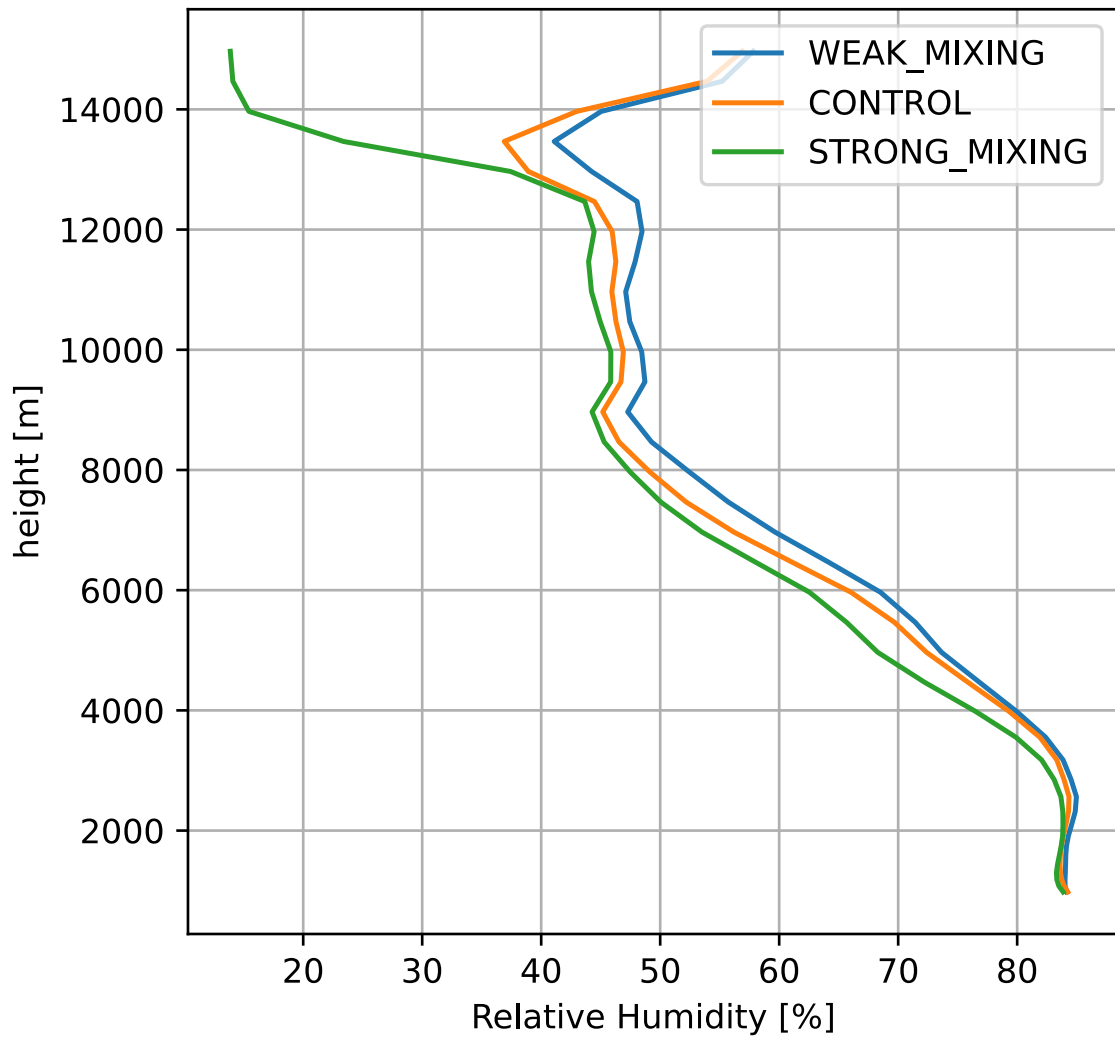


Figure 3.7: Mean vertical profiles of relative humidity (%) for each of the three model simulations. Averages are taken over whole model domain over length of simulation.

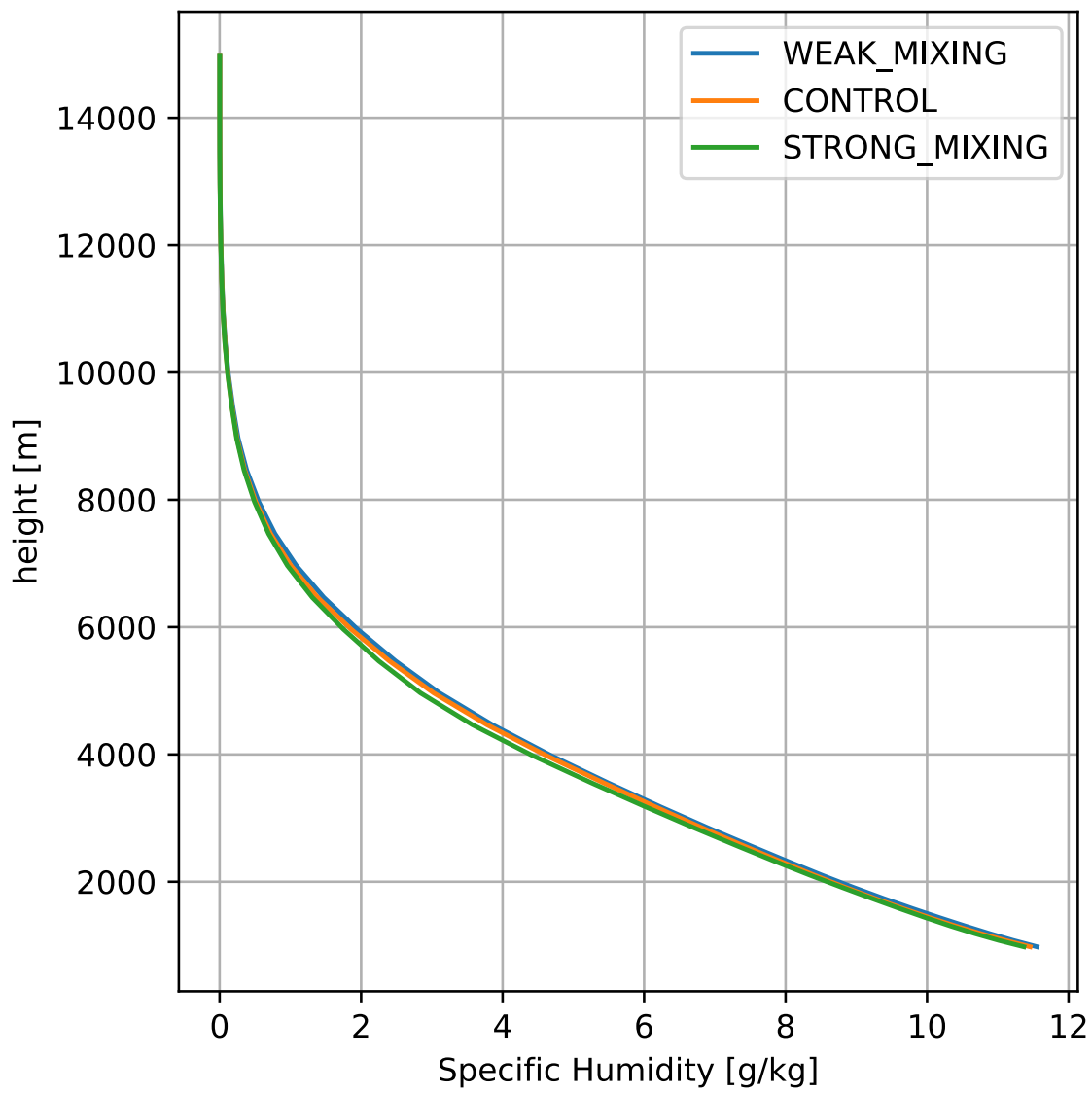


Figure 3.8: Mean vertical profiles of specific humidity (g/kg) for each of the three model simulations. Averages are taken over whole model domain over length of simulation.

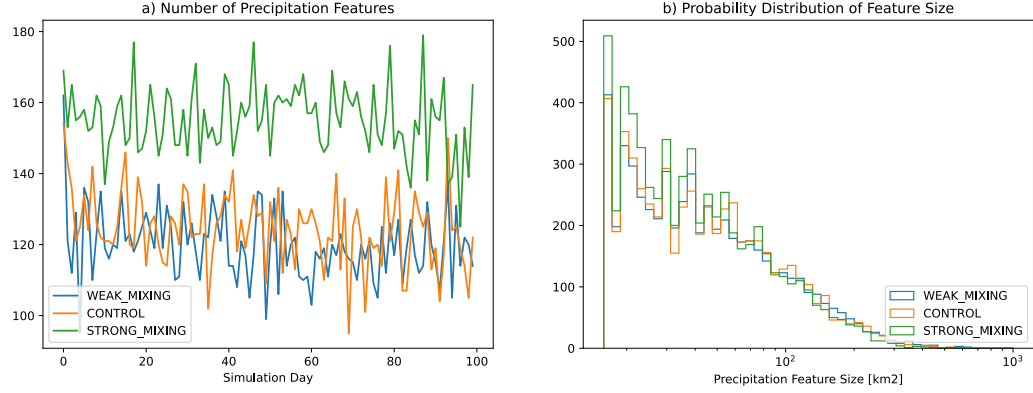


Figure 3.9: a) A timeseries of number of precipitation systems for each simulation. b) Normalized density of convective system area over the entire model run.

tal area fraction of the simulation domain that experiences precipitation (Fig. 3.10). In particular, STRONG_MIXING rain fractions are generally smaller than for CONTROL or WEAK_MIXING. This again indicates that precipitation features in STRONG_MIXING are smaller, and thus take up a smaller fraction of the entire model domain.

3.3.3 Mixing, Morphology, and Maximum Feature Precipitation

In this section we examine how the connection between a feature's morphology and its maximum precipitation rate (MaxPr) is affected by changes to the strength of subgrid mixing. Figure 3.11 shows the bin-averaged MaxPr value for precipitation features of given size and λ . We can see that for every simulation, MaxPr depends on both on λ and the size of the feature. All three simulations analyzed in Fig. 3.11 exhibit the greatest MaxPr values for features that are both large and localized. In comparing the three simulations, we observe that the MaxPr value for the smallest and least localized systems are generally greater for STRONG_MIXING than for CONTROL or WEAK_MIXING. However, the overall sensitivity of MaxPr to the morphology of the system appears to have been largely unchanged by the modulation in the mixing rates.

The influence of feature morphology of MaxPr is also apparent from Figure 3.12 , which shows the bin-mean values of feature MaxPr composited by the size of each feature's princi-

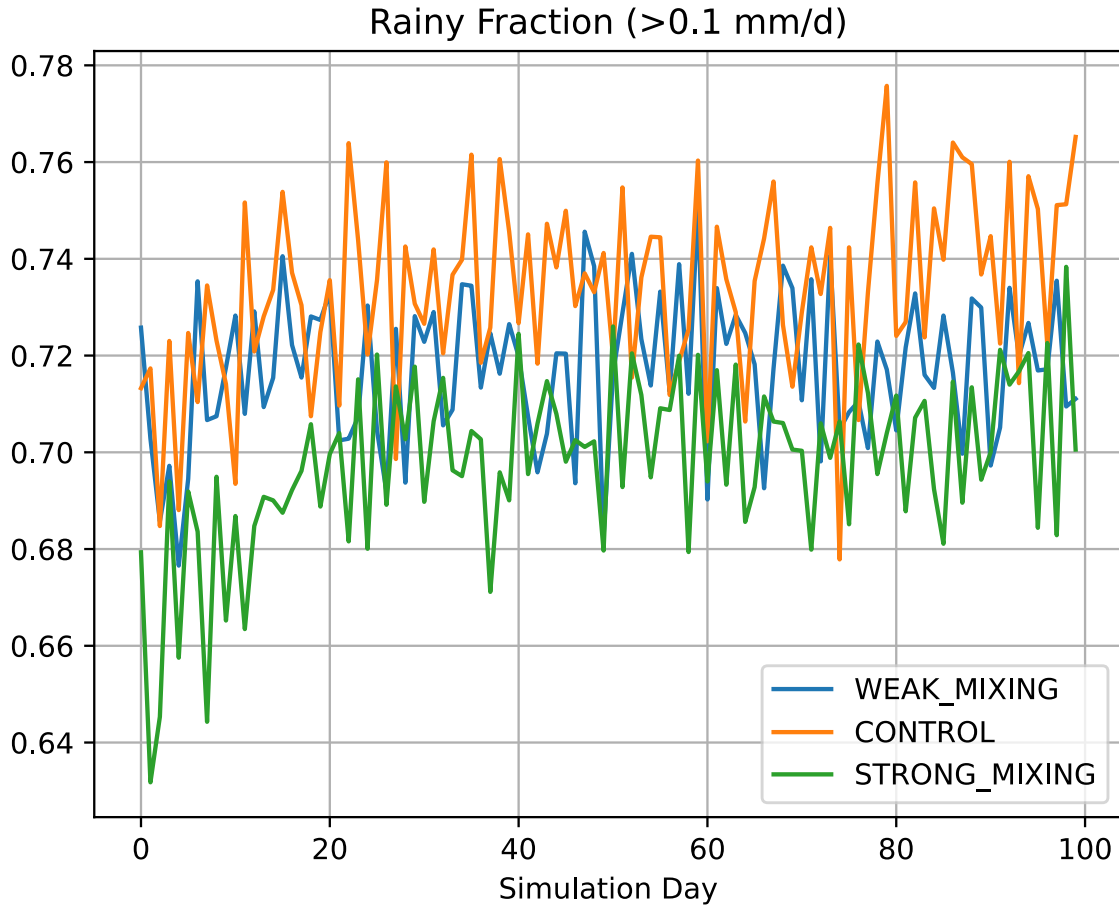


Figure 3.10: Time series of the fractional coverage of rainy pixels ($> 0.1 \text{ mm/d}$ rain rate) for each model experiment.

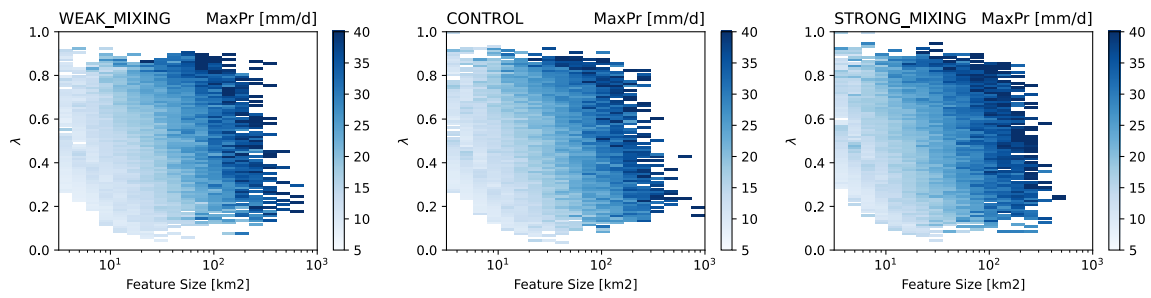


Figure 3.11: Bin-mean values of MaxPr, stratified by feature size (x-axis) and localization λ (Eq. 3.3; y-axis).

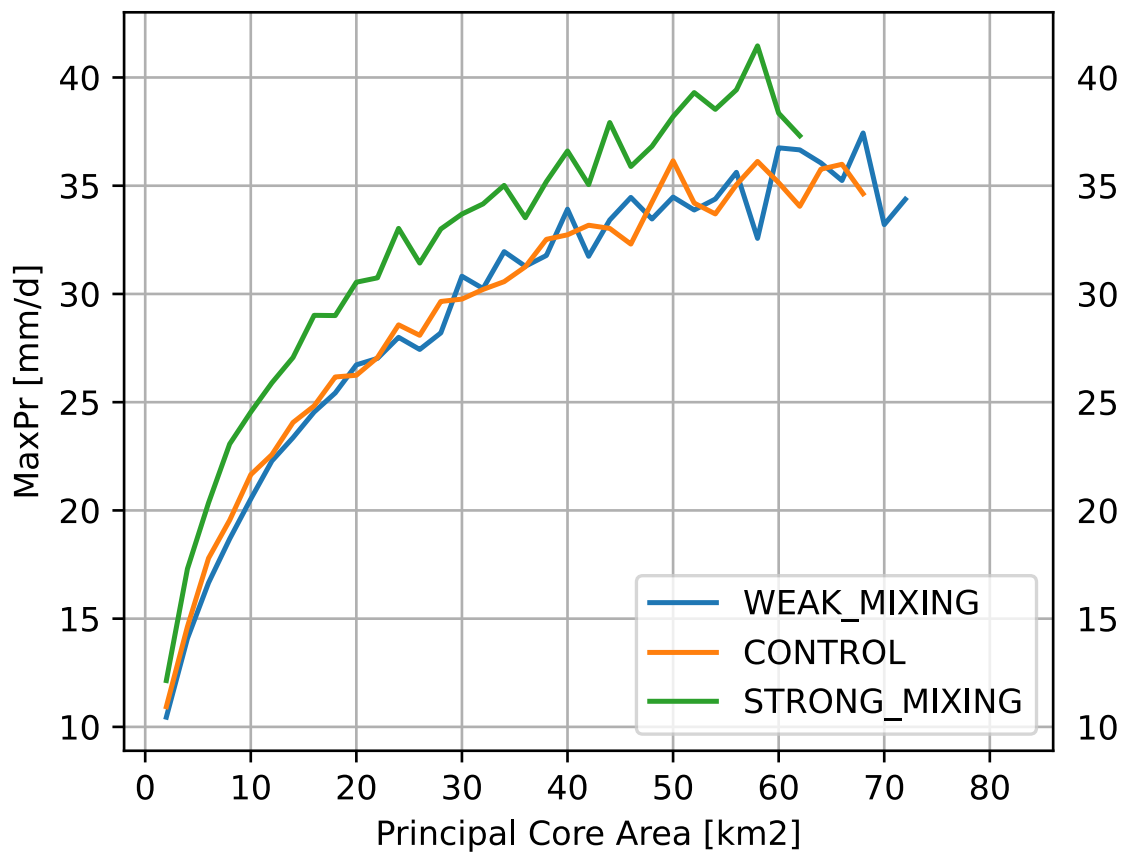


Figure 3.12: Feature MaxPr composited by the size of the feature's principal core. Only bins with at least 10 features are considered.

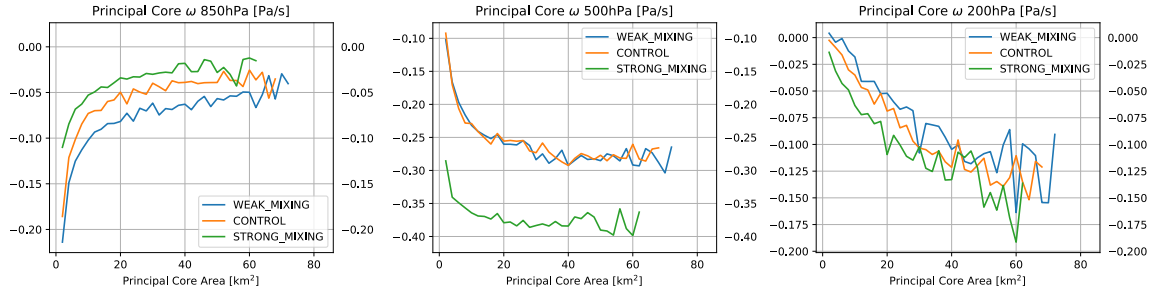


Figure 3.13: Bin-mean vertical velocity (in isobaric coordinates) within principal cores of indicated size. Vertical velocities reported at a) 850 hPa; b) 500 hPa; and c) 200 hPa.

pal core. We can observe that in all three experiments, larger principal cores are associated with greater MaxPr. We further note that in the STRONG_MIXING experiment, the scaling of MaxPr with the area of the principal core is stronger than in CONTROL or WEAK_MIXING. The difference between CONTROL and WEAK_MIXING in Fig. 3.12 is rather negligible, however.

We can further probe the interactions between morphology and MaxPr by examining the mean vertical structure of the principal cores of precipitation features. Figure 3.13 shows the mean vertical velocities (in isobaric coordinates) of principal cores, composited by the size of the core. We see that for 850 hPa (Fig. 3.13a), there is stronger ascent (more negative values) in WEAK_MIXING and CONTROL than STRONG_MIXING. We further see that there is a slight but clear weakening in vertical velocity at this level with increasing principal core size, indicating that larger principal cores experience weaker vertical velocity at 850 hPa than smaller principal cores. Turning to 500 hPa isobar (Fig. 3.13b), we see much stronger ascent within principal cores for STRONG_MIXING than either WEAK_MIXING or CONTROL. However, there is not much change in vertical velocity at this level with changing principal core sizes. Finally, considering the 200 hPa isobar (Fig. 3.13b), we see a very clear relationship between core size and vertical velocity at this level; in particular, larger principal cores experience much stronger vertical velocity than smaller cores at 200 hPa. Interestingly, for all three heights considered, the scaling between principal core size and MaxPr is largely comparable, suggesting that the different model experiments exhibited

similar dependence between principal core size and vertical motion, but differing absolute values.

From Figure 3.13 we can identify that core size is a stronger modulator of upper-level vertical motions (200 hPa level; Fig. 3.13c) than lower levels. This is consistent with the idea that larger cores would be more protected from buoyancy reduction due to mixing of dry air into updrafts, which would in turn favor vertical motions deep into the troposphere.

3.4 Conclusion

In this study we have sought to better understand the role that subgrid mixing plays in coupling the morphology of a given precipitation feature to its precipitation production. Using a set of three idealized RCE experiments with disaggregated convection and differing subgrid mixing strengths (STRONG_MIXING, WEAK_MIXING, and CONTROL) we define precipitation features in each model integration as contiguous groups of pixels with precipitation rates exceeding the 75th percentile of precipitation rate for that model. We further define precipitation cores as contiguous groups of pixels within features exceeding the 90th percentile of precipitation rate (Fig. 3.1).

We find that the different mixing strengths do impact the overall number and mean size of precipitation features generated (Fig. 3.9). In particular, we find that the STRONG_MIXING experiment results in a larger number of smaller systems than either the CONTROL or the WEAK_MIXING experiments. We further note that the different mixing strengths are also associated with robust and clear differences in the mean vertical structure of the atmosphere. We see that the modulation in the magnitude of the eddy mixing coefficient results in a greater amount of subgrid mixing (eddy diffusivity; Fig. 3.2). We see that stronger mixing is associated with both a greater amount of cloud mass flux (Fig. 3.5) as well as a drier atmospheric profile (Figs. 3.7 and 3.8). Overall, these results suggest that stronger mixing results in stronger convection (as quantified by mass flux) and more spatially constrained features.

We additionally examined the relationship between feature morphology, quantified by the feature size and its localization λ (Eq. 3.3), and the maximum precipitation value generated by the feature (MaxPr). We observe that MaxPr does depend on both feature

size and λ for all model experiments, with greatest MaxPr values associated with large and localized features (Fig. 3.11). The dependence between MaxPr and the size of the principal core indicates that the largest principal cores generate a greater MaxPr values than smaller principal cores. This suggests that more spatially localized feature morphologies serve to promote extreme values of MaxPr.

Finally, we examined the vertical structure of principal cores of differing sizes to investigate the coupling between core size and MaxPr. We found that core size is a major determinant of 200 hPa-level vertical motions, but is not as important for 500 hPa or 850 hPa vertical motions. This suggests that core size affects the maximum depth achievable by convection for all models. Notably, the dependence (slope) between core size and MaxPr seems largely similar between all experiments considered, suggesting that the different mixing rates did not modulate the overall sensitivity of precipitation production to feature morphology.

Chapter 4

MULTISCALE CONVECTIVE CIRCULATIONS AND SCALE INTERACTIONS IN A GLOBAL STORM-RESOLVING MODEL

4.1 Introduction

A fundamental difficulty in accurately representing convection and its interaction with large-scale circulations in numerical models is the smallness of the scales at which moist deep convection occurs. Contemporary global climate models (GCMs) have typical resolutions on the order of $\sim 100\text{km}$, which is too coarse to explicitly represent deep convective systems. Because of this, convection must be parameterized within global climate models. Such so-called convective (or cumulus) parameterizations attempt to represent the aggregate dynamics and thermodynamics of ensembles of convective clouds, rather than individual constituents of deep convective systems (*Arakawa and Schubert, 1974; Randall et al., 2003; Arakawa, 2004*).

However, both observational and numerical studies have shown that processes that occur at scales smaller than a GCM grid are known to be critical to the formation, maintenance, and organization of convective systems. A particular example of such processes is the organization of deep convection into mesoscale convective systems (*Houze, 2004, 2018*). With characteristic spatial dimensions on the order of $\sim 100\text{km}$ (*Feng et al., 2021*), MCSs are organized convective systems comprised of several relatively narrow deep cumulonimbus cores connected by a spatially extensive stratiform anvil cloud. The deep convective elements within an MCS contributes positive heating at all levels through the depth of the troposphere. The stratiform component, by contrast, exhibits a dipole heating structure, with evaporation of falling hydrometeors contributing a negative heating below the melting level, and condensational heating contributing positive heating above the melting level (*Houze, 1982; Houze Jr., 1989; Schumacher et al., 2004*)

Thus, the vertical heating profile of MCSs exhibit a “top-heaviness” (*Liu et al., 2021*).

Representing this property of MCSs in numerical models has been shown to improve the simulation of large-scale circulations of the tropics (*Hartmann et al.*, 1984). Furthermore, recent studies have shown that the top-heaviness of vertical motions affects the efficiency of moist static energetic export by the associated overturning circulation (*Inoue et al.*, 2021). In addition to the combined heating profile resulting from their superposition, the positive-definite heating of deep convection and the dipole heating of stratiform clouds induce distinct gravity wave responses to the environmental stratification, which propagate at different speeds due to the dispersive nature of internal gravity waves (*Bretherton and Smolarkiewicz*, 1989; *Mapes*, 1998) and may have implications for the role convection plays in making its local environment either more or less favorable for subsequent convection (*Mapes*, 1993, 2000). From all this it therefore follows that the interactions between circulations that occur at scales smaller than an individual convective system may have impacts on the circulations that occur at larger scales, and thus may be crucial to the coupling between convection and large-scale circulations.

It is also worth noting that the small-scale convective circulations modulate the properties of clouds, which in turn affects the role of radiation on large-scale convectively coupled circulations. A clear example of this is the role of longwave heating by spatially expansive stratiform anvils in the maintenance of the MJO (*Kim et al.*, 2015). These anvils are borne out of the outflow of deep convective clouds, and are thus strongly coupled to convection that is unresolvable at the scale of a GCM grid. Additionally, model studies of convective self-aggregation in idealized radiative-convective equilibrium (see, e.g., *Wing et al.* (2017) for a review) have shown the importance of longwave heating due to water vapor in the development and maintenance of a state of aggregated deep convection (*Wing and Emanuel*, 2014; *Emanuel et al.*, 2014). Thus, the way that small-scale convection modulates the larger-scale atmospheric state is influenced by both the dynamical circulations of such systems, as well as the role those circulations play in affecting clouds.

A major recent development for our ability to numerically represent these interactions is the proliferation of global models with “storm-resolving” resolutions (grid size roughly smaller than 5-km; also termed “cloud-resolving” and “cloud-permitting” resolutions in the literature). At these resolutions, the model can explicitly represent individual storm systems

without the need for a convective parametrization. These models, therefore, offer a novel and powerful tool for deepening our understanding of the multiscale couplings between deep convective systems and large-scale circulations.

In this study we will utilize output from a global storm-resolving simulation that was done as a part of the second phase of the DYnamics of the Atmospheric general circulation Modeled On Non-hydrostatic Domains (DYAMOND2) project (*Stevens et al.*, 2019). We will examine tropical convection over the ocean in this model, and characterize the convective circulations that exist on both large and small scales. In Section 2 we describe the model used in the present study, as well as the observational data used. In Section 3 we describe the framework by which we will separate and describe the large-scale and small-scale convective circulations. In Section 4 we will describe the nature of the large-scale circulations, their evolutions, and the relationship between the structure of the large-scale vertical motions and mean cloud properties. In Section 5 we document and discuss the small-scale circulations. In Section 6 we consider our results in light of the broader question of scale interactions in tropical convection, and offer support to the importance of on the upscale impacts of small-scale circulations. Conclusions and final remarks are stated in Section 7.

4.2 Model Setup and Datasets

4.2.1 Model Setup

The model used for this study is the Global System for Atmospheric Modelling, or gSAM (*Khairoutdinov et al.*, 2022), a global extension with realistic topography of the widely-used System for Atmospheric Modeling (*Khairoutdinov and Randall*, 2003). The dynamical core of gSAM is formulated using the anelastic approximation with a global constant reference density profile. The model run analyzed in this study was part of the DYAMOND2 project. DYAMOND2, an extension of the DYAMOND project (*Stevens et al.*, 2019), is a model intercomparison of GSRMs. As part of this intercomparison, our gSAM run was initialized on January 20, 2020, and run freely (without nudging towards observations) for 40 days, with prescribed sea surface temperature (SST), ending on March 1, 2020. The model grid has a horizontal spacing of 4.34 km at the equator. The default single-moment microphysics

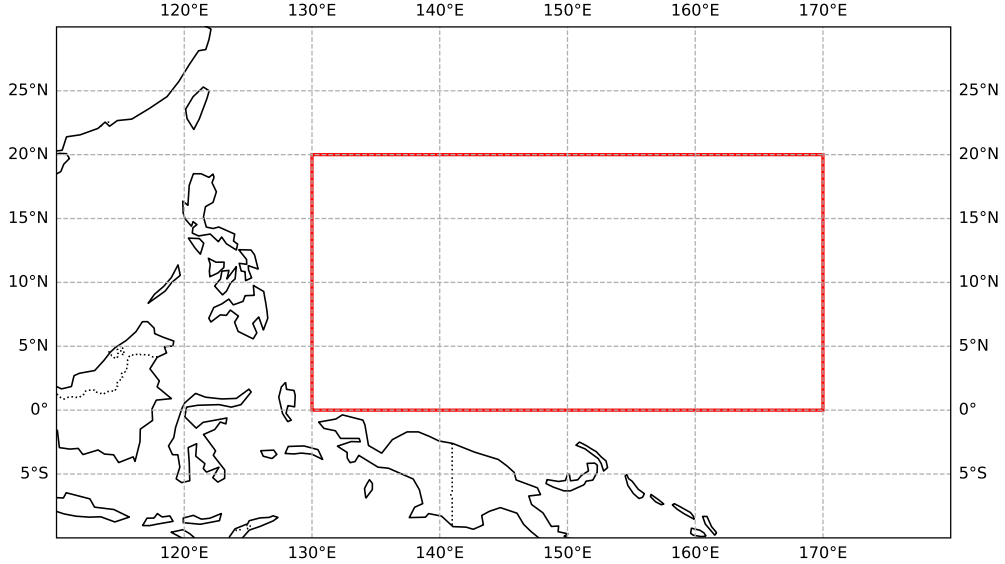


Figure 4.1: The red box above indicates the boundaries of our study domain.

scheme in SAM is used. Further details of the run are given in *Khairoutdinov et al. (2022)*. The three-dimensional model fields are output every 3 hours. We only use model data from the latter 30 days (February 1 to March 1, 2020) to allow for model spin-up. We select as our study domain a region in the northwestern tropical Pacific, between 0N and 20N, and 130E to 170E (Fig. 4.1). An oceanic domain is chosen to avoid the effects of orography.

4.2.2 Observational and Reanalysis Data

To provide an observational comparison to our model output, we utilize a combination of gridded observational products. All observational data are taken from Feb 1, 2020 to Feb 28, 2020, over the same latitude and longitude domain as gSAM (Fig. 4.1).

Vertical mass flux profiles, as well as estimated of column water vapor, are obtained from the ERA5 reanalysis (*Hersbach et al., 2020*). The ERA5 data are provided at global 0.25° horizontal resolution. Observational estimates of hourly precipitation are obtained

from Version 1 of the Climate Prediction Center Morphing Technique (CMORPH; *Joyce et al.* (2004)). CMORPH provides hourly global precipitation estimates at 0.25° horizontal resolution. Observational estimates of longwave and shortwave cloud radiative effects are derived from the CERES SYN1DEG satellite observational product (*Rutan et al.*, 2015). These products provide hourly estimates of both clear-sky and all-sky radiative fluxes at top-of-atmosphere. The data are provided at 1° and hourly resolutions.

All observational data are subsampled to 3-hourly resolution and coarsened to $2^\circ \times 2^\circ$ spatial resolution.

4.3 Methods

4.3.1 Scale separation: large-scale and small-scale motions

Since we are interested in understanding both the “small-scale” and “large-scale motions” in our GSRM, we must impose a scale separation to define these scales of motion. We set this scale separation at $2^\circ \times 2^\circ$ (50 gSAM pixels a side) for the purposes of the present study. We can thus decompose any given atmospheric field φ as

$$\varphi(x, y, z, t) = \underbrace{\bar{\varphi}(z, t)}_{\text{large-scale}} + \underbrace{\varphi'(x, y, z, t)}_{\text{small-scale}} \quad (4.1)$$

where $\bar{\varphi}$ denotes the horizontal average of φ over a given $2^\circ \times 2^\circ$ domain, and is termed the “large-scale” profile of φ over the domain. In a similar way, φ' denotes the deviation from this horizontal mean at each coordinate, as is termed the “small-scale” structure of φ over the domain. To avoid confusion between the rectilinear scale-separation of $2^\circ \times 2^\circ$ and the grid resolution of gSAM (4km), we shall refer to these segments as “domains” and “pixels”, respectively.

The choice of $2^\circ \times 2^\circ$ is arbitrary in some sense; however, this scale corresponds to the partition between meso- α and meso- β scales, as defined by *Orlanski* (1975). Physically, this separation is meant to partition coherent circulation responses (e.g. CCEWs) from the smaller-scale circulations more proximately driven by convection. From a modeling perspective, this scale separation is meant to represent the separation between circulations on the scale of a contemporary GCM grid, and circulations that have historically been

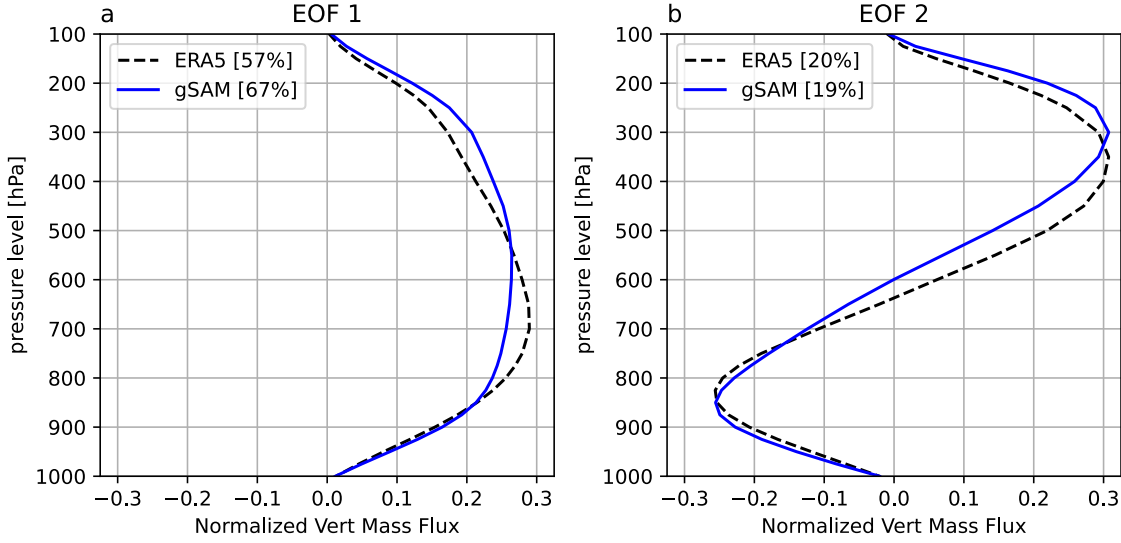


Figure 4.2: First (a) and second (b) empirical orthogonal functions (EOFs) of large-scale vertical mass flux for gSAM (solid blue) and ERA5 (dashed black). The explained variance ratio for each mode is indicated in brackets.

parameterized.

4.3.2 Characterizing large-scale vertical motions

To quantitatively characterize large-scale vertical motions, we compute the leading empirical orthogonal functions (EOFs) of large-scale vertical mass flux, following previous studies (*Back and Bretherton, 2009; Inoue et al., 2020; Chien and Kim, 2023*). The two leading EOFs for both gSAM and ERA5 are shown in Figure 4.2. Together the first two EOFs explain 86% and 77% of the total variance for gSAM and ERA5, respectively. The first EOF exhibits upward vertical motion through the depth of the troposphere, while the second EOF exhibits ascent above ~ 5 km and subsidence below. These structures are consistent with the ones found by previous studies (e.g., *Back and Bretherton (2009); Inoue et al. (2020); Chien and Kim (2023)*). We term the first EOF the “convective mode” and the second EOF the “stratiform mode”. As the sign of an EOF is arbitrary, the second EOF was taken as having the opposite sign to our stratiform mode in *Back et al. (2017)*, with low-level ascent

and high-level subsidence, and so was termed the “shallow mode”. However, this study’s emphasis on the role of the elevated overturning circulations associated with latent heat release in stratiform clouds motivates us to adopt a convective/stratiform nomenclature.

Since the explained variance by the first two EOFs is so high (Fig. 4.2), we approximately decompose the large-scale vertical mass flux \bar{M} as the a linear combination of the two orthogonal profiles:

$$\bar{M}(z, t) \approx \alpha_{conv}(t)M_{conv}(z) + \alpha_{strat}(t)M_{strat}(z) \quad (4.2)$$

where M_{conv} and M_{strat} are the first and second EOFs, respectively, and α_{conv} and α_{strat} are the first and second principal components (PCs). Note that the values α_{conv} and α_{strat} are large-scale variables, defined for each time step for each 2° domain.

We define normalized PCs a_{conv} and a_{strat} as

$$a_{conv} = \frac{\alpha_{conv}}{\sigma_{conv}} \quad (4.3)$$

$$a_{strat} = \frac{\alpha_{strat}}{\sigma_{strat}} \quad (4.4)$$

$$(4.5)$$

where σ_{conv} and σ_{strat} is the standard deviation of all α_{conv} and α_{strat} , respectively. Thus the ordered pair (a_{conv}, a_{strat}) serves as a leading-order description of the strength and vertical structure of the large-scale convective circulation.

In Section 4 we will utilize a phase plane spanned by a_{conv} and a_{strat} . In this case, each large-scale domain can be assigned a point in the a_{conv} - a_{strat} plane, given by (a_{conv}, a_{strat}) . We can thus compute for each grid cell an associated amplitude R_{cs} given by

$$R_{cs}^2 = a_{conv}^2 + a_{strat}^2, \quad (4.6)$$

and associated angle θ_{cs} given by

$$\tan(\theta_{cs}) = \frac{a_{strat}}{a_{conv}}. \quad (4.7)$$

To group similar large-scale vertical motions, we partition the a_{strat} - a_{conv} plane into eight *Phases*. The phases are numbered with Phase 1 corresponding to a regime of large-scale subsidence ($a_{conv} < 0, a_{strat} \approx 0$); Phase 3 corresponding to a regime of lower-level

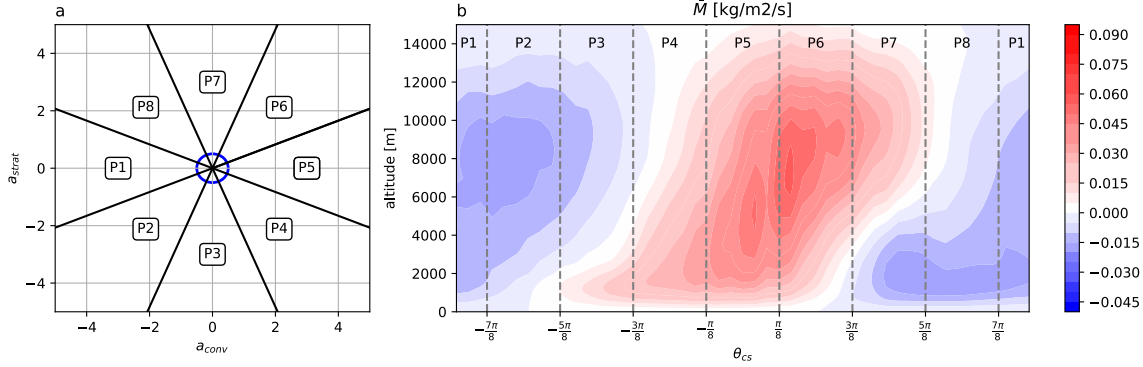


Figure 4.3: a) Diagram showing the partitioning of the a_{strat} - a_{conv} plane into eight phases. The circle in the center shows the boundary of Phase 0, which comprises bins with $R_{cs} < 0.5$; b) the composite large-scale mass flux profile (\bar{M} ; Eq. 4.2) binned by θ_{cs} . The boundaries of each phase are indicated.

ascent and upper-level subsidence ($a_{conv} \approx 0, a_{strat} < 0$); Phase 5 corresponding to a regime of ascent through the depth of the tropopause ($a_{conv} > 0, a_{strat} \approx 0$); and Phase 7 corresponding to a regime of upper-level ascent and lower-level descent ($a_{strat} > 0, a_{conv} \approx 0$); the even-numbered phases represent transitional stages between these regimes. Figure 4.3a shows how the a_{strat} - a_{conv} plane is divided into these phases. The circle in the center of 4.3a shows the bounds of Phase 0, which is the designation for a_{conv} - a_{strat} bins with $R_{cs} < 0.5$. Since we are primarily interested in regimes of strong vertical motions, we will typically neglect this phase.

The dynamical significance of each phase can be seen clearly in Figure 4.3b, where large-scale vertical mass flux profiles (\bar{M} , Equation 4.2) are binned and composited by θ_{cs} (profiles with $R_{cs} < 0.5$ are neglected). We can see that different values of θ_{cs} correspond to different degrees of top- or bottom-heaviness of the vertical velocity profile. Differences in the shape of the large-scale ascent profile have been shown to have ramifications for the large-scale energetics of convection, in particular in connection to the so-called gross moist stability of the atmosphere (*Inoue et al., 2021; Back and Bretherton, 2009; Bernardez and Back, 2024; Raymond et al., 2009*). We note that what we are calling θ_{cs} is conceptually similar, but not exactly equivalent, to the “top-heaviness angle” of *Bernardez and Back*

(2024). The amplitude of \bar{M} can be seen to vary with θ_{cs} , with the strongest values of $|\bar{M}|$ in the convective Phases 5–6.

4.3.3 Small-scale circulations and moisture space

We additionally seek a representation for the small-scale vertical motions that occur within a large-scale domain. To isolate and describe the vertical motions at this scale, we utilize the *moisture space* framework used in previous works (*Bretherton et al.*, 2005; *Schulz and Stevens*, 2018; *Sokol and Hartmann*, 2022). To construct the moisture space, we compute for each gSAM pixel (x, y) its saturation fraction, given by

$$\text{SF} = \frac{\langle q \rangle}{\langle q^* \rangle} \quad (4.8)$$

where q is the specific humidity, q^* is the saturation specific humidity, and brackets indicate mass-weighted integration through the depth of the column. Each column is then assigned a normalized rank $\eta \in [0, 1]$, with the column with the lowest SF taken to have $\eta = 0$, and the column with the greatest SF taken to have $\eta = 1$. The vertical coordinate remains untransformed. Thus every point (x, y, z) in our original three-dimensional domain corresponds to a new point (η, z) in our two-dimensional moisture space representation.

A mass circulation in the moisture space can thus be defined via a streamfunction ψ given by

$$\psi(\eta, z, t) = \int_0^\eta M'(\eta', z, t) d\eta' \quad (4.9)$$

where $M'(\eta, z, t) = M(\eta, z, t) - \bar{M}(z, t)$ is the small-scale mass flux (i.e., anomalous motions relative to the domain mean). It is clear from the definition that $\partial_\eta \psi = M'(\eta, z, t)$. By mass continuity, it can be shown that $\partial_z \psi$ is the cumulative convergence of columns with rank less than the argument η . Thus contours of ψ correspond to the exchange of mass between columns with differing SF values. We stress that the circulation in the moisture space should be distinguished from the three-dimensional circulation occurring in the Cartesian coordinates. Rather than capturing the motions in physical space, this circulation in moisture space is a two-dimensional representation of the net exchange of mass between relatively drier parts of the grid cell and relatively moist parts.

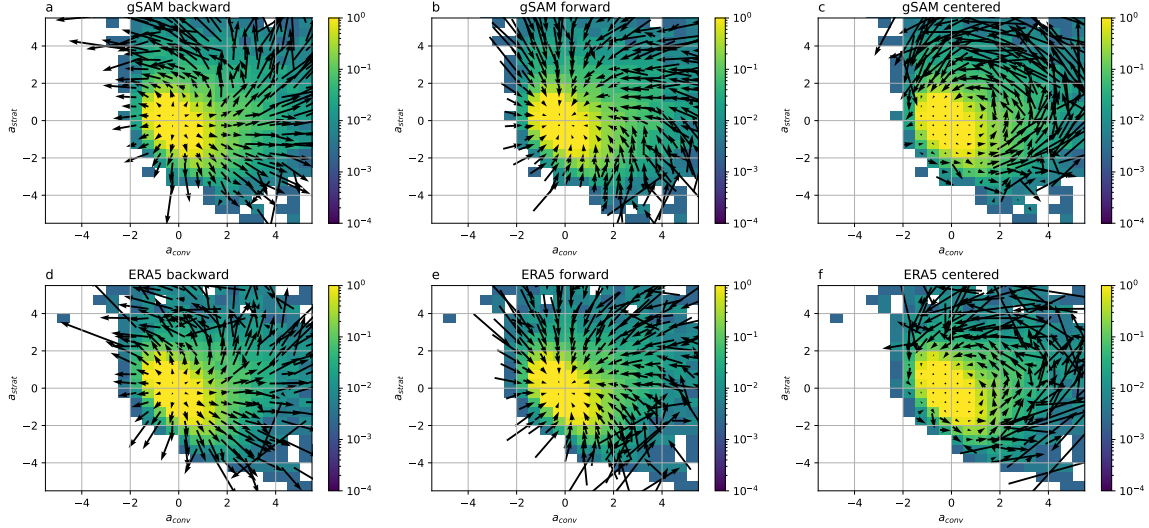


Figure 4.4: (Shading) Joint histogram of gSAM (top row) and ERA5 (bottom row) in the a_{conv} - a_{strat} plane. Bin-mean tendencies a_{strat} and a_{conv} are shown as arrows. Backward differences (a,d) show the evolution over the preceding 3 hours, with arrow heads located at bin center; forward differences (b,e) show the evolution over the subsequent 3 hours, with arrow tails located at bin center; and centered differences (c,f) represent the mean evolution over a 6 hour centered period, with arrow midpoints located at bin center.

4.4 Large-Scale Circulations and Mean Cloud Properties

4.4.1 Mean Eulerian evolution of large-scale circulations

We first consider the evolution of the large-scale vertical motions in gSAM. At each time step the large-scale vertical mass flux profile $\bar{M}(z, t)$ for each $2^\circ \times 2^\circ$ domain can be represented by a point (a_{conv}, a_{strat}) in a phase plane, with (x, y) coordinates corresponding to projection of \bar{M} onto the first and second EOFs of vertical mass flux (Sec. 3b). The evolution of these grid-scale motions can thus be represented as the vector change between time steps. Figure 4.4 shows the average change in a_{conv} and a_{strat} computed between observations at time $t - 3$ hours and t (hereafter the backward difference), between time t and $t + 3$ hours (hereafter the forward difference), and time $t - 3$ hours and $t + 3$ hours (hereafter the centered difference). We stress that these difference schemes capture the local (Eulerian) evolution of the flow. Figure 4.4 displays these differences separately as quiver plots, with

the joint histogram of observations shown in coloring (same between all panels).

We see that the backward differences (Fig 4.4a) exhibit a radially outward component, indicating that the strongest large-scale convective circulations (large R_{cs}) arise from relatively rapid strengthening of the circulation over a given location. This outward component is seemingly greater for bins farther from the origin, further indicating that the strongest grid-scale circulations also undergo the most rapid local evolution. Similarly, the mean forward differences (Fig. 4.4b) exhibit a radially inward component in the mean evolution, again supporting the claim that the strongest large-scale convective circulations relatively short-lived deviations from the mean vertical motions present at a given location. Both the forward and backward differences exhibit a slight counter-clockwise rotational component. The centered difference over a 6 hour period (Fig. 4.4c) exhibits a weaker radial component than the forward and backward differences, indicating that the radial components of Figures 4.4a and 4.4b are approximately equal and opposite. The mean centered difference has a much more dominant counter-clockwise rotational component. By its definition (Eq. 4.7), the angular coordinate of the a_{conv} - a_{strat} plane corresponds to the shape of the large-scale vertical motion profile. This suggests that on timescales on the order of 6 hours, the average (centered) evolution of the strongest large-scale vertical motions is largely comprised of modifications in the relative top- or bottom-heaviness of the vertical mass flux profile. A similar relationship between forward, backward, and centered differences was found in reanalysis by *Wolding et al.* (2020).

To compare the mean evolution in gSAM to observations, a similar analysis is performed on ERA5 vertical mass flux profiles (Figure 4.4e-f). We can see a remarkable similarity in the mean evolution fields between ERA5 and gSAM for all 3 difference schemes, which gives us confidence in gSAM's ability to accurately represent the evolution of large-scale ascending motions on sub-daily time scales.

4.4.2 Transition frequencies between phases

The counter-clockwise evolution evident in Figure 4.4 can also be captured by computing the frequency with which a $2^\circ \times 2^\circ$ domain evolves from being in one Phase to another as

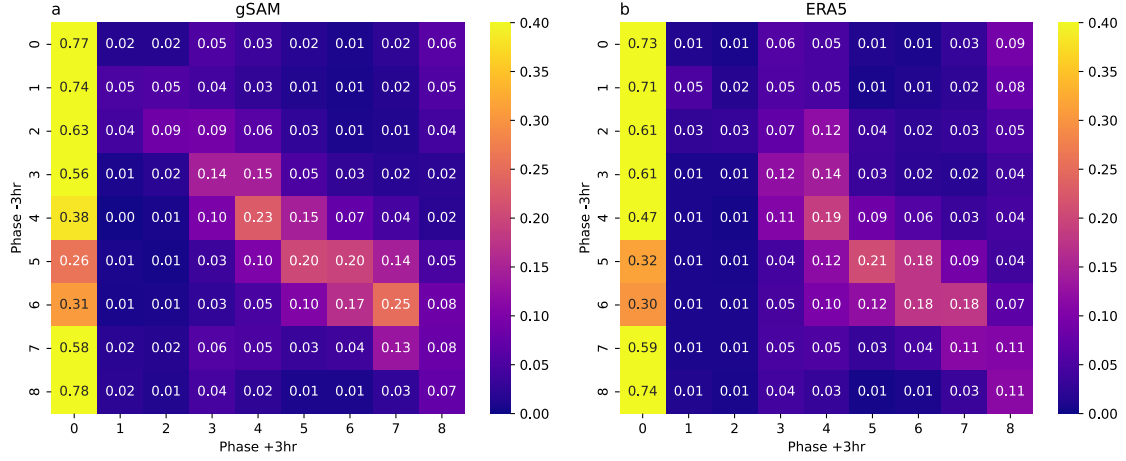


Figure 4.5: Transition frequencies over a 6-hour centered period for (a) gSAM and (b) ERA5. The shown frequencies indicate the conditional probability that a large-scale domain that is in the indicated initial phase at $t-3\text{hr}$ will transition to a given final phase at $t+3\text{hr}$.

defined in Figure 4.3. These transition frequencies are computed for gSAM (Figure 4.5a) and ERA5 (Figure 4.5b). The frequencies are computed as the fraction of $2^\circ \times 2^\circ$ domains that are in the indicated initial Phase at $t-3$ hours that then transition to the indicated Phase at $t+3$ hours. By construction, then, each row of frequencies shown in Figure 4.5 sums to unity.

We see that for all initial Phases, the most common transition is to Phase 0 (i.e., weak large-scale vertical motion), indicating a propensity for circulations to weaken over a 6-hour period. Only in Phases 4, 5, and 6 does the likelihood of a transition to Phase 0 fall below 50%. However, for all Phases, there is a notable local maximum in probabilities centered along the main diagonal. The maximized probabilities in Fig. 4.5 correspond to the fraction of large-scale domains that persist in the same phase (diagonal entries), advance to the subsequent phase (first upper off-diagonal), or regress to the preceding phase (first lower off-diagonal). In Section 4.6, we will relate these differing transitions to the large- and small-scale circulations that occur beforehand.

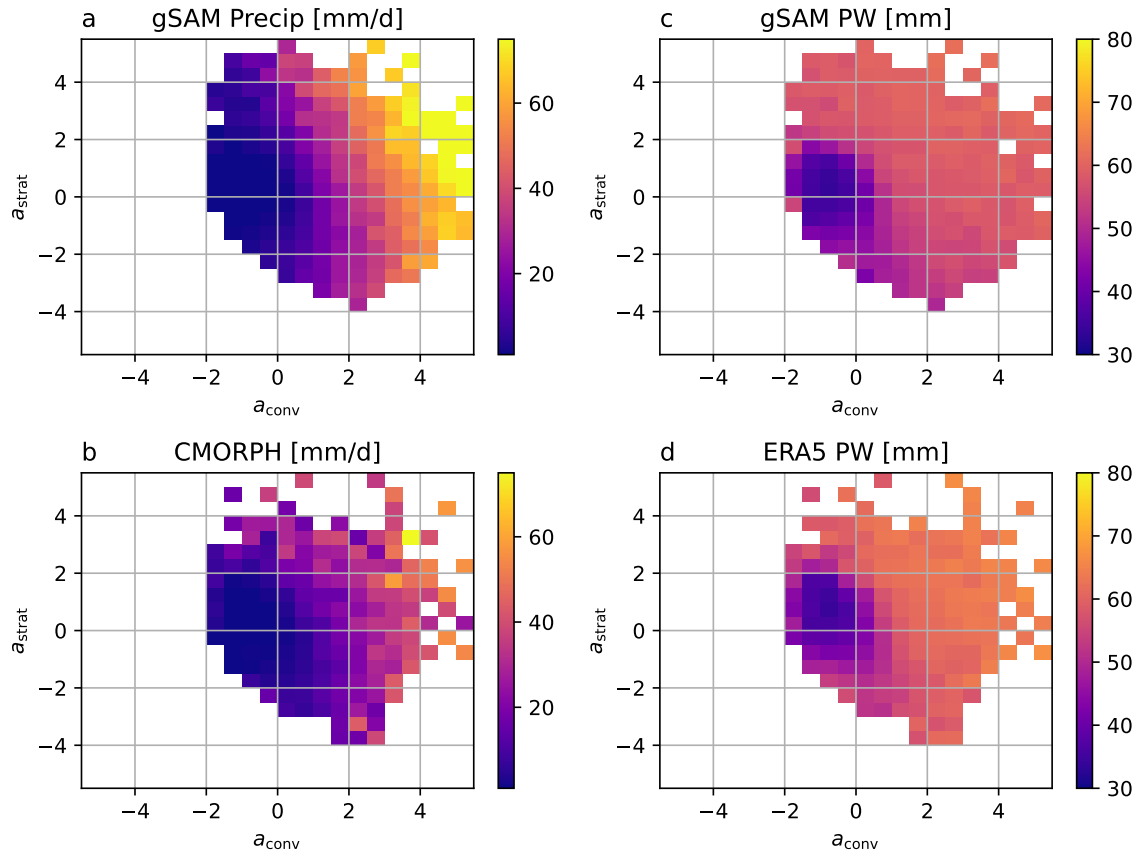


Figure 4.6: (a-b) Bin-average of large-scale precipitation derived from (a) gSAM and (b) CMORPH observational dataset; (c-d) bin-average of large-scale precipitable water (PW) from (c) gSAM and (d) ERA5 Reanalysis.

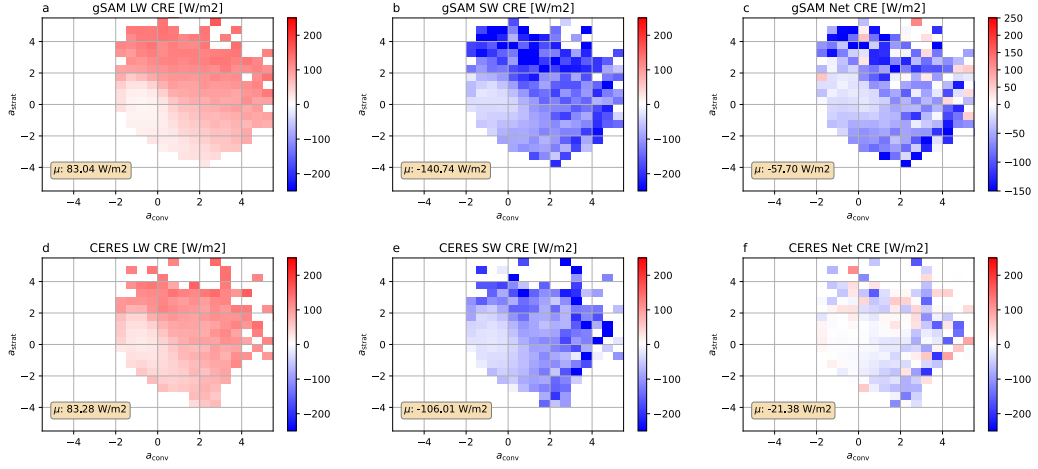


Figure 4.7: As in Fig. 4.6, but with cloud radiative effects (CRE) binned by a_{conv} and a_{strat} . Top row: Bin-composite values of (a) longwave CRE; (b) shortwave CRE; and (c) net CRE in gSAM. Bottom row: CERES values of (d) longwave CRE; (e) shortwave CRE; and (f) net CRE. Averages over all bins displayed

4.4.3 Large-scale circulations and mean cloud properties

The counterclockwise mean evolutions indicated in Figure 4.4c for gSAM and Figure 4.4f for ERA5 can be interpreted as a manifestation of the so-called “prototypical convective life cycle” (PCLC). The PCLC is an idealization of the lifecycle of organized convective systems as deviations from an assumed quiescent background state. The PCLC is comprised of a shallow/congestus convective stage, followed by a deep convective stage, and a subsequent stratiform stage. This pattern has been used to describe the evolution of a range of tropical convective disturbances, from large-scale equatorial waves to individual mesoscale convective systems (Mapes *et al.*, 2006; Khouider and Majda, 2008; Kiladis *et al.*, 2009). We can invoke the PCLC to describe the mean counterclockwise evolution evident in Figure 4.4c as an initially bottom-heavy circulation dominated by shallow/congestus convection ($a_{strat} < 0$, $a_{conv} \approx 0$); which develops into a deep convective regime ($a_{conv} > 0$, $a_{strat} \approx 0$); which eventually becomes more top-heavy as stratiform clouds develop ($a_{strat} > 0$, $a_{conv} \approx 0$); and which eventually decays into weak subsidence ($a_{conv} < 0$, $a_{strat} \approx 0$).

To validate this proposed association of the structure of large-scale vertical motions

and cloud properties, we examine the composites of large-scale cloud, precipitation, and radiative quantities over bins in the a_{conv} - a_{strat} plane. Figure 4.6 shows the dependence of large-scale precipitation rates and precipitable water (PW) on a_{conv} and a_{strat} . We find that in gSAM (Fig. 4.6a), domain-mean precipitation is maximized for domains in the region of a_{conv} - a_{strat} plane corresponding to strong vertical ascent with some degree of top-heaviness ($\theta_{cs} > 0$). By contrast, regimes of subsidence or shallow ascent are associated with low amounts of mean precipitation. A qualitatively similar pattern exists in observations (Fig. 4.6b), though the magnitude of observed precipitation rates is smaller in CMORPH than in gSAM, which may be due to the difference in resolution between each dataset (Section 4.2.2).

We also examine the mean relationship between large-scale ascent and large-scale precipitable water (PW) in gSAM and ERA5 (Fig 4.6c,d, respectively). Similar to previous studies (Bretherton *et al.*, 2004; Rushley *et al.*, 2018; Wolding *et al.*, 2020), we find that there is a nonlinear relationship between PW and precipitation, as moderate increases in PW correspond to much greater changes in mean precipitation rate. As with precipitation, the lowest (highest) PW values are associated with grid-scale subsidence (ascent). A similar pattern is observed in PW as computed from ERA5 (Figure 4.6d).

The relationship between the structure of large-scale motions and clouds is also evident from the cloud radiative effects (CRE) of different Phases of the a_{conv} - a_{strat} plane. We compute the grid-scale cloud radiative effect at the top of atmosphere (TOA CRE), defined as

$$CRE = F^{all-sky} - F^{clear-sky} \quad (4.10)$$

where $F^{all-sky}$ is the net downward radiative flux at TOA for all-sky conditions, and $F^{clear-sky}$ is the clear-sky flux. The composite CRE is computed from gSAM in the a_{conv} - a_{strat} plane for longwave (Fig. 4.7a) and shortwave (Fig. 4.7b) fluxes separately; their sum, the net CRE, is shown in Figure 4.7c. To provide observational comparison, we also compute CRE using the CERES SYN1DEG dataset using coincident ERA5 data to provide its position in the a_{conv} - a_{strat} plane (Section 4.2.2). We can see that the longwave CRE for both gSAM and CERES (Figures 4.7a and d, respectively) show a positive correlation with a_{strat} , indicating that top-heavy grid-scale circulations are associated with greater longwave

absorption at TOA. This suggests that top-heavy circulations are associated with anvil clouds, which are effective in trapping upwelling terrestrial radiation. Furthermore, the shortwave CRE in gSAM also shows a strong dependence on a_{strat} , with the strongest (negative) shortwave CRE coinciding with the strongest (positive) longwave CRE. The CERES data instead shows no clear dependence on a_{strat} or a_{conv} , instead depending primarily on the amplitude of the grid-scale circulation (R_{cs}). We further note that the shortwave CRE in gSAM (Figure 4.7b) is notably stronger than retrieved by CERES (Figure 4.7e), by about 35 W m^{-2} in the mean. As a result, the net CRE for gSAM is more negative than for CERES, while the latter is close to neutral for all but the strongest circulations ($R_{cs} \gtrsim 2$).

4.5 Small-Scale Circulations and Upscale Impacts

4.5.1 Composite structures of small-scale circulations

We seek to investigate the interaction between the large-scale circulation present in each $2^\circ \times 2^\circ$ domain and the small-scale motions contained within each grid cell. For each $2^\circ \times 2^\circ$ domain, we compute the moisture-space streamfunction ψ (Eq. 4.9), which provides a representation of the small-scale vertical motions removed from the large-scale motions (Fig. 4.8). The streamfunctions are composited by Phase, with shading indicating the composite moisture-sorted total vertical velocity field w (without the mean removed). By sign convention, a negative streamfunction (dashed contours) corresponds to counter-clockwise flow in the (η, z) moisture-space plane. To minimize noise from bin-to-bin variations in the vertical velocity field, values of w are averaged in 5-column chunks. The composite averaging across the many large-scale domains in each phase also reduces the maximum value of w , which is why the color bar in Figure 4.8 saturates at a relatively modest $\sim 10 \text{ cm/s}$.

Beginning with the composite structure of Phase 1 (Fig. 4.8a), we note the presence of quasi-uniform subsidence throughout the troposphere, suggesting that this subsidence may be radiatively driven. In the marine boundary layer, an anomalous shallow overturning circulation exists in moisture space, with air being moved from dry columns to moist columns in the lower branch, and a return flow from moist columns back to dry columns in the lower troposphere (below 2 km altitude). Anomalous vertical motions are generally shallow.

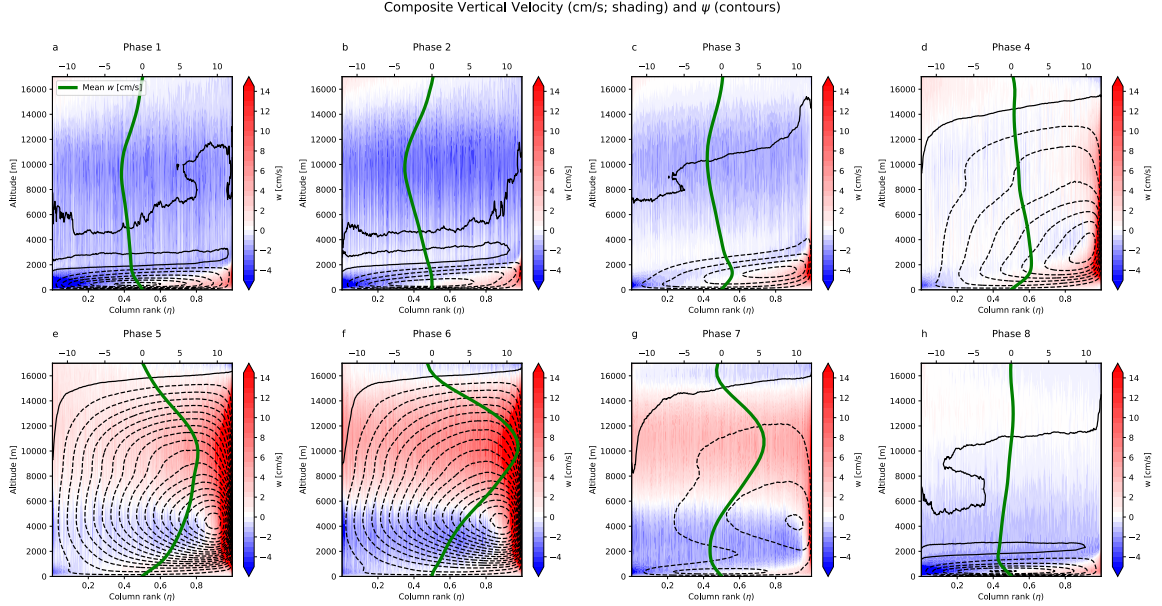


Figure 4.8: Composite means of sub grid-scale vertical velocity (shading) and moisture-space circulation ψ (contours). Profile of mean vertical velocity is also shown. Data are averaged over 5 columns to reduce the noisiness of the sub grid-scale vertical velocity.

In Phase 2 (Fig. 4.8b), we see that the structure of the circulation is generally similar to that in Phase 1. However, we observe that the broad-scale subsidence is slightly stronger in the upper troposphere relative to Phase 1, resulting in a local minimum in \bar{w} at ~ 11 km in height. Additionally, there is a strengthening and deepening of the composite upward motions of the moistest columns ($\eta \gtrsim 0.95$) at low-levels.

In Phase 3 (Fig. 4.8c) the composite vertical motions of the moistest columns are stronger and deeper than those in Phase 2. We note that the vertical structure of \bar{w} has evolved to have a shallow layer of mean ascent near the surface, but deep vertical motions do exist in the moistest columns of the composite structure. We additionally note that the small-scale circulation has deepened slightly, with a convective outflow occurring higher in the troposphere.

In Phase 4 (Fig. 4.8d), the character of the circulation is markedly different. The ascending branch of the circulation is now much deeper and stronger, with streamfunction contours becoming almost vertical above $\eta \gtrsim 0.95$. The descending branch, by comparison,

is spread across a large fraction of the domain. As in Phase 3, the deepest convection is contained in the moistest columns. The broad-scale subsidence evident in the drier columns in preceding phases is greatly diminished. With the height of the streamfunction minimum rising to ~ 3 km, the inflow to the ascending branch of the circulation appears to span a considerable range of depths, reminiscent of the “deep inflow” reported by *Kuo and Neelin* (2022).

In Phase 5 (Fig. 4.8e) the circulation again strengthens, with the moistest columns ($\eta \gtrsim 0.95$) undergoing stronger ascent. This narrow band of deep convection is superposed on a dipole structure of ascending air above 5km, and descending air below it. This dipole structure implies some amount of mid-level convergence. Such mid-level inflow is a well-documented feature of the anvil clouds of mature MCSs (*Houze*, 1997), and has been connected to the maintenance of organized convective systems (*Masunaga*, 2014). The contours of the moisture-space streamfunction are nearly horizontal for a large range of η values in the upper troposphere ($\gtrsim 10$ km), suggesting lateral outflow from the deep convection. The interface between these two layers is highest over the moistest columns and descends slightly with increasing η outside of the range of η values undergoing vigorous convection. This pattern continues to Phase 6 (Fig. 4.8f), where the circulations overall weakens slightly, but the broad-scale ascent and descent outside the convective columns are both stronger than in Phase 5.

In Phase 7 (Fig. 4.8g), deep convection is present, though much diminished from its vigorous state in Phase 6. The dominant structure in this phase is the divergent circulation generated by the ascending upper troposphere and the descending lower troposphere. We note that this dipole structure is present for the vast majority of columns, excepting only the highest η -valued columns. The anomalous circulation has weakened substantially from Phase 6, much more so than the mean ascent in the upper troposphere. Finally, in Phase 8 (Fig. 4.8h) the upper troposphere is no longer ascending, and there is general subsidence. The small-scale circulation has now weakened to a similar level as in Phase 1.

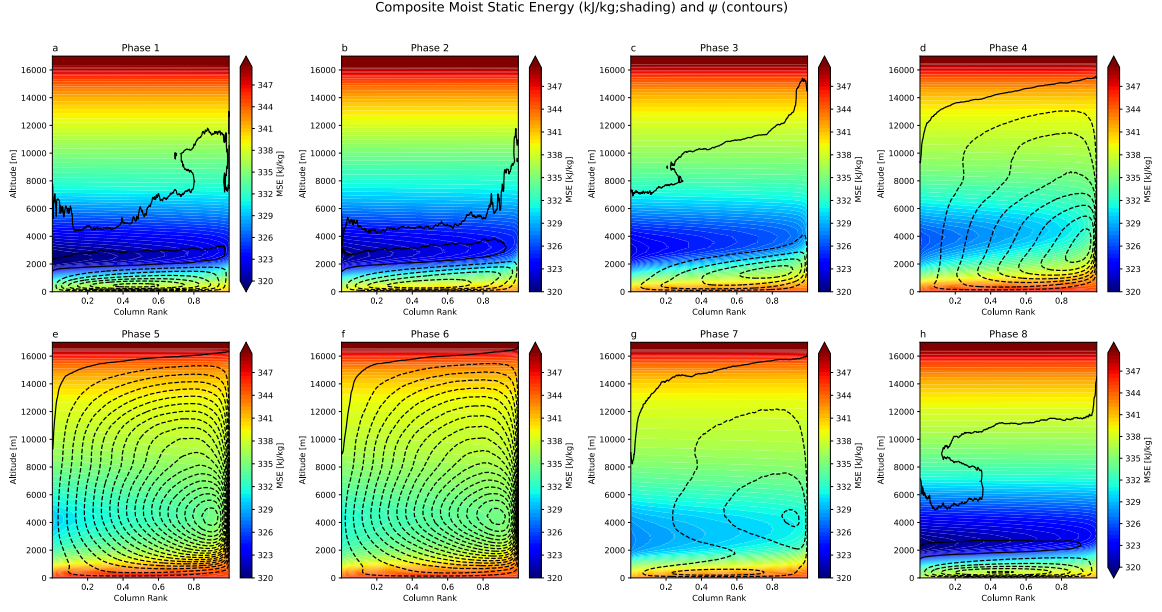


Figure 4.9: As in Figure 4.3, but with shading of moist static energy.

4.5.2 Small-scale circulations, moist static energy, and the role of buoyancy

The circulations shown in Fig. 4.8 bear striking resemblance to the dynamical structures of deep convective systems through different points of their lifecycles. We are thus motivated to examine the extent to which the evolution of the small-scale circulations is coupled to the evolution of thermodynamic fields. The composite structure of the moist static energy field (MSE) is shown in Fig. 4.9. The MSE field in Phases 1 and 2 (Fig. 4.9a-b) generally exhibits a layered structure, with an MSE minimum in the lower free troposphere (2-5 km) above the driest columns. Progressing to Phase 3 (Fig. 4.9c), we observe that boundary layer MSE increases. Furthermore, the MSE contours in the lower troposphere begin to slope upwards and to the right as MSE is preferentially increased in the mid-troposphere over the moistest columns. In Phase 4 (Fig. 4.9d), we see that the anomalous ascent localized over the moistest columns coincides with regions of increased MSE, generating a horizontal MSE gradient between moist and dry columns. The strengthening of the small-scale circulation in Phases 5 and 6 (Figs. 4.9e-f) coincides with both an increase in low-level MSE, as well as a relaxing of this horizontal gradient as the MSE over the driest columns increases. Finally,

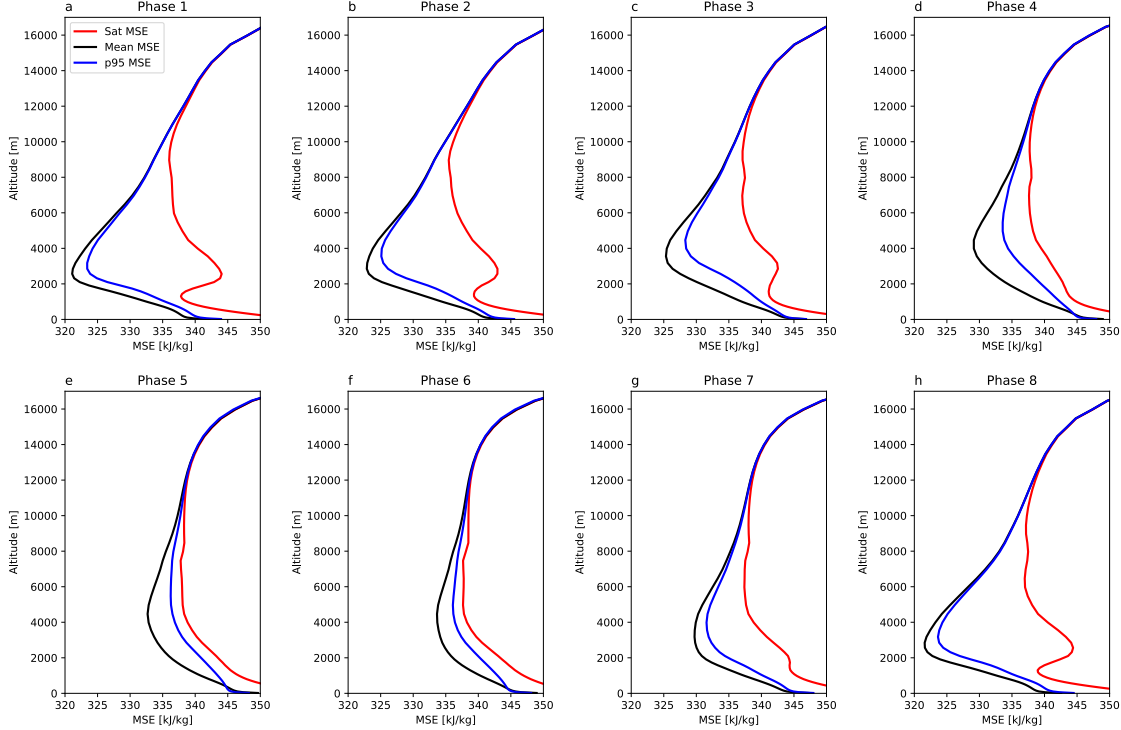


Figure 4.10: Profiles of Phase-averaged saturation MSE (red), mean MSE (black), and the mean MSE of columns in the 95th percentile of column saturation fraction ($\eta > 0.95$; Sec. 34.3.3)

in Phases 7 and 8 (Figs. 4.9g-h), the MSE in the lower-free troposphere decreases to similar levels as in Phase 1.

The evolution of the deep overturning circulation evident in Figure 4.8 can be connected to the development and eventual dissipation of deep convection. This can be illustrated by comparing the domain-mean vertical profile of MSE with the vertical profile of saturation MSE. The difference between these two profiles is proportional to the mean buoyancy felt by saturated convecting parcels, as would exist within deep convective clouds (Arakawa and Schubert, 1974; Khairoutdinov and Randall, 2006). Figure 4.10 shows the composite of the mean MSE profile of the whole domain, as well as the average MSE profile over only columns with $\eta \geq 0.95$, meant to represent the region of deep vertical ascent (Fig. 4.8). We observe that Phases 1-3 (Fig. 4.10a-c) exhibit a wide difference between the saturation and mean

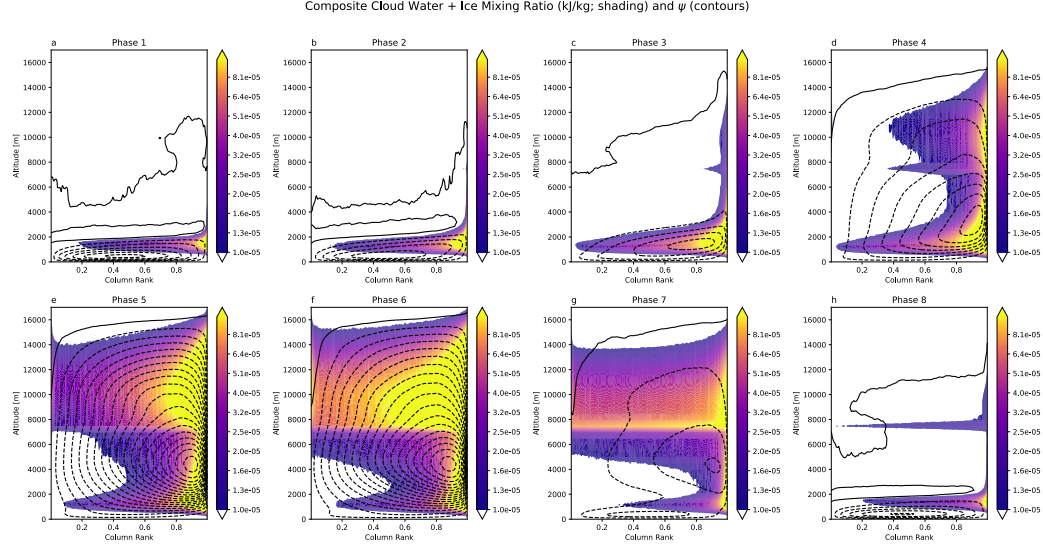


Figure 4.11: As in Figure 4.9, but with shading of combined cloud water and ice mixing ratio.

profiles, indicating a regime of stability and very negative mean buoyancy. For Phases 4-6 (Fig. 4.10d-f), which are associated with much stronger and deeper vertical ascent, we see that the difference between the saturation and mean profiles is greatly minimized. This is especially true for the top 5% of columns, which indicates that the buoyancy is greatest over the moistest columns. The near-neutrality of the buoyancy profile for convective phases is consistent with previous studies (Xu, 1986). Finally, Phases 7 and 8 (Fig. 4.10g-h) exhibit a similar degree of sub-saturation to Phases 1-3. This indicates that the progression of Phases indicated by Fig. 4.4 is strongly coupled to the evolution of buoyancy in the domain.

4.5.3 Small-scale circulations and the development of clouds

The circulation structures of Figure 4.8 are also strongly coupled to the development of clouds within the domain. This can be seen by compositing cloud water and ice mixing ratios in the moisture space plane by Phase as shown in Figure 4.11. Beginning with Phase 1 (Fig. 4.11a), we observe that the composite shows a wide layer of cloud liquid water with small mass mixing ratios ($0.01\text{--}0.1 \text{ g kg}^{-1}$) topping the boundary layer, which we interpret as nearly-uniformly distributed but locally infrequent trade cumulus. In the subsequent Phases

(2-3; Figs. 4.11b-c), there is evidence of sporadic deep clouds in the moistest columns, as well as a growing region of condensate in the upper troposphere, indicative of convective outflow of hydrometeors. For Phases 4-6 (Figs. 4.11d-f) we can see evidence of growing tropical anvil clouds generated by convective outflow. By Phase 7 (Fig. 4.11g), we observe that the deep convective clouds are less pronounced for the moistest columns, but a widespread layer of cloud condensate remains present. Finally, as the circulation decays to Phase 8 (Fig. 4.11h), the anvil thins substantially while the cloudy top of the boundary layer remains. A horizontal band of enhanced cloud near 7km is visible in Figure 4.11h, which is due to the phase change between liquid and ice cloud condensate that occurs over a fixed temperature range in the simple microphysics scheme in gSAM *Khairoutdinov et al.* (2022).

4.6 Bidirectionally of Scale Interactions

4.6.1 Multiscale influences on large-scale evolution

Having documented the co-evolution of the small-scale circulations and the large-scale vertical motions for different regimes of large-scale vertical motion (Figs 4.8-4.10), we now focus on the two-way, cross-scale interactions that mediate this multiscale evolution. We will focus on Phases 4-6 for this analysis, as these Phases have a robust small-scale circulation (Figure 4.8). These Phases correspond to regions of large-scale ascent, and differ primarily in the level of top-heaviness present in the large-scale ascent profile. Furthermore, as is clear from Figure 4.5, large-scale circulations that are in these Phases have a relatively high frequency of either advancing to the next Phase (first upper off-diagonal), regressing to the prior Phase (first lower off-diagonal), or persisting in the same phase (diagonal entries) over a 6-hour period, allowing for robust comparison between large-scale domains undergoing different types of transitions. To facilitate discussion, we shall refer to the set of domains that persist in the same Phase over a 6-hour period as “persisting domains”; domains that advance to the subsequent Phase as “advancing domains”; and domains that regress to the previous Phase as “regressing domains”.

Figure 4.12a-c shows the composite mean of large-scale vertical mass flux for advancing, regressing, and persisting domains. We observe that regressing domains have, on average,

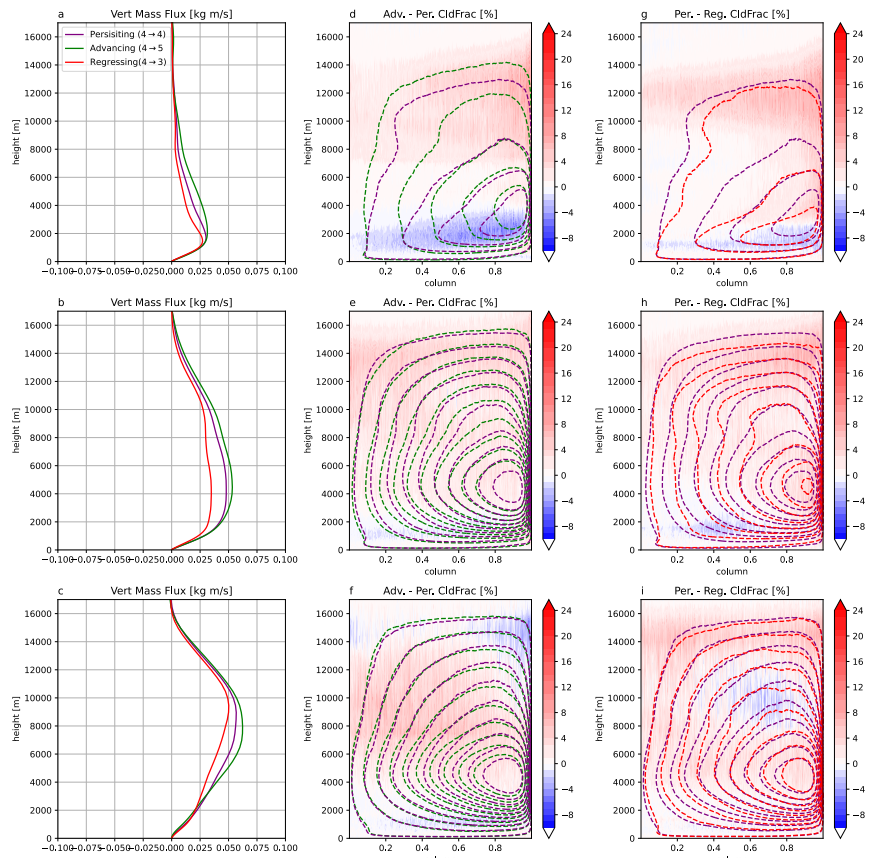


Figure 4.12: (a-c) Composite large-scale vertical mass flux profiles of domains that either advance; (d-f) Composite difference in cloud water and ice mixing ratio between domains undergoing advancing transitions and persistence.

weaker vertical mass flux than persisting domains. Persisting domains in turn have weaker vertical mass flux profiles than advancing domains, though this difference is less than the difference between regressing and persisting domains for domains originating in Phases 5 or 6.

To compare the small-scale structure of clouds in domains undergoing different transitions, we compute the difference in cloud fraction between advancing and persisting domains, as well as between persisting and regressing domains (Fig. 4.12d-f and g-i, respectively). Cloud fraction is here defined as the frequency with which a given coordinate (η, z) of moisture space has a combined cloud water and ice mixing ratio exceeding 10^{-5} kg/kg. Also shown are the composite circulations for each of these groups of domains.

We can observe that the domains that undergo advancing transitions have on average a larger cloud fraction over the domain than do domains that persist in the same phase, particularly at altitudes above 7.5km (Fig. 4.12d-f). A similar pattern holds when comparing domains that persist in the same phase to domains that regress to a previous phase (Fig. 4.12g-i). A notable exception exists for domains advancing from Phase 4 to 5 (Figure 4.12 d and g), where the layer from near the surface to ~ 2 km height is more often cloudy for regressing domains than for persisting or advancing domains.

The small-scale moisture space circulation (Eq. 4.9) is additionally seen to be stronger (i.e., the streamfunction obtains a lower minimum) in the advancing domains than persisting domains (Fig. 4.12d-f). Similarly, the small-scale circulation is stronger in persisting domains than regressing domains (Fig. 4.12g-i).

Thus, Figure 4.12 provides us with some insight into the different structures of the small-scale circulation associated with different evolutions the local large-scale vertical motions. We see that advancing domains, whose large-scale vertical motions increase in top-heaviness, have on average a greater amount and frequency of cloud present in the upper levels of the domain. Additionally, we see that regressing domains have on average both less cloud present at high levels and a weaker small-scale circulation. Therefore, we can identify systematic, robust differences in the small-scale (moisture-space circulation and cloud fraction) of large-scale domains that undergo different evolutions, despite originating in similar large-scale regimes.

4.6.2 Discussion: Are scale interactions a two-way street?

In computing the small-scale circulations present in a domain (Eq. 4.9), the mean vertical motion is removed. Thus, by isolating the large-scale and small-scale motions from one another, we can obtain insight into how these scales of motions interact with one another. The question of how convective systems of differing scales mutually interact has been a longstanding question of tropical metrology from both observational (*Palmer, 1952; Zipser, 1970*) and modeling (*Arakawa and Schubert, 1974; Yano, 1999*) perspectives. In this brief section we will discuss the results described in the present study in the context of the larger discussion surrounding so-called “scale interactions” in the tropics. In this discussion the terms “small-scale” and “large-scale” are still defined as in Section 4.3.1. When comparing to the broader literature on scale interactions, however, the definition of these terms can be relaxed to refer, roughly, to scales smaller or larger than a population of clouds, typically taken as $\mathcal{O}(100 \text{ km})$.

To guide this discussion, it will be useful to explicitly state two hypotheses of how interactions across scales impact the local large-scale evolution. These hypotheses are deliberately constructed as mutually exclusive, extremist perspectives, and are meant to serve as a set of foils with which to juxtapose our findings, rather than as representative perspectives to rebuff:

- **Strict Large-Scale Control (SLSC):** The SLSC hypothesis supposes that the evolution of local large-scale vertical motions is modulated only by the properties of the large-scale circulation. That is, the local evolution of the large-scale flow is completely independent of the small-scale structure, and depends only on the large-scale averages of domain properties. We can express this idea semi-formally as a dynamical equation of the form

$$\partial_t(R_{cs}, \theta_{cs}) = \text{func}(R_{cs}, \theta_{cs}) \quad (4.11)$$

where R_{cs} and θ_{cs} (Eq. 4.6 and 4.7) are controlling (large-scale) parameters for the evolution of large-scale vertical motions. Under SLSC, modeling the evolution of large-scale circulations would not be improved by the inclusion of small-scale motions.

- **Strict Small-Scale Control (SSSC):** The SSSC hypothesis supposes that the evolution of the local large-scale vertical motions is modulated only by the properties of the small-scale circulation. That is, the local evolution of the large-scale flow is completely independent of the properties of the large-scale flow. We can similarly encode this idea as a dynamical system of the form

$$\partial_t(R_{cs}, \theta_{cs}) = \text{func}(\psi) \quad (4.12)$$

where ψ (Eq. 4.9) is the controlling (small-scale) parameter for the evolution of large-scale vertical motions. Under SSSC, the large-scale circulations do not impact their own evolution; rather, the evolution of a large-scale domain is determined only by the circulations contained within, rather than by the influence of large-scale motions.

We can evaluate each of these perspectives critically in light of the present study, in particular Figure 4.12. In considering support for the SLSC hypothesis, we have shown that there are systematic variations in the evolution of the large-scale vertical motions for different initial large-scale conditions (Figure 4.4). We see that domains with large-scale vertical motions that are of greater amplitude (larger R_{cs}), tend to undergo larger changes in R_{cs} and θ_{cs} ; furthermore, the precise character of the evolution also seems to depend on the starting value of θ_{cs} . This indicates that there is a substantial amount of variability in the local evolution of large-scale vertical velocity profiles that depends on the structure of the large-scale (domain mean) vertical motions themselves.

However, we have also shown that there exists a wide range of variance around this mean evolution, as large-scale domains evolve from one Phase to another (Figure 4.5). We found that these different transitions are associated with differing small-scale circulations and cloud distributions; domains that undergo advancing or persisting transitions, indicative of growing top-heaviness of the large-scale profile, are associated with stronger small-scale circulations and increased cloud fraction in the upper troposphere. We have seen that the small-scale circulation is connected to the development and distribution of clouds within the domain (Figure 4.11), suggesting that the evolution of the local large-scale vertical motions may be mediated by the strength and structure of the small-scale circulation. A further

complication is the fact that mean cloud properties also depend on the large-scale motions, as evidenced by Figures 4.6 and 4.7.

We therefore find that our analysis cannot solely support either the SLSC or SSSC hypothesis. The composite large-scale evolution have been shown to depend strongly on both R_{cs} and θ_{cs} (Fig. 4.4). On the other hand, through its interactions with cloud processes, the small-scale circulation can be seen to vary systematically between different large-scale grids that undergo different forward evolutions (Figure 4.12). Rather than supporting either hypothesis unequivocally, this work supports the idea that cross-scale interactions are bi-directional, and that the representation of tropical large-scale dynamics in the tropics is sensitive to the representation of both small-scale and large-scale processes.

4.7 Summary and Conclusions

This study sought to investigate the relationship between large-scale and small-scale vertical circulations over the tropical ocean. Using output from a 40-day integration of a the Global System for Atmospheric Modeling (gSAM), a global storm-resolving model with horizontal grid spacing of $\sim 4\text{km}$, we focused on a region of the tropical Pacific ocean (Fig. 4.1). Large-scale circulations are characterized as mean vertical mass flux profiles computed over $2^\circ \times 2^\circ$ domains; small scale circulations are based on deviations of vertical mass flux from its average in each $2^\circ \times 2^\circ$ domain.

By projecting the large-scale vertical mass flux profile onto its first and second empirical orthogonal modes (Fig. 4.2), we constructed a phase plane where a given large-scale vertical mass flux profile is specified by an ordered pair (a_{conv}, a_{strat}) , with a_{conv} and a_{strat} the normalized values of the first and second principal components (PCs), respectively (Section 4.3.2). The evolution of the large-scale circulation can thus be represented by the bin-mean composite forward, backward, or centered difference of these PCs (Fig. 4.4). Compositing over our data, we find that the large-scale circulation evolves in a manner that bears qualitative resemblance to the prototypical life cycle of convection (*Mapes et al., 2006; Kiladis et al., 2009; Wolding et al., 2020*). We further find that the average magnitude and direction of this composite large-scale evolution depends systematically on the values of a_{conv} and a_{strat} , with the fastest large-scale evolutions occurring for a_{conv} and a_{strat} values cor-

responding to strong, slightly top-heavy large-scale vertical ascent. We also find that these same bins also exhibit an increased precipitation rate, moisture content, and cloud radiative effects (Figs 4.6 and 4.7). Relatively weak and/or subsiding large-scale motions correspond to smaller amplitudes of a_{conv} and a_{strat} as well as weaker precipitation, precipitable water and cloud radiative effects. This behavior is qualitatively similar to what is observed in reanalysis and satellite radiation observations.

To examine the small-scale circulations, we computed an anomalous streamfunction ψ defined in moisture-space coordinates (Eq. 4.9). This streamfunction, computed from deviations of vertical motions from the domain-mean, captures the small-scale mass transport that comprises the domain-mean, large-scale convective motions. Separating the $a_{conv} - a_{strat}$ plane into eight Phases (Fig. 4.3) and examining the composite mean small-scale circulation for each Phase, we find that small-scale motions undergo a systematic co-evolution with the large-scale mass flux (Fig. 4.8). We further find that the evolution of the small-scale circulation is associated with the evolution of moist static energy (Fig. 4.9) and deep convection (Fig. 4.10). Phase composites of cloud content highlight the role of small-scale motions in clouds formation and evolution (Fig. 4.11).

We placed our findings within the context of a larger question of how different scales of motions mutually interact in the tropics. Focusing on regimes of large-scale ascent (Phases 4,5, and 6), we found that large-scale domains that regress in their convective lifecycle have less cloud content and weaker small-scale circulation than large-scale domains that persist or advance in their stage of the convective lifecycle, despite originating from similar large-scale domains (Fig. 4.12). However, we emphasized that the large-scale evolution also has a dependence on the structure of the large-scale vertical motions that cannot be neglected.

There is a clear appetite for the application of global storm-resolving models in modeling long-term weather and climate (*Stevens et al.*, 2019; *Hohenegger et al.*, 2023). In the context of these contemporary and valuable modeling efforts, the present study offers both encouragement and caution. As argued by the proponents of GSRMs, and as evidenced here, the evolution of large-scale vertical motions is mediated by smaller-scale circulations; therefore, accurate representation of the evolution of large-scale motions can be expected to benefit by the improved representation (relative to traditional climate models) of small-scale, convective

tively coupled motions afforded by GSRMs. However, as we have shown here, the large-scale motions are also capable of influencing themselves; therefore, the explicit representation of small-scale convection by GSRMs is not a guarantee that the large-scale structures, or their evolutions, are realistically represented. While the ability of contemporary GSRMs to generate realistic-seeming large-scale structures is notable (as in the so-called Palmer-Turing test of *Stevens et al.* (2019)), further research is warranted to probe the details of these large-scale features and to unravel their bi-directional coupling to small-scale, explicitly represented convection.

Chapter 5

SUMMARY OF DISSERTATION AND CONCLUSIONS

5.1 Synopsis of Dissertation

This dissertation has focused on understanding the multiscale properties of tropical convection. By “multi-scale”, I mean the features of tropical convection (and related phenomena, like clouds and precipitation) that are relevant at a range of scales. In this section I will summarize each chapter of this dissertation, and its bearing on the question of scale interactions in the tropical atmosphere.

- In Chapter 2, the relationship between the spatial structure of precipitation features and their probability of generating extreme rainfall events was analyzed. We found that extreme rainfall events tend to occur within tropical precipitation features that are both larger in areal extent and more spatially localized in its precipitation production. We further found that such extreme rain events are associated with stronger convection (greater reflectivity echoes from GPM radar) at a range of heights. We interpret this finding in terms of mutual interactions between convective elements, mediated by entrainment/detrainment, and the associated drying/moistening of the updraft/environment, respectively. **We therefore conclude that the spatial organization of individual precipitation features influences the generation of tropical extreme rainfall events**

- In Chapter 3, we probe the role of free-tropospheric mixing in modulating the morphology and characteristics of precipitation features. Using idealized simulations of radiative-convective equilibrium (RCE), we perform three numerical experiments with differing eddy diffusivity strengths above 400 m. We find that the simulation with stronger mixing tend to generate smaller features, as well as stronger vertical motions. However, when analyzing the coupling between feature morphology and maximum

precipitation production, we find that modifying the rate of subgrid mixing effects a minimal change. We instead find that within individual precipitation features, the strongest rain events tend to occur within larger principal cores. We further find that larger cores tend to be associated with stronger vertical motions at both the 500 hPa and 200 hPa levels. **We therefore conclude that changes in the strength of subgrid mixing does modulate the mean structure of convection in disaggregated RCE, but only weakly modify the coupling of maximum precipitation production to feature morphology.**

- In Chapter 4, we use a global high-resolution model, with non-parameterized convection, to characterize the interactions between *large-scale circulations* ($> 2^\circ \times 2^\circ$) and *small scale circulations* (deviations from horizontal mean over large-scale domain). We find that the large-scale circulation evolves in a cyclic manner that is evocative of the lifecycle of an individual cumulus. We identify this as an instance of the “prototypical convective lifecycle” described in previous literature (e.g. *Wolding et al. (2020)*). Using a two-mode framework to classify large-scale convective regimes, we additionally find that the small-scale circulations co-evolve with the large-scale vertical motion. This co-evolution is coupled strongly to the development of both spatially limited deep convective clouds and spatially expansive anvil clouds. These larger anvil clouds are identified as a key factor in the development of top-heavy large-scale vertical motion. Finally, we determine that both the strength of the large-scale vertical motion and the strength of the small-scale circulation exert control on the evolution of the large-scale circulation. **We thus conclude that the large-scale tropical motions are influenced by the structure and strength of both large-scale and small-scale vertical motions.**

5.2 Concluding remarks

In an episode 302 of his podcast *Deep Convection*, Professor Adam Sobel interviewed Professor Brian Mapes about his career and published science (which is cited frequently in the foregoing text). In discussing his initial encounter as a graduate student with the literature

surrounding the role of cloud in atmospheric dynamics, Professor Mapes says:

They're just chiseled from marble, these Midwestern summer clouds. It's like landscapes, you could imagine romping and playing on them. Except they change every three minutes... It's like a time evolving landscape. I was just in love with it. And I felt that it had a great amount of life force or something. [...] Vigor, agency, life force. I felt like it was a thing that had some heart to it. And then you come, and so you go into that field of science and you come along and you discover the people running the show have decided that it's a too-complicated-to-care-about response to some forcing. And it drove me batty.

Professor Mapes' frustration is understandable; on the scale of humans and everyday life, the high-impact weather events (and the clouds they are directly associated with) certainty appear to hold leading roles in determining the local weather. To hear a fellow scientist refer to such events as “small-scale variability” due to some larger-scale (and thus ostensibly more *important*) process does smack of regarding trees as merely some response to the presence of forests. However, these same clouds may, indeed, also be regarded as controlled by larger-scale forcings and circulations in certain models of large-scale atmospheric dynamics and climate. Both these viewpoints have enjoyed ample adoption among scientists working at different ends of a space-time axis. At a local scale, particularly over conditionally unstable atmospheres (as exist over the American Midwest), the dynamics of individual cumulus clouds can generally be regarded as discrete entities who consume local instability and convert it into the motions of air that generate precipitation and other weather. At a larger scales, however, it may be helpful to “smooth over” individual convective clouds, and instead regard convection as an implicit process that can be diagnostically treated (as in the weak-temperature gradient framework; *Adames (2022)*). Both view points are useful, if philosophically opposed in some ways.

This dissertation represents, in some ways, my own attempts to reconcile these two points of view. The position that this dissertation takes, ultimately, is one of compromise: while the structure of individual clouds is certainly important for determining local weather (and local extremes; c.f. Ch. 2), so to is the large-scale circulation important in determining

the structure and evolution of individual clouds (c.f. Ch. 4). Thus, the question of whether up-scale or down-scale control is correct is not as meaningful as the question of when, and to what extent, is either direction dominant in determining the evolution of multiscale atmospheric flows.

To conclude this dissertation, I reproduce a passage from Herbert Riehl's seminal text on tropical metrology (*Riehl*, 1954). Riehl, along with several other experts in extratropical meteorology, had arrived in Rio Piedras, Puerto Rico in 1943 to establish the Institute of Tropical Meteorology for the benefit of Allied forces fighting in the Pacific theater of World War II. Riehl recounts his first evening in the tropics, where he and his colleagues seem to have received a message about the dangers of neglecting smaller scales of motion:

On the first evening some of the staff walked along the beach and admired the beauty of the trade cumuli in the moonlight. Well schooled in the ice-crystal theory of formation of rain, they had no suspicions about these clouds with tops near 8,000 feet where the temperature is higher than +10°C. Suddenly, however, the landscape ahead of them began to dim; then it disappeared; a roar approached as from rain hitting roof tops. When some minutes later they stood on a porch, drenched and shivering, they had realized that cloud tops with temperatures below freezing were not needed for production of heavy rain from trade-wind cumulus

Riehl (1954)

It is my hope that further advances in our humble field of atmospheric science may allow us soon to consider, in the same intellectual breath, not only the largest-scale circulations that give rise to the variability observed on Earth, but also the small-scale atmospheric structures that mediate that variability and, in doing so, inspire us all to look up at the sky and ponder our own place in the scale of things.

BIBLIOGRAPHY

- Adames, F., The Basic Equations under Weak Temperature Gradient Balance: Formulation, Scaling, and Types of Convectively Coupled Motions, *Journal of the Atmospheric Sciences*, 79(8), 2087–2108, doi:10.1175/JAS-D-21-0215.1, 2022.
- Adames, F., and J. M. Wallace, Three-Dimensional Structure and Evolution of the Moisture Field in the MJO, *Journal of the Atmospheric Sciences*, 72(10), 3733–3754, doi:10.1175/JAS-D-15-0003.1, publisher: American Meteorological Society Section: Journal of the Atmospheric Sciences, 2015.
- Ahmed, F., and C. Schumacher, Convective and Stratiform Components of the Precipitation-Moisture Relationship, *Geophysical Research Letters*, 42(23), 10,453–10,462, doi:10.1002/2015GL066957, eprint: <https://agupubs.onlinelibrary.wiley.com/doi/10.1002/2015GL066957>, 2015.
- Angulo-Umana, P., and D. Kim, Mesoscale convective clustering enhances tropical precipitation, *Science Advances*, 9(2), eabo5317, doi:10.1126/sciadv.abo5317, publisher: American Association for the Advancement of Science, 2023.
- Arakawa, A., The Cumulus Parameterization Problem: Past, Present, and Future, *Journal of Climate*, 17(13), 2493–2525, doi:10.1175/1520-0442(2004)017j2493:RATCPP;2.0.CO;2, publisher: American Meteorological Society Section: Journal of Climate, 2004.
- Arakawa, A., and W. H. Schubert, Interaction of a Cumulus Cloud Ensemble with the Large-Scale Environment, Part I, *Journal of the Atmospheric Sciences*, 31(3), 674–701, doi:10.1175/1520-0469(1974)031j0674:IOACCE;2.0.CO;2, publisher: American Meteorological Society Section: Journal of the Atmospheric Sciences, 1974.
- Back, L. E., and C. S. Bretherton, A Simple Model of Climatological Rainfall and Vertical Motion Patterns over the Tropical Oceans, *Journal of Climate*, 22(23), 6477–6497, doi:10.1175/2009JCLI2393.1, publisher: American Meteorological Society Section: Journal of Climate, 2009.
- Back, L. E., Z. Hansen, and Z. Handlos, Estimating Vertical Motion Profile Top-Heaviness: Reanalysis Compared to Satellite-Based Observations and Stratiform Rain Fraction, *Journal of the Atmospheric Sciences*, 74(3), 855–864, doi:10.1175/JAS-D-16-0062.1, publisher: American Meteorological Society Section: Journal of the Atmospheric Sciences, 2017.

- Bao, J., and S. C. Sherwood, The Role of Convective Self-Aggregation in Extreme Instantaneous Versus Daily Precipitation, *Journal of Advances in Modeling Earth Systems*, 11(1), 19–33, doi:10.1029/2018MS001503, 2019.
- Bao, J., S. C. Sherwood, M. Colin, and V. Dixit, The Robust Relationship Between Extreme Precipitation and Convective Organization in Idealized Numerical Modeling Simulations, *Journal of Advances in Modeling Earth Systems*, 9(6), 2291–2303, doi:10.1002/2017MS001125, 2017.
- Bao, J., B. Stevens, L. Kluft, and C. Muller, Intensification of daily tropical precipitation extremes from more organized convection, *Science Advances*, 10(8), eadj6801, doi:10.1126/sciadv.adj6801, publisher: American Association for the Advancement of Science, 2024.
- Bernardes, M., and L. Back, Integrating Thermodynamic and Dynamic Views on the Control of the Top-Heaviness of Convection in the Pacific ITCZ With Weak Temperature Gradient Simulations, *Journal of Advances in Modeling Earth Systems*, 16(2), e2022MS003,455, doi:10.1029/2022MS003455, eprint: <https://onlinelibrary.wiley.com/doi/pdf/10.1029/2022MS003455>, 2024.
- Bretherton, C. S., and P. K. Smolarkiewicz, Gravity Waves, Compensating Subsidence and Detrainment around Cumulus Clouds, *Journal of the Atmospheric Sciences*, 46(6), 740–759, doi:10.1175/1520-0469(1989)046;0740:GWCSAD;2.0.CO;2, publisher: American Meteorological Society Section: Journal of the Atmospheric Sciences, 1989.
- Bretherton, C. S., M. E. Peters, and L. E. Back, Relationships between Water Vapor Path and Precipitation over the Tropical Oceans, *Journal of Climate*, 17(7), 1517–1528, doi:10.1175/1520-0442(2004)017;1517:RBWVPA;2.0.CO;2, publisher: American Meteorological Society Section: Journal of Climate, 2004.
- Bretherton, C. S., P. N. Blossey, and M. Khairoutdinov, An Energy-Balance Analysis of Deep Convective Self-Aggregation above Uniform SST, *Journal of the Atmospheric Sciences*, 62(12), 4273–4292, doi:10.1175/JAS3614.1, 2005.
- Brown, R. G., and C. Zhang, Variability of Midtropospheric Moisture and Its Effect on Cloud-Top Height Distribution during TOGA COARE*, *Journal of the Atmospheric Sciences*, 54(23), 2760–2774, doi:10.1175/1520-0469(1997)054;2760:VOMMAI;2.0.CO;2, publisher: American Meteorological Society Section: Journal of the Atmospheric Sciences, 1997.
- Carenso, M., B. Fildier, R. Roca, and T. Fiolleau, Multiscale precipitation extremes are determined by rain event morphology in very deep convective systems, doi:10.22541/essoar.172909079.94970992/v1, 2024.

Cheng, Y.-M., J. Dias, G. Kiladis, Z. Feng, and L. R. Leung, Mesoscale Convective Systems Modulated by Convectively Coupled Equatorial Waves, *Geophysical Research Letters*, 50(10), e2023GL103,335, doi:10.1029/2023GL103335, _eprint: <https://onlinelibrary.wiley.com/doi/pdf/10.1029/2023GL103335>, 2023.

Chien, M.-T., and D. Kim, Representation of the Convectively Coupled Kelvin Waves in Modern Reanalysis Products, *Journal of the Atmospheric Sciences*, 80(2), 397–418, doi:10.1175/JAS-D-22-0067.1, publisher: American Meteorological Society Section: Journal of the Atmospheric Sciences, 2023.

de Rooy, W. C., P. Bechtold, K. Fröhlich, C. Hohenegger, H. Jonker, D. Mironov, A. Pier Siebesma, J. Teixeira, and J.-I. Yano, Entrainment and detrainment in cumulus convection: an overview, *Quarterly Journal of the Royal Meteorological Society*, 139(670), 1–19, doi:10.1002/qj.1959, _eprint: <https://onlinelibrary.wiley.com/doi/pdf/10.1002/qj.1959>, 2013.

Emanuel, K. A., J. David Neelin, and C. S. Bretherton, On Large-Scale Circulations in Convecting Atmospheres, *Quarterly Journal of the Royal Meteorological Society*, 120(519), 1111–1143, doi:10.1002/qj.49712051902, _eprint: <https://rmets.onlinelibrary.wiley.com/doi/pdf/10.1002/qj.49712051902>, 1994.

Emanuel, K. A., A. A. Wing, and E. M. Vincent, Radiative-convective instability: Radiative-Convective Instability, *Journal of Advances in Modeling Earth Systems*, 6(1), 75–90, doi:10.1002/2013MS000270, 2014.

Feng, Z., L. R. Leung, N. Liu, J. Wang, R. A. Houze Jr, J. Li, J. C. Hardin, D. Chen, and J. Guo, A Global High-Resolution Mesoscale Convective System Database Using Satellite-Derived Cloud Tops, Surface Precipitation, and Tracking, *Journal of Geophysical Research: Atmospheres*, 126(8), e2020JD034,202, doi:10.1029/2020JD034202, _eprint: <https://onlinelibrary.wiley.com/doi/pdf/10.1029/2020JD034202>, 2021.

Fraser, A. B., The white box: The mean mechanics of the cumulus cycle, *Quarterly Journal of the Royal Meteorological Society*, 94(399), 71–87, doi:10.1002/qj.49709439908, _eprint: <https://onlinelibrary.wiley.com/doi/pdf/10.1002/qj.49709439908>, 1968.

Fuchs-Stone, , D. J. Raymond, and S. Sentić, A Simple Model of Convectively Coupled Equatorial Rossby Waves, *Journal of Advances in Modeling Earth Systems*, 11(1), 173–184, doi:10.1029/2018MS001433, _eprint: <https://onlinelibrary.wiley.com/doi/pdf/10.1029/2018MS001433>, 2019.

Hamada, A., Y. N. Takayabu, C. Liu, and E. J. Zipser, Weak linkage between the heaviest rainfall and tallest storms, *Nature Communications*, 6(1), 6213, doi: 10.1038/ncomms7213, number: 1 Publisher: Nature Publishing Group, 2015.

Haman, K., On the influence of convective clouds on the large scale stratification, *Tellus*, 21(1), 40–53, doi:10.1111/j.2153-3490.1969.tb00416.x, eprint: <https://onlinelibrary.wiley.com/doi/pdf/10.1111/j.2153-3490.1969.tb00416.x>, 1969.

Hartmann, D. L., H. H. Hendon, and R. A. Houze, Some Implications of the Mesoscale Circulations in Tropical Cloud Clusters for Large-Scale Dynamics and Climate, *Journal of the Atmospheric Sciences*, 41(1), 113–121, doi:10.1175/1520-0469(1984)041j0113:SIOTMC;2.0.CO;2, publisher: American Meteorological Society Section: Journal of the Atmospheric Sciences, 1984.

Hermawan, E., S. W. Lubis, T. Harjana, A. Purwaningsih, Risyanto, A. Ridho, D. F. Andarini, D. N. Ratri, and R. Widyaningsih, Large-Scale Meteorological Drivers of the Extreme Precipitation Event and Devastating Floods of Early-February 2021 in Semarang, Central Java, Indonesia, *Atmosphere*, 13(7), 1092, doi: 10.3390/atmos13071092, number: 7 Publisher: Multidisciplinary Digital Publishing Institute, 2022.

Hersbach, H., et al., ERA5 Hourly Data on Single Levels from 1979 to Present, 2020.

Hohenegger, C., et al., ICON-Sapphire: simulating the components of the Earth system and their interactions at kilometer and subkilometer scales, *Geoscientific Model Development*, 16(2), 779–811, doi:10.5194/gmd-16-779-2023, publisher: Copernicus GmbH, 2023.

Holloway, C. E., and J. D. Neelin, Moisture Vertical Structure, Column Water Vapor, and Tropical Deep Convection, *Journal of the Atmospheric Sciences*, 66(6), 1665–1683, doi:10.1175/2008JAS2806.1, 2009.

Holton, J. R., and G. J. Hakim, *An introduction to dynamic meteorology*, fifth edition ed., Academic Press, Amsterdam, 2013.

Houze, R. A., Stratiform Precipitation in Regions of Convection: A Meteorological Paradox?, *Bulletin of the American Meteorological Society*, 78(10), 2179–2196, doi:10.1175/1520-0477(1997)078j2179:SPIROC;2.0.CO;2, publisher: American Meteorological Society Section: Bulletin of the American Meteorological Society, 1997.

Houze, R. A., Mesoscale convective systems, *Reviews of Geophysics*, 42(4), doi:10.1029/2004RG000150, eprint: <https://onlinelibrary.wiley.com/doi/pdf/10.1029/2004RG000150>, 2004.

Houze, R. A., 100 Years of Research on Mesoscale Convective Systems, *Meteorological Monographs*, 59(1), 17.1–17.54, doi:10.1175/AMSMONOGRAPH-D-18-0001.1, publisher: American Meteorological Society Section: Meteorological Monographs, 2018.

Houze, R. A., Jr., Cloud Clusters and Large-Scale Vertical Motions in the Tropics, *Journal of the Meteorological Society of Japan. Ser. II*, 60(1), 396–410, doi: 10.2151/jmsj1965.60.1_396, 1982.

Houze Jr., R. A., Observed structure of mesoscale convective systems and implications for large-scale heating, *Quarterly Journal of the Royal Meteorological Society*, 115(487), 425–461, doi:10.1002/qj.49711548702, eprint: <https://rmets.onlinelibrary.wiley.com/doi/pdf/10.1002/qj.49711548702>, 1989.

Iguchi, T., S. Seto, R. Meneghini, N. Yoshida, J. Awaka, M. Le, V. Chandrasekar, S. Brodzik, and T. Kubota, GPM/DPR Level-2 Algorithm Theoretical Basis Document, p. 127.

Iguchi, T., T. Kozu, R. Meneghini, J. Awaka, and K. Okamoto, Rain-Proiling Algorithm for the TRMM Precipitation Radar, *Journal of Applied Meteorology and Climatology*, 39(12), 2038–2052, doi:10.1175/1520-0450(2001)040;2038:RPAFTT;2.0.CO;2, publisher: American Meteorological Society Section: Journal of Applied Meteorology and Climatology, 2000.

Inoue, K., F. Adames, and K. Yasunaga, Vertical Velocity Profiles in Convectively Coupled Equatorial Waves and MJO: New Diagnoses of Vertical Velocity Profiles in the Wavenumber–Frequency Domain, *Journal of the Atmospheric Sciences*, 77(6), 2139–2162, doi:10.1175/JAS-D-19-0209.1, 2020.

Inoue, K., M. Biasutti, and A. M. Fridlind, Evidence that Horizontal Moisture Advection Regulates the Ubiquitous Amplification of Rainfall Variability over Tropical Oceans, *Journal of the Atmospheric Sciences*, 78(2), 529–547, doi:10.1175/JAS-D-20-0201.1, publisher: American Meteorological Society Section: Journal of the Atmospheric Sciences, 2021.

IPCC, *Climate Change 2021 – The Physical Science Basis: Working Group I Contribution to the Sixth Assessment Report of the Intergovernmental Panel on Climate Change*, 1 ed., Cambridge University Press, doi:10.1017/9781009157896, 2023.

Jiang, X., F. Adames, D. Kim, E. D. Maloney, H. Lin, H. Kim, C. Zhang, C. A. DeMott, and N. P. Klingaman, Fifty Years of Research on the Madden-Julian Oscillation: Recent Progress, Challenges, and Perspectives, *Journal of Geophysical Research: Atmospheres*, 125(17), e2019JD030911, doi:10.1029/2019JD030911, eprint: <https://onlinelibrary.wiley.com/doi/pdf/10.1029/2019JD030911>, 2020.

Joyce, R. J., J. E. Janowiak, P. A. Arkin, and P. Xie, CMORPH: A Method that Produces Global Precipitation Estimates from Passive Microwave and Infrared Data at High Spatial and Temporal Resolution, *Journal of Hydrometeorology*, 5(3), 487–503, doi:10.1175/1525-7541(2004)005;0487:CAMTPG;2.0.CO;2, publisher: American Meteorological Society Section: Journal of Hydrometeorology, 2004.

Khairoutdinov, M., and D. Randall, High-Resolution Simulation of Shallow-to-Deep Convection Transition over Land, *Journal of the Atmospheric Sciences*, 63(12), 3421–3436, doi:10.1175/JAS3810.1, publisher: American Meteorological Society Section: Journal of the Atmospheric Sciences, 2006.

Khairoutdinov, M. F., and D. A. Randall, Cloud Resolving Modeling of the ARM Summer 1997 IOP: Model Formulation, Results, Uncertainties, and Sensitivities, *Journal of the Atmospheric Sciences*, 60(4), 607–625, doi:10.1175/1520-0469(2003)060j0607:CRMOTA;2.0.CO;2, publisher: American Meteorological Society Section: Journal of the Atmospheric Sciences, 2003.

Khairoutdinov, M. F., P. N. Blossey, and C. S. Bretherton, Global System for Atmospheric Modeling: Model Description and Preliminary Results, *Journal of Advances in Modeling Earth Systems*, 14(6), e2021MS002,968, doi:10.1029/2021MS002968, _eprint: <https://onlinelibrary.wiley.com/doi/pdf/10.1029/2021MS002968>, 2022.

Khouider, B., and A. J. Majda, Multicloud Models for Organized Tropical Convection: Enhanced Congestus Heating, *Journal of the Atmospheric Sciences*, 65(3), 895–914, doi:10.1175/2007JAS2408.1, publisher: American Meteorological Society Section: Journal of the Atmospheric Sciences, 2008.

Kiladis, G. N., M. C. Wheeler, P. T. Haertel, K. H. Straub, and P. E. Roundy, Convectively coupled equatorial waves, *Reviews of Geophysics*, 47(2), doi:10.1029/2008RG000266, _eprint: <https://onlinelibrary.wiley.com/doi/pdf/10.1029/2008RG000266>, 2009.

Kim, D., M.-S. Ahn, I.-S. Kang, and A. D. D. Genio, Role of Longwave Cloud–Radiation Feedback in the Simulation of the Madden–Julian Oscillation, *Journal of Climate*, 28(17), 6979–6994, doi:10.1175/JCLI-D-14-00767.1, publisher: American Meteorological Society Section: Journal of Climate, 2015.

Kuo, Y.-H., and J. D. Neelin, Conditions for Convective Deep Inflow, *Geophysical Research Letters*, 49(20), e2022GL100,552, doi:10.1029/2022GL100552, _eprint: <https://onlinelibrary.wiley.com/doi/pdf/10.1029/2022GL100552>, 2022.

Lafore, J.-P., and M. W. Moncrieff, A Numerical Investigation of the Organization and Interaction of the Convective and Stratiform Regions of Tropical Squall Lines, *Journal of the Atmospheric Sciences*, 46(4), 521–544, doi:10.1175/1520-0469(1989)046j0521:ANIOTO;2.0.CO;2, publisher: American Meteorological Society Section: Journal of the Atmospheric Sciences, 1989.

Liu, N., L. R. Leung, and Z. Feng, Global Mesoscale Convective System Latent Heating Characteristics from GPM Retrievals and an MCS Tracking Dataset, *Journal of Climate*, 34(21), 8599–8613, doi:10.1175/JCLI-D-20-0997.1, publisher: American Meteorological Society Section: Journal of Climate, 2021.

Mapes, B., S. Tulich, J. Lin, and P. Zuidema, The Mesoscale Convection Life Cycle: Building Block or Prototype for Large-Scale Tropical Waves?, *Dynamics of Atmospheres and Oceans*, 42(1-4), 3–29, doi:10.1016/j.dynatmoce.2006.03.003, 2006.

Mapes, B. E., Gregarious Tropical Convection, *Journal of the Atmospheric Sciences*, 50(13), 2026–2037, doi:10.1175/1520-0469(1993)050;2026:GTC;2.0.CO;2, publisher: American Meteorological Society Section: Journal of the Atmospheric Sciences, 1993.

Mapes, B. E., Equilibrium Vs. Activation Control of Large-Scale Variations of Tropical Deep Convection, in *The Physics and Parameterization of Moist Atmospheric Convection*, edited by R. K. Smith, NATO ASI Series, pp. 321–358, Springer Netherlands, Dordrecht, doi:10.1007/978-94-015-8828-7_13, 1997.

Mapes, B. E., The Large-Scale Part of Tropical Mesoscale Convective System Circulations: A Linear Vertical Spectral Band Model, *Journal of the Meteorological Society of Japan. Ser. II*, 76(1), 29–55, doi:10.2151/jmsj1965.76.1_29, 1998.

Mapes, B. E., Convective Inhibition, Subgrid-Scale Triggering Energy, and Stratiform Instability in a Toy Tropical Wave Model, *Journal of the Atmospheric Sciences*, 57(10), 1515–1535, doi:10.1175/1520-0469(2000)057;1515:CISSTE;2.0.CO;2, publisher: American Meteorological Society Section: Journal of the Atmospheric Sciences, 2000.

Masunaga, H., Free-tropospheric moisture convergence and tropical convective regimes, *Geophysical Research Letters*, 41(23), 8611–8618, doi:10.1002/2014GL062301, eprint: <https://onlinelibrary.wiley.com/doi/pdf/10.1002/2014GL062301>, 2014.

Masunaga, H., The Edge Intensification of Eastern Pacific ITCZ Convection, *Journal of Climate*, 36(10), 3469–3480, doi:10.1175/JCLI-D-22-0382.1, 2023.

Masunaga, H., and H. Takahashi, The Energetics of the Lagrangian Evolution of Tropical Convective Systems, *Journal of the Atmospheric Sciences*, 81(4), 783–799, doi:10.1175/JAS-D-23-0141.1, publisher: American Meteorological Society Section: Journal of the Atmospheric Sciences, 2024.

Matsuno, T., Quasi-Geostrophic Motions in the Equatorial Area, *Journal of the Meteorological Society of Japan. Ser. II*, 44(1), 25–43, doi:10.2151/jmsj1965.44.1_25, 1966.

Muller, C. J., P. A. O’Gorman, and L. E. Back, Intensification of Precipitation Extremes with Warming in a Cloud-Resolving Model, *Journal of Climate*, 24(11), 2784–2800, doi:10.1175/2011JCLI3876.1, publisher: American Meteorological Society Section: Journal of Climate, 2011.

Neelin, J. D., and I. M. Held, Modeling Tropical Convergence Based on the Moist Static Energy Budget, *Monthly Weather Review*, 115(1), 3–12, doi:10.1175/1520-0493(1987)115j0003:MTCBOT;2.0.CO;2, publisher: American Meteorological Society Section: Monthly Weather Review, 1987.

Nesbitt, S. W., R. Cifelli, and S. A. Rutledge, Storm Morphology and Rainfall Characteristics of TRMM Precipitation Features, *Monthly Weather Review*, 134(10), 2702–2721, doi:10.1175/MWR3200.1, 2006.

O’Gorman, P. A., and T. Schneider, The physical basis for increases in precipitation extremes in simulations of 21st-century climate change, *Proceedings of the National Academy of Sciences*, 106(35), 14,773–14,777, doi:10.1073/pnas.0907610106, publisher: Proceedings of the National Academy of Sciences, 2009.

Orlanski, I., A Rational Subdivision of Scales for Atmospheric Processes, *Bulletin of the American Meteorological Society*, 56(5), 527–530, publisher: American Meteorological Society, 1975.

O’Donnell, G. L., and A. A. Wing, Precipitation Extremes and Their Modulation by Convective Organization in RCEMIP, *Journal of Advances in Modeling Earth Systems*, 16(11), e2024MS004,535, doi:10.1029/2024MS004535, eprint: <https://onlinelibrary.wiley.com/doi/pdf/10.1029/2024MS004535>, 2024.

Palmer, C. E., Reviews of modern meteorology—5. Tropical meteorology, *Quarterly Journal of the Royal Meteorological Society*, 78(336), 126–164, doi:10.1002/qj.49707833603, eprint: <https://onlinelibrary.wiley.com/doi/pdf/10.1002/qj.49707833603>, 1952.

Pedlosky, J., *Geophysical fluid dynamics*, Springer study edition, 2nd ed ed., Springer, New York Berlin Paris [etc.], 1987.

Pendergrass, A. G., K. A. Reed, and B. Medeiros, The Link Between Extreme Precipitation and Convective Organization in a Warming Climate: Global Radiative-Convective Equilibrium Simulations, *Geophysical Research Letters*, 43(21), doi:10.1002/2016GL071285, 2016.

Randall, D., M. Khairoutdinov, A. Arakawa, and W. Grabowski, Breaking the Cloud Parameterization Deadlock, *Bulletin of the American Meteorological Society*, 84(11), 1547–1564, doi:10.1175/BAMS-84-11-1547, publisher: American Meteorological Society Section: Bulletin of the American Meteorological Society, 2003.

Raymond, D. J., Thermodynamic control of tropical rainfall, *Quarterly Journal of the Royal Meteorological Society*, 126(564), 889–898, doi:10.1002/qj.49712656406, eprint: <https://onlinelibrary.wiley.com/doi/pdf/10.1002/qj.49712656406>, 2000.

Raymond, D. J., S. L. Sessions, A. H. Sobel, and Fuchs, The Mechanics of Gross Moist Stability: Gross Moist Stability, *Journal of Advances in Modeling Earth Systems*, 1(3), n/a–n/a, doi:10.3894/JAMES.2009.1.9, 2009.

Riehl, H., *Tropical meteorology*, McGraw-Hill, pages: 392, 1954.

Riehl, H., On the Heat Balance in the Equatorial Trough Zone, *Geophysica*, 6, 503–538, 1958.

Roca, R., and T. Fiolleau, Extreme Precipitation in the Tropics Is Closely Associated with Long-Lived Convective Systems, *Communications Earth & Environment*, 1(1), 1–6, doi:10.1038/s43247-020-00015-4, bandiera_abtest: a Cc_license_type: cc_by Cg_type: Nature Research Journals Number: 1 Primary_atype: Research Publisher: Nature Publishing Group Subject_term: Atmospheric dynamics;Climate sciences;Hydrology Subject_term_id: atmospheric-dynamics;climate-sciences;hydrology, 2020.

Roca, R., J. Aublanc, P. Chambon, T. Fiolleau, and N. Viltard, Robust Observational Quantification of the Contribution of Mesoscale Convective Systems to Rainfall in the Tropics, *Journal of Climate*, 27(13), 4952–4958, doi:10.1175/JCLI-D-13-00628.1, publisher: American Meteorological Society Section: Journal of Climate, 2014.

Rushley, S. S., D. Kim, C. S. Bretherton, and M. Ahn, Reexamining the Nonlinear Moisture-Precipitation Relationship Over the Tropical Oceans, *Geophysical Research Letters*, 45(2), 1133–1140, doi:10.1002/2017GL076296, 2018.

Rutan, D. A., S. Kato, D. R. Doelling, F. G. Rose, L. T. Nguyen, T. E. Caldwell, and N. G. Loeb, CERES Synoptic Product: Methodology and Validation of Surface Radiant Flux, *Journal of Atmospheric and Oceanic Technology*, 32(6), 1121–1143, doi:10.1175/JTECH-D-14-00165.1, publisher: American Meteorological Society Section: Journal of Atmospheric and Oceanic Technology, 2015.

Sakaeda, N., and G. Torri, The Behaviors of Intraseasonal Cloud Organization During DYNAMO/AMIE, *Journal of Geophysical Research: Atmospheres*, 127(7), e2021JD035749, doi:10.1029/2021JD035749, _eprint: <https://agupubs.onlinelibrary.wiley.com/doi/pdf/10.1029/2021JD035749>, 2022.

Satoh, M., B. Stevens, F. Judt, M. Khairoutdinov, S.-J. Lin, W. M. Putman, and P. Düben, Global Cloud-Resolving Models, *Current Climate Change Reports*, 5(3), 172–184, doi:10.1007/s40641-019-00131-0, 2019.

Schulz, H., and B. Stevens, Observing the Tropical Atmosphere in Moisture Space, *Journal of the Atmospheric Sciences*, 75(10), 3313–3330, doi:10.1175/JAS-D-17-0375.1, 2018.

Schumacher, C., R. A. Houze, and I. Kraucunas, The Tropical Dynamical Response to Latent Heating Estimates Derived from the TRMM Precipitation Radar, *Journal of the Atmospheric Sciences*, 61(12), 1341–1358, doi:10.1175/1520-0469(2004)061j1341:TTDRTL;2.0.CO;2, publisher: American Meteorological Society Section: Journal of the Atmospheric Sciences, 2004.

Semie, A. G., and S. Bony, Relationship Between Precipitation Extremes and Convective Organization Inferred from Satellite Observations, *Geophysical Research Letters*, 47(9), doi: 10.1029/2019GL086927, 2020.

Senior, N. V., A. J. Matthews, B. G. M. Webber, S. Webster, R. W. Jones, D. S. Permana, J. A. I. Paski, and R. Fadila, Extreme precipitation at Padang, Sumatra triggered by convectively coupled Kelvin waves, *Quarterly Journal of the Royal Meteorological Society*, n/a(n/a), doi:10.1002/qj.4506, eprint: <https://onlinelibrary.wiley.com/doi/pdf/10.1002/qj.4506>, 2022.

Sokol, A. B., and D. L. Hartmann, Congestus Mode Invigoration by Convective Aggregation in Simulations of Radiative-Convective Equilibrium, *Journal of Advances in Modeling Earth Systems*, 14(7), e2022MS003,045, doi:10.1029/2022MS003045, eprint: <https://onlinelibrary.wiley.com/doi/pdf/10.1029/2022MS003045>, 2022.

Stevens, B., et al., DYAMOND: the DYnamics of the Atmospheric general circulation Modeled On Non-hydrostatic Domains, *Progress in Earth and Planetary Science*, 6(1), 61, doi: 10.1186/s40645-019-0304-z, 2019.

Takayabu, Y. N., Large-Scale Cloud Disturbances Associated with Equatorial Waves, *Journal of the Meteorological Society of Japan. Ser. II*, 72(3), 433–449, doi: 10.2151/jmsj1965.72.3433, 1994.

Tiedtke, M., A Comprehensive Mass Flux Scheme for Cumulus Parameterization in Large-Scale Models, *Monthly Weather Review*, 117(8), 1779–1800, doi:10.1175/1520-0493(1989)117j1779:ACMFSF;2.0.CO;2, publisher: American Meteorological Society Section: Monthly Weather Review, 1989.

Tomassini, L., et al., Confronting the Convective Gray Zone in the Global Configuration of the Met Office Unified Model, *Journal of Advances in Modeling Earth Systems*, 15(5), e2022MS003,418, doi:10.1029/2022MS003418, eprint: <https://onlinelibrary.wiley.com/doi/pdf/10.1029/2022MS003418>, 2023.

Tompkins, A. M., and A. G. Semie, Organization of Tropical Convection in Low Vertical Wind Shears: Role of Updraft Entrainment, *Journal of Advances in Modeling Earth Systems*, 9(2), 1046–1068, doi:10.1002/2016MS000802, 2017.

Tsai, W.-M., et al., Co-Occurring Atmospheric Features and Their Contributions to Precipitation Extremes, *Journal of Geophysical Research: Atmospheres*, 130(5), e2024JD041,687, doi:10.1029/2024JD041687, _eprint: <https://onlinelibrary.wiley.com/doi/pdf/10.1029/2024JD041687>, 2025.

Wheeler, M., and G. N. Kiladis, Convectively Coupled Equatorial Waves: Analysis of Clouds and Temperature in the Wavenumber–Frequency Domain, *Journal of the Atmospheric Sciences*, 56(3), 374–399, doi:10.1175/1520-0469(1999)056j0374:CCEWAO;2.0.CO;2, 1999.

Wing, A. A., and T. W. Cronin, Self-aggregation of convection in long channel geometry, *Quarterly Journal of the Royal Meteorological Society*, 142(694), 1–15, doi:10.1002/qj.2628, 2016.

Wing, A. A., and K. A. Emanuel, Physical mechanisms controlling self-aggregation of convection in idealized numerical modeling simulations, *Journal of Advances in Modeling Earth Systems*, 6(1), 59–74, doi:10.1002/2013MS000269, _eprint: <https://onlinelibrary.wiley.com/doi/pdf/10.1002/2013MS000269>, 2014.

Wing, A. A., K. Emanuel, C. E. Holloway, and C. Muller, Convective Self-Aggregation in Numerical Simulations: A Review, *Surveys in Geophysics*, 38(6), 1173–1197, doi:10.1007/s10712-017-9408-4, 2017.

Wolding, B., J. Dias, G. Kiladis, F. Ahmed, S. W. Powell, E. Maloney, and M. Branson, Interactions between Moisture and Tropical Convection. Part I: The Coevolution of Moisture and Convection, *Journal of the Atmospheric Sciences*, 77(5), 1783–1799, doi:10.1175/JAS-D-19-0225.1, 2020.

Wood, R., and C. S. Bretherton, Boundary Layer Depth, Entrainment, and Decoupling in the Cloud-Capped Subtropical and Tropical Marine Boundary Layer, *Journal of Climate*, 17(18), 3576–3588, doi:10.1175/1520-0442(2004)017j3576:BLDEAD;2.0.CO;2, publisher: American Meteorological Society Section: Journal of Climate, 2004.

Wood, R., and C. S. Bretherton, On the Relationship between Stratiform Low Cloud Cover and Lower-Tropospheric Stability, *Journal of Climate*, 19(24), 6425–6432, doi:10.1175/JCLI3988.1, publisher: American Meteorological Society Section: Journal of Climate, 2006.

Xu, Q., Conditional symmetric instability and mesoscale rainbands, *Quarterly Journal of the Royal Meteorological Society*, 112(472), 315–334, doi:10.1002/qj.49711247203, _eprint: <https://onlinelibrary.wiley.com/doi/pdf/10.1002/qj.49711247203>, 1986.

Xu, W., H. Chen, H. Wei, Y. Luo, and T. Zhao, Extreme Precipitation Produced by Relatively Weak Convective Systems in the Tropics and Subtropics, *Geophysical Research Letters*, 49(7), e2022GL098,048, doi:10.1029/2022GL098048, _eprint: <https://onlinelibrary.wiley.com/doi/pdf/10.1029/2022GL098048>, 2022.

Yano, J.-I., Scale-Separation and Quasi-Equilibrium Principles in Arakawa and Schubert's Cumulus Parameterization, *Journal of the Atmospheric Sciences*, 56(21), 3821–3825, doi: 10.1175/1520-0469(1999)056j3821:SSAQEP;2.0.CO;2, publisher: American Meteorological Society Section: Journal of the Atmospheric Sciences, 1999.

Yano, J.-I., Formulation structure of the mass-flux convection parameterization, *Dynamics of Atmospheres and Oceans*, 67, 1–28, doi:10.1016/j.dynatmoce.2014.04.002, 2014.

Zhang, C., Madden-Julian Oscillation, *Reviews of Geophysics*, 43(2), doi: 10.1029/2004RG000158, 2005.

Zipser, E. J., The Line Islands Experiment, Its Place in Tropical Meteorology and the Rise of the Fourth School of Thought, *Bulletin of the American Meteorological Society*, 51(12), 1136–1147, doi:10.1175/1520-0477-51.12.1136, publisher: American Meteorological Society Section: Bulletin of the American Meteorological Society, 1970.

Zipser, E. J., and C. Liu, Extreme Convection vs. Extreme Rainfall: a Global View, *Current Climate Change Reports*, 7(4), 121–130, doi:10.1007/s40641-021-00176-0, 2021.